Characteristic Study of Noise Reduction of Brillouin Random Fiber Lasers

Zichao Zhou

Thesis submitted to the University of Ottawa
in partial Fulfillment of the requirements for the Degree of
Doctor of Philosophy
in
Physics

Department of Physics
University of Ottawa
Ottawa, Ontario, Canada

To my family

Abstract

Random fiber lasers, a new type of fiber laser that uses disordered medium to provide distributed feedback, have drawn considerable interest in the photonics community over the past ten years. Stimulated Brillouin scattering (SBS), with a typical narrow spectral width of ~100 MHz, provides an important gain mechanism for random fiber lasers. Brillouin random fiber laser (BRFL) has shown excellent advantages in generating highly coherent photons and in ultrasound sensing. However, the accompanied large intensity noise in BRFLs hinders its further performance improvement and practical applications. In order to design a low noise BRFL, it is important to explore the fundamental physics behind BRFL and study its output characteristics. This thesis focuses on the study of random lasing mechanism in BRFL, which lays the foundation for the demonstration of a low noise BRFL. The main research results and contributions are as follows:

(1) In order to understand the dynamic noise properties of BRFLs, the properties of the acoustic wave generated by BRFL, including its intrinsic spectral width, intensity dynamics, distributed spectrum and distributed intensity statistics are characterized for the first time. The characterization method is based on the SBS enhanced polarization decoupled four wave mixing process, where the pump wave, Stokes wave, probe wave and reflected probe wave are coupled through the fiber density variation induced by the acoustic wave. It is demonstrated that the intrinsic spectral width of the acoustic wave in the Brillouin gain fiber depends on the spectral convolution of pump light and Stokes light. Stochastic behaviour is introduced to the intensity dynamics of the acoustic wave when the linewidth of the pump light (or the Stokes light) is larger than several MHz. The distributed spectra of the dynamic

grating are determined by the birefringence of the Brillouin gain fiber, which have maximum change on the order of 10^{-7} to 10^{-6} when the BRFL is on operation. Different proportion of optical rogue waves are detected at high gain position and low gain position near the lasing threshold, proving the nonlinear amplification of the SBS process.

(2) In order to study the mode selection mechanism of the distributed random feedback and explore new physics phenomenon in BRFLs, the conventional Rayleigh scattering fiber in BRFL is replaced by the artificially controlled random scattering medium. First, weak FBG array with random spacing offers distributed feedback with varied length, which demonstrate the longitudinal mode filter function of the distributed random feedback. Single longitudinal mode operation of BRFL is realized by using appropriate length of the FBG array. Then, scattering from random fiber grating (RFG) with varied grating period is used to provide feedback for BRFL. The enhanced backscattering strength from RFG improves the slope efficiency of BRFL to 29.3% and reduces the lasing threshold to 10.2 mW. By calculating the correlation of the intensity fluctuation spectra from trace to trace, the correlation of two traces is found to be dependent on the specific two chosen traces, demonstrating the replica symmetry breaking phenomenon in photonics.

(3) RFG with relatively large refractive index modulation shows potentials in improving the performance of the BRFL. In order to investigate the working mechanism of the RFG, optical frequency domain reflectometry (OFDR) with spatial resolution of 8 μm is employed to characterize the property of RFG. The backscattering strength and spectral response of RFG is highly related to the degree of randomness of RFG. Theoretically, entropy is introduced to build a quantitative relationship between the degree of randomness and backscattering strength of the RFG based on the transfer matrix method. A linear relationship between the average reflectivity of the RFG in dB scale and sub-grating’s entropy is found.

Further, based on a polarization maintaining RFG, a low noise BRFL is proposed and demonstrated. Compared to Rayleigh scattering, the polarization maintaining RFG can tolerate environmental perturbation, leading to a 20 dB intensity noise suppression of the BRFL in the low frequency domain from 10 Hz to 1 kHz.

(4) The dynamic properties of the slowly varying frequency drift of a dual-wavelength BRFL in polarization maintaining fiber are characterized. Two principal lasing peaks in each polarization are enabled by the combined distributed Rayleigh scattering and the Brillouin gain provided by the polarization maintaining fiber with large birefringence. Polarization dependent and polarization independent spectral variations are studied in the dual-wavelength BRFL due to the environmental perturbation and gain competition. The probability distribution of the lasing frequency exhibits a dip near the mean frequency that is caused by the spectral hole burning. By calculating the matrix of the Pearson correlation coefficient, the internal correlations between different part of random fiber laser spectra are found, which enhances the understanding of the fundamental physics of random lasing process.

Acknowledgments

It is a precious life experience for me to join the fiber optics group in department of physics, University of Ottawa. I have benefitted a lot during this journey pursuing my Ph.D. degree. This thesis could not have been finished without the support and guidance that I have received from many people. It is my great honor to have this opportunity to thank all the people who have helped me during my Ph.D. study.

I would like to first express my sincere gratitude to my supervisor Professor Xiaoyi Bao for her continuous support of my Ph.D studies and related research. Professor Bao is one of the smartest people I know with great passion for scientific research. She is always available to have discussions with her students, and I learned a lot from these discussions with her rich experience, immense knowledge and creative ideas. Her dedication and perseverance towards scientific research is respectable, and will always be regarded as an inspiring model in my future research career. I would also like to thank Professor Liang Chen in our group. Professor Chen gives me a lot of instructive and insightful suggestions during my Ph.D studies with his profound knowledge in physics and mathematics.

I would like to thank Dr. Liang Zhang for helping me understand the frequency noise measurement method, and also for his efforts in helping me to build the experiment setup of Brillouin random fiber lasers at the initial stage of my Ph.D studies. Thanks Dr. Ping Lu and Dr. Stephen Mihailov in the National Research Council for helping me to understand the details of random fiber gratings. I would also like to thank Mr. Chengxian Zhang for helping me to build the experiment setup regarding the problems on electric circuits.

Many thanks to Dr. Chams Baker, Mr. Haiyang Wang, and Mr. Yuan Wang. They gave me a lot of assistance in building my experiment setup and discussions with them inspired in me lots of creative ideas. Thanks to my buddy Mr. Benoit Vanus for accompanying me occasionally in the journey of the Ph.D study. I would also like to express my thanks for the help from other group members: Dr. Song Gao, Dr. Huibo Fan, Dr. Yanping Xu, Dr. Lijuan Gu, Dr. Bhavaye Saxena, Dr. Wei Cai, Mr. Chen Chen, Mr. Zhuo Wang, Mr. Ole Krarup, Mr. Robert Chutu Li, and Ms. Wenwen Ma. My life in the laboratory was enriched by their company. I am also thankful to my friends, Le Qiao, Wei Cui, and Yuanming. Their company made my life in Ottawa wonderful. Thanks to Vickie Peoples for helping me to correct the grammar mistakes in the thesis.

Last, but not the least, I am deeply indebted to my parents for being understanding and supportive throughout my life in Canada! I dedicate this dissertation to them.

It is impossible to thank everyone, and I apologize to those I have inadvertently left out.

Thank you all again.

Statement of originality

This work contains no material which has been accepted for the award of any other degree or diploma in any university or other tertiary institution and, to the best of my knowledge and belief, contains no material previously published or written by another person, except where due reference has been made in the text.

I give consent to this copy of my thesis, when deposited in the University Library, being available for loan and photocopying.

SIGNED: ………………………………..

DATE: …………………………………...

Supervisor: Prof. Xiaoyi Bao

Contents

List of Figures

List of Tables

List of Acronyms

BDG	Brillouin dynamic grating
BOTDA	Brillouin optical time domain analysis
BRFL	Brillouin random fiber laser
DP-QPSK	dual polarization quadrature phase shift keying
DSH	delayed self-heterodyne
EDFA	erbium doped fiber amplifier
EOM	electro-optical modulator
ESA	electrical spectrum analyzer
FBG	fiber Bragg grating
FFT	fast Fourier transformation
FP	Fabry-Perot
FRM	Faraday rotator mirrors
FSR	free spectral range
FWM	four wave mixing
OCT	optical coherence tomography
OFDR	optical frequency domain reflectometry
OSA	optical spectrum analyzer
OTDR	optical time domain reflectometry
PBC	polarization beam combiner

PBS	polarization beam splitter
PC	polarization controller
PD	photo detector
PM	polarization maintaining
POSS	polyhedral oligomer silsesquioxanes
RFG	random fiber grating
RFL	random fiber laser
RIN	relative intensity noise
RSB	replica symmetry breaking
RS fiber	Rayleigh scattering fiber
SBS	stimulated Brillouin scattering
SMF	single mode fiber
SMSR	single mode suppression ratio
SNR	signal to noise ratio
SRS	stimulated Raman scattering
WDM	wavelength division multiplexing

Chapter 1 Introduction

The invention of laser and its applications in the field of laser spectroscopy, high precision metrology, industrial manufacturing, nonlinear optics etc., has initiated a continuous development in advanced optical engineering techniques and new generation of photonics devices since the late fifties of the 20th century. The key elements to constitute a conventional laser are pump source, gain medium and cavity, in which the cavity determines the spectral and spatial mode structures of laser radiation. In contrast, the concept of random lasers that utilize the cavityless random media to provide distributed feedback was introduced by Letokhow in 1966-1968 [1, 2]. Since then, the random laser has attracted a lot of interest both as a rich complex physical system and as a potential high performance cost-effective laser source in practical applications. The random lasing phenomenon was first observed by N. M. Lawandy [3, 4] on colloidal solutions containing rhodamine 640 perchlorate dye in methanol and TiO_2 with pump laser working at wavelength of 532 nm. Then Anderson localization of light in the random medium was studied by D. S. Wiersma [5, 6] in semiconductor powders under Ioffe-Regel criteria to realize strong scattering. An important next step was made by H. Cao who reveals the transition from amplified spontaneous emission to laser action in strongly random medium [7, 8], by measuring the photon number statistics of random lasers that change continuously from Bose-Einstein distribution at the threshold to Poisson distribution well above the threshold, as shown in Figure 1-1 [9]. The different photon statistics and lasing mechanisms of random laser with resonant feedback and non-resonant feedback were illustrated. The non-resonant feedbacks manifest as narrowing of spectrum above the generation threshold without narrowband features in the smooth spectrum [Figure 1-2 (a)], while resonant feedbacks result in narrow lasing spikes on top of the gain profile [Figure 1-2 (b)] due to the strong scattering induced closed loops of light with interference effects. Since the initial demonstrations of random laser, a large number of research articles including the spatially incoherent random laser generation and its applications [10-12], mode locking random lasers [13-15] and nanoscale random lasers [16, 17] have been reported.

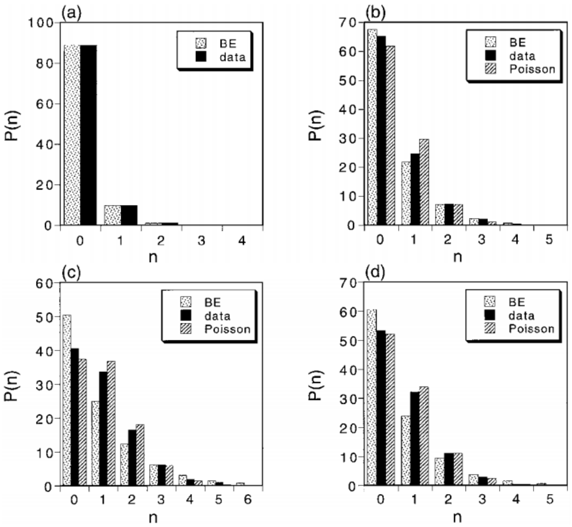

Figure 1-1 The solid columns are the measured photon count distribution of the random laser radiation. The dotted (dashed) columns are the Bose-Einstein (Poisson) distribution for the same count mean. The incident pump intensity is (a) 1.0, (b) 1.5, (c) 3.0, and (d) 5.6 times of the threshold intensity where discrete spectral peaks appear, n the is photon number of the measured mode [9].

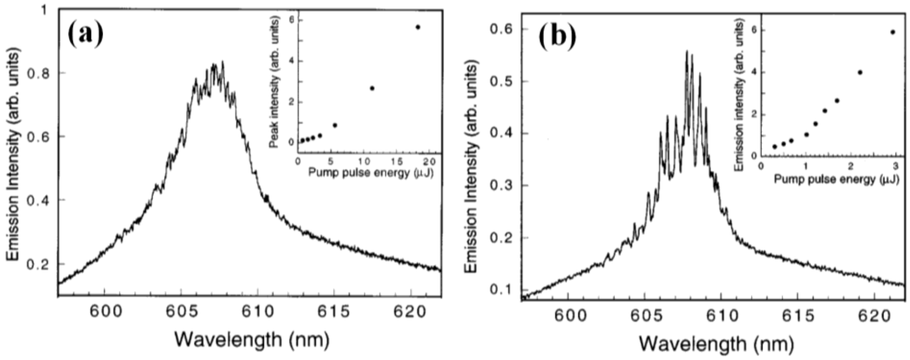

Figure 1-2 (a) Emission spectra of an RFL when the incident pump pulse energy is 5.6 μJ and particle density of ZnO is ~3×10^{11} cm^{-3}. (b) Emission spectra of an RFL when the incident pump pulse energy is 2.9 μJ and particle density of ZnO is ~1×10^{12} cm^{-3} [8].

At the same time, K. Kao [18] pointed that the fundamental limitation for glass attenuation should be below 20 dB/km. After that, the optical fiber manufacturing techniques have been greatly advanced, which lead to progressively development of fiber lasers in recent years. Tremendous achievements in the field of fiber lasers, such as the development of high power fiber lasers [19] and ultrafast fiber lasers [20], have attracted extensive attention with several review papers [21-24] introducing the fiber laser technology. Random fiber laser (RFL) is an important branch of both random lasers and fiber lasers by combining their attractive features, such as low cost and simplicity in fabrication of random lasers, good directionality and high efficiency of fiber lasers. RFLs, which can be regarded as 1-dimensional random lasers, resemble to those traditional 2-dimensional and 3-dimensional random lasers that utilize random scattering to provide laser feedback. The concept of RFL was first proposed in 2007 by De Matos etc. [25]. In their work, a suspension of 250 nm TiO_2 particles in Rhodamine 6G solutions was inserted into the hollow core of a photonic crystal fiber to generate the RFL, which showed an efficiency at least two orders higher than conventional random lasers. In 2010, Rayleigh scattering was first employed to provide distributed feedback for an RFL based on stimulated Raman scattering (SRS) [26], which was a milestone in the development of RFLs. Since then, RFLs have developed rapidly and become one of research focus in the past ten years. The significance of the research in RFLs mainly comes from two aspects. First, RFLs link to a number of interdisciplinary research fields, such as laser physics, theory of disordered systems, material science, theoretical physics and applied mathematics, nonlinear optics, transport theory and others. As a cost effective photonic platform, RFLs exhibit numerous new phenomena. Research on the physical nature of RFLs would promote the development of various disciplines and stimulate the integration of interdisciplinary research fields. Second, as a potential laser source in practical applications, RFLs can surpass the conventional fiber lasers in particular aspects of optical performance. For instance, in telecom applications, because long fiber spans are used to provide distributed Rayleigh scattering in RFLs, RFLs are natural candidates for distributed Raman amplification in quasi-lossless transmission systems. Distributed fiber sensor systems could also benefit from the unique design of random fiber lasers to realize long range remote sensing with high sensitivity. The concept of RFL leads to new promising opportunities in telecommunications, distributed sensing and secure communications. This chapter, in the following section, introduces the background of RFLs, including different types of RFLs, recent advances, and their applications. Then motivation and contribution of my research work are introduced in Section 1.2. At last, Section 1.3 gives the outline of the thesis.

1.1 Background

This section reviews the development of RFLs from the following three aspects. First, different categories of random RFLs are summarized depending on gain mechanisms and types of random medium. Then, recent researches on the high power generation, spectral properties management and temporal statistical properties of RFLs are introduced. At last, the applications and challenges of RFLs are discussed.

1.1.1 Types of RFLs

RFLs make use of the multiple scattering of photons in a disordered medium to provide optical feedback. Lasing occurs when the total gain in the random cavity overcomes the total loss. Therefore, RFLs can be classified either by the category of disordered medium or by types of gain mechanisms. There are three main types of random disordered mediums utilized in RFLs: (1) random nanoparticles scattering in colloidal suspension, (2) random refractive index modulation that are introduced in the random fiber grating (RFG) and (3) Rayleigh scattering from the intrinsic refractive index variation of fiber. Depending on the gain mechanisms, random fiber lasers can be classified as Raman gain based RFL, Brillouin gain based RFL, Er-doped (or other types of rare earth ion doped) gain based RFL and hybrid gain based RFL.

A. Nanoparticles scattering feedback

Random nanoparticles scattering in colloidal suspension inserted in the hollow core fiber were the first disordered medium employed in RFLs. In such a configuration, the strength of disorder can be controlled by varying concentration of scatters while the fiber provides necessary confinement and directionality. De Matos demonstrated such a configuration in the incoherent feedback regime [25]. A coherent RFL was realized in a similar configuration, in which a dispersive solution of polyhedral oligomer silsesquioxanes (POSS) nanoparticles and laser dye pyrromethene 597 in CS_2 were injected into a hollow core fiber [27], as shown in Figure 1-3. Then, by employing the *in situ* formed weak POSS scatters during polymerization, the optimized configuration of the nanoparticles based RFL was demonstrated [28], which showed stabilized output spectrum and lower lasing threshold. An RFL using the disordered layer at the internal surface in the cylindrical waveguide was reported in [29]. The disordered layer provides randomly scattered light, and the fiber was filled with laser dye solution in the core region, providing both light confinement and laser gain. Since the performance of nanoparticle enabled random fiber laser is sensitive to the scattering strength, it can be used to detect the concentration of small particles in the dye solution.

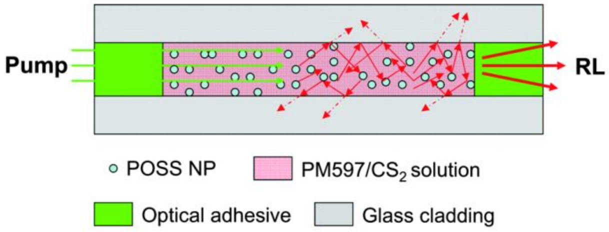

Figure 1-3 Schematic of the RFL system based on nanoparticles scattering in liquid core optical fiber (POSS NP: polyhedral oligomer silsesquioxanes nanoparticles; RL: random laser; PM597: pyrromethene 597) [27].

B. Rayleigh scattering feedback

Rayleigh scattering that is initiated from intrinsic disordered refractive index variation of fiber offers a naturally random feedback mechanism, which is the one most widely used in building RFLs. Ultra-long fiber with total length of 83 km was used in the first demonstration of RFL based on Rayleigh scattering [26], as shown in Figure 1-4. Though the loss coefficient of the telecommunication fiber determined by Rayleigh scattering is ultra-low (0.2 dB/km) with a backscattering coefficient as small as $\varepsilon = 4.5\times10^{-5} km^{-1}$, distributed backscattering was accumulated in the long fiber resulting in strong feedback to form RFL. At the same time, SRS was initiated in the long fiber with high pump power to provide light amplification as the gain mechanism of RFLs. The work demonstrated that stationary lasing with narrow spectrum can be enabled by distributed Rayleigh scattering, disproving the previous opinion that fiber lasers with distributed Rayleigh scattering must exhibit irregular stochastics behavior [30, 31]. Because the strength of Rayleigh scattering is inversely proportional to λ^4, shorter wavelengths of light are scattered more strongly in the fiber. At the same time, the nonlinear effect in single mode fiber (SMF) is enhanced at shorter wavelengths due to the relatively small effective mode field area, which can further increase the efficiency of an RFL with short length of the SMF. D.V. Churkin demonstrated random distributed feedback Raman fiber laser operating at a 1.2 μm wavelength range [32] with a slope efficiency of more than 30%. Cascaded architecture [33] was further employed in the 1.2 μm spectral band Raman RFL with conversion efficiency reaching up to 60%.

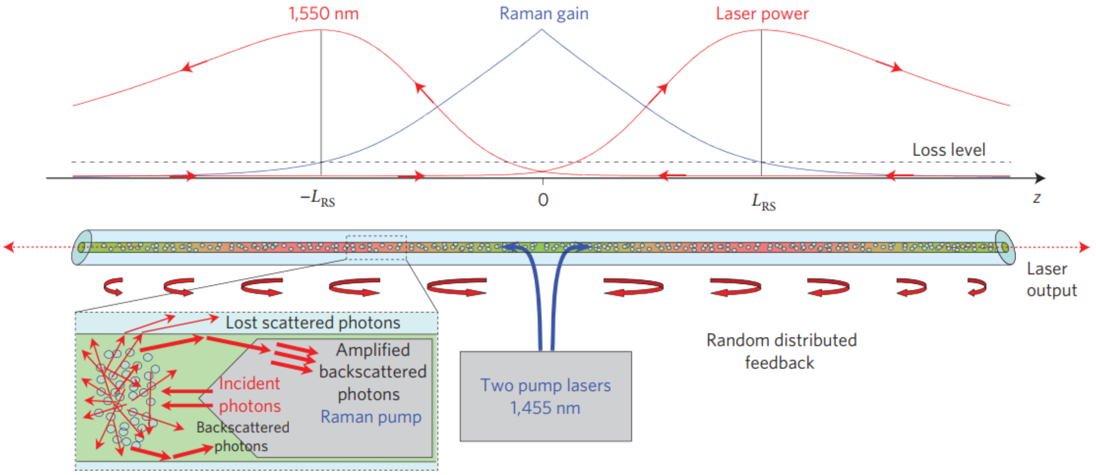

Figure 1-4 Principle of random distributed feedback fiber laser based on Rayleigh scattering. Two pump waves coupled at z=0 provide distributed Raman gain along the fiber. Photons propagating in the long fiber are coherently scattered by random refractive index variation. The backscattered guided photons can be amplified if total gain (blue) is larger than the loss level (dashed line). As a result, forward (red line, right arrows) and backward (red line, left arrows) propagating waves are generated [26].

C. RFG feedback

Randomness of fiber can also be artificially introduced by inscribing RFGs or introducing random refractive index variations in a controlled fashion [34], providing additional flexibility in managing properties of RFLs. Because of the light localization in the random medium, high Q resonance can be realized with randomly distributed phase shift [35, 36]. The localization theory in the 1-dimensional RFG was demonstrated in [35] by measuring the exponential intensity decay of the light after transmitting from the random fiber medium. The first random Erbium doped fiber laser with lowest threshold (3 mW) to date was demonstrated based on a RFG [37]. A narrow linewidth tunable random feedback fiber laser with low intensity noise was demonstrated based on a CO_2 laser refractive index modification on a standard telecommunication SMF [38]. The random refractive index modulation of the fiber was also achieved by a femtosecond laser as shown by the microscopic view of the index modulation in Figure 1-5 [39]. In their work, the spacing between neighboring index modulation planes was arbitrarily varied from 10 μm to 30 μm with large index change on the order of 10^{-3}, which suppressed the frequency noise of RFL with 2.1 kHz laser linewidth. By tailoring a series of randomly separated fiber Bragg gratings (FBG) in an active Er-doped optical fiber, the lasing mode of the RFL can be controlled [40]. Other demonstrations of RFLs enabled by RFG can also be seen in [41-44].

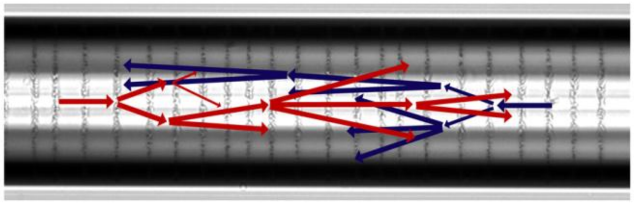

Figure 1-5 A microscopic image of the femtosecond laser modulation of the RFG [39].

D. Gain based on SRS

The idea of RFL based on SRS can be traced back to the research in 2007 [45], which dealt with the interesting question of the longitudinal mode structure formed in a Raman fiber laser with an ultra-long cavity. The work demonstrated that the maximum length for a Raman fiber laser to maintain its longitudinal mode structure was ~270 km. The ~0.38 kHz mode spacing governed by the rule $\Delta\upsilon = c/2nL$ was observed in the 270 km long Raman fiber laser. When the cavity length was longer than 300 km, the strength of the accumulated Rayleigh scattering was greater than that of the reflection from the FBG at the fiber end, thus the conventional longitudinal mode was suppressed though the laser could still be generated. This idea evoked the first demonstration of Raman RFL based on Rayleigh scattering [26] as it proved that the fixed cavity in conventional fiber lasers could be replaced by distributed Rayleigh scattering. Then, an optimized version of the Raman RFL was proposed [46] with more work to demonstrate multi-wavelength generation [47-49], super-continuum generation [50] and tunable RFL [51, 52]. SRS is currently the most widely demonstrated gain mechanism in building RFLs.

E. Gain based on SBS

Stimulated Brillouin scattering (SBS), whose typical threshold is one order of magnitude lower than that of SRS [53], provides an ideal gain mechanism for RFL. With an intrinsic narrow Brillouin gain bandwidth on the order of ~100 MHz, Brillouin random fiber laser (BRFL) naturally takes the advantage for generations of highly coherent photons. Narrow spectrum of Stokes field and Gaussian statistics of Stokes power were observed in cooperative stimulated Brillouin and Rayleigh backscattering processes in [54]. The BRFL was first demonstrated by Pang *et al* in [55], in which the resonator of the BRFL was composed of three different fiber spans, as shown in Figure 1-6. The Brillouin Stokes wave was amplified by the middle fiber section with enhanced random feedback produced by the Rayleigh scattering from the other two fiber sections. When the Brillouin gain of the middle fiber overcomes the loss, single frequency lasing was observed with a linewidth of ~3 kHz. A dramatic decrease of the lasing linewidth (~10 Hz) was achieved via high quality coherent random oscillation based on SBS, in which the random multi-scattering centers were separated from the Brillouin gain medium [56]. The configuration was further optimized to realize frequency stabilized BRFL using high finesse narrowband Fabry-Perot (FP) interferometer to select lasing frequency within the Brillouin gain bandwidth [57]. More recent work of RFLs based on Brillouin gain includes demonstration of linearly polarized BRFL [58, 59] and multi-wavelength generation based on BRFL [60, 61].

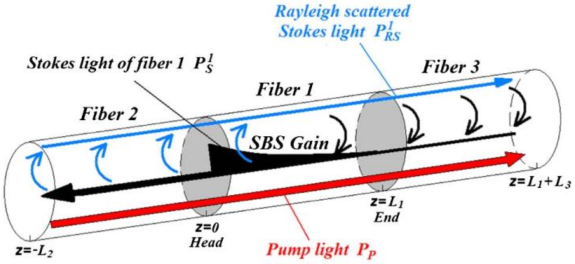

Figure 1-6 A BRFL composed of three types of fibers with different Brillouin frequencies. The middle fiber (Fiber 1) was used to provide Brillouin gain, and the two sides (Fiber 2 and 3) were used to provide random feedback [55].

F. Gain based on rare earth ions

RFLs based on SBS and SRS act on the principle of distributed amplification, which needs long length of fiber to provide sufficient gain. In contrast, the high gain and wide bandwidth provided by Erbium ions make them an attractive choice to demonstrate RFLs based on Er-doped fiber as gain mechanism with short length. In [62], stimulated Rayleigh scattering was initiated in a non-uniform fiber to realize a tunable narrow linewidth Er-doped RFL, which achieved 3 dB linewidth of less than 2 kHz with 70 dB extinction ratio. The configuration of the Er-doped RFL was optimized in [63], which used the distributed Rayleigh scattering to eliminate the longitudinal cavity mode and to compress linewidth of the laser. Thermal frequency noise of Er-doped RFL was suppressed in an half open cavity configuration [64], as shown in Figure 1-7. The feedback from Rayleigh scattering suppressed the noise at high frequencies by introducing a Lorentzian envelope over the thermal frequency noise, realizing the minimum value for an optimized length of the Rayleigh scattering fiber. Further demonstrations of Er-doped RFLs can be seen in [65-67]. More recently, wavelength locking of Er-doped RFL was demonstrated in [68]. Similarly, other types of rare earth ions were also used as gain mechanism for RFLs, such as the Yb-doped RFL [52] operating around

1 μm, Bi-doped RFL [69] operating around 1.2 μm and Tm-doped RFL [70] operating around 2 μm.

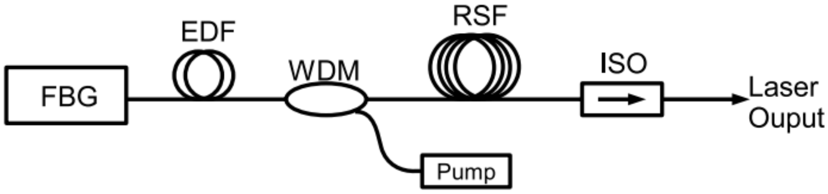

Figure 1-7 Schematic of the RFL based on Er-doped gain. FBG: fiber Bragg grating; EDF: Er-doped fiber; WDM: wavelength division multiplexing; RSF: Rayleigh scattering fiber; ISO: isolator [64].

G. Hybrid gain

Furthermore, the RFL can be realized by combining different types of gain mechanisms. For example, by integrating Rayleigh scattering based Raman RFL with a section of Er-doped fiber, the working range of the remotely pumped Er-doped fiber was extended to L band [71]. A high dense multi-wavelength generation of Brillouin-Raman RFL was demonstrated in [72, 73] with over 500 Stokes lines and an optical signal to noise ratio (SNR) higher than 12.5 dB. Cascaded Stokes light was generated in a hybrid Brillouin gain and Er-doped gain RFL by enhanced amplification of the Brillouin Stokes light in active Er-doped fiber [74]. Single peak random lasing with spectral contrast ratio up to 35 dB was demonstrated in an RFL based on combination of Er-doped gain and Raman gain [75]. An RFL based on hybrid Raman-Erbium gain showed improved performance in producing single lasing peak with maximum optical SNR of 62.37 dB [76].

1.1.2 Development of RFLs

In the past ten years, RFLs have experienced a rapid development with numerous efforts to study their unique properties and to improve their performances. Considering the output properties of RFLs, in the following we will introduce the current development of RFLs from three aspects: (1) high power and high efficiency generation of RFLs; (2) temporal and statistical properties of RFLs and (3) spectral properties and management of RFLs.

A. High power and high efficiency generation

The simple configuration of RFL has attracted a lot attention in the research field for high power laser generation with ultimate efficiency [77]. A comprehensive study of power output characteristics of a random distributed feedback Raman fiber laser was presented in [78], which analytically predicted an exponential growth of laser efficiency with decreasing fiber length, as shown in Figure 1-8. In [79], the longitudinal power distribution was experimentally and theoretically investigated in the RFL. An ultrafast convergent power balance model was proposed in [80] to predict the slope efficiency and power distribution of RFL with improved calculation efficiency. Experimentally, a high efficiency RFL using 850 m span of a phosphosilicate fiber was demonstrated with an output power of 7.3 W [81]. Later on, a total output power of 73.7 W was demonstrated in a Raman fiber laser based on weak Rayleigh scattering feedback [82]. The cavity length of the Raman RFL was only 300 m, enabling a laser efficiency of 74.7%. It was demonstrated in [83] that the quantum efficiency of converting the pump into the random laser output radiation was almost independent of the Raman Stokes power. In 2016, a 200 W output power based on Raman RFL was realized by a simple 120 m long cavity with 89% of observed optical-to-optical conversion efficiency [84], which confirmed the theoretical prediction in [85]. Furthermore, by using a Yb doped fiber oscillator as the pump source combined with a core diameter of 20 μm fiber as the gain medium, the maximum output power of the Raman RFL reached up to 418 W [86]. A tapered fiber with longitudinal varying diameter was used to suppress the four wave mixing (FWM) effect in a high power Raman RFL, which achieved a maximum output power of 491 W [87]. High power linearly polarized RFL emission was demonstrated in [88], where a Lyot filter was employed to manipulate the polarization dependent Raman gain. More recently, kilowatt level random fiber lasers were demonstrated based on a half open cavity [89] and tandem pumping [90] respectively.

In the above high power RFLs, the pump source was high brightness laser radiation which was further pumped by high power laser diodes. In order to simplify the configuration, a random lasing based on Rayleigh scattering in a passive fiber was directly pumped by the high power laser diode in [91]. In this configuration, laser diode beam was converted into high quality laser output owing to the Rayleigh scattering based random distributed feedback. Though the generated power only approached 1 W level at a wavelength below 1 μm, it offers new opportunities in the development of fiber laser sources at short wavelengths in the near infrared and visible ranges [92]. Later, cascaded Raman generation of the second Stokes order was demonstrated in the laser diode pumped RFL with near diffraction limited beam quality and an output power of 17 W [93].

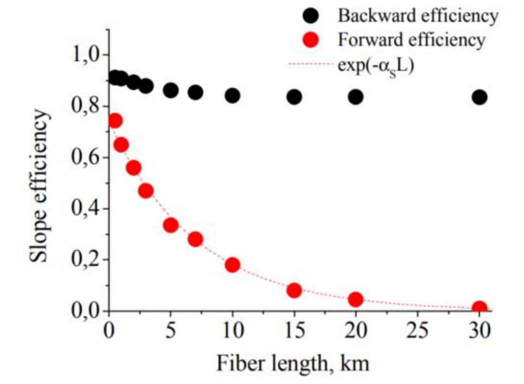

Figure 1-8 Generation efficiency of the forward and backward waves over fiber length in a Raman RFL [78].

B. Temporal and statistical properties of RFLs

In order to understand the physics of the operational mechanisms of RFLs, it is important to investigate the temporal dynamics and statistical properties of random laser radiation. Such efforts have been made by researchers theoretically and experimentally. Selfoscillations of a random distributed feedback Raman fiber laser with period close to transit time of the cavity was observed in [94], where the authors used a temporal-spatial-coupled numerical model to describe the observed temporal oscillations. A numerical nonlinear Schrödinger equation model was proposed in [95] to describe the temporal and statistical properties of random distributed feedback fiber lasers. The influence of the random backscattering via dispersion and nonlinearity was taken into account in the model, which revealed evidence of non-Gaussian intensity statistics of RFLs due to the stochastic fluctuations on the order of picosecond. The deviation from the exponential curve at low dispersion in Figure 1-9 (c) manifests the non-Gaussian statistics of the RFL radiation. However, due to the limited bandwidth of a conventional oscilloscope and photodetector, it is hard to characterize the fast intensity fluctuations in the experiment. Later, the fast intensity dynamics of random distributed feedback fiber lasers was experimentally measured in [96] by using a high bandwidth oscilloscope and photodetector, supporting the theory proposed in [95].

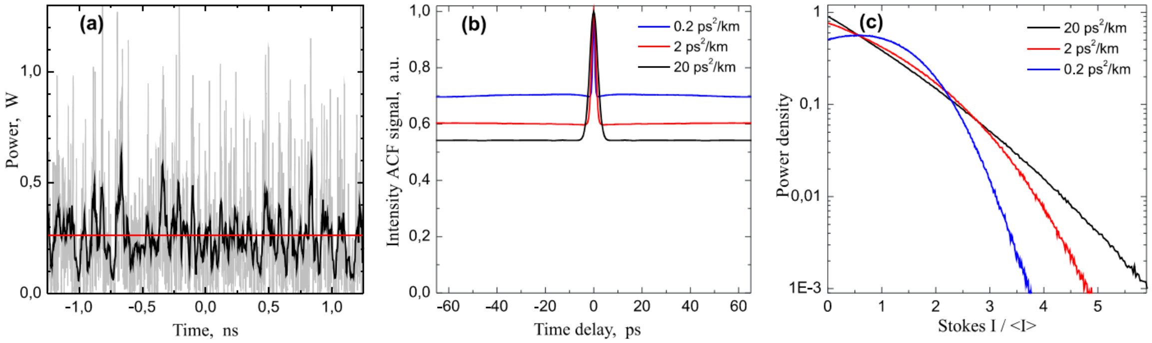

Figure 1-9 (a) Typical intensity dynamics (grey shows original simulated data, black is smoothed with a bandwidth of 40 GHz, red is the average lasing power level), (b) Intensity auto-correlation function and (c) intensity probability density functions for different fiber dispersions [95].

The unusual intensity statistics of RFLs provide a photonic platform to study interdisciplinary phenomena in their nature. For example, the extreme event in fiber lasers was linked to the optical rogue wave [97], which originally describes the extremely large intensity water wave in the open ocean. An optical rogue wave was detected in the transient intensity of an incoherently pumped RFL in [98], which was attributed to a crucial SBS process with an intrinsic stochastic nature. Many RFL systems exhibited deviation from the Gaussian intensity statistical distribution [99-102]. Transitions from the Gaussian statistics to Lévy statistics and back to Gaussian statistics were experimentally demonstrated in a one dimensional Er-based RFL [103], as shown in Figure 1-10. Compared to Gaussian distribution, the Lévy distribution exhibits long tails in the probability density function which means more extreme events in the Lévy distribution. Mathematically, if the stochastic values assumed by I are uncorrelated and the second moment of the probability density function $P(I)$ is finite, the central limit theorem assures that the associated fluctuations are driven by Gaussian dynamics. On the other hand, if the second moment of $P(I)$ diverges, the generalized central limit theorem states that the fluctuations are governed by Lévy statistics. A similar phenomenon was also observed in a Raman RFL [104]. Turbulent behavior was demonstrated in photonics based on an RFL [105], in which three distinct behaviors of intensity distribution were exhibited: a Gaussian regime below threshold, a mixture of two distributions with exponentially decaying tails near the threshold and a mixture of distributions with stretched-exponential tails above threshold. As a random photonic platform, RFLs also demonstrated the transition from a photonic paramagnetic phase to a photonic spin-glass phase, signaled by the phenomenon of replica symmetry breaking (RSB) in [106, 107]. The replica symmetry means that in a disordered system, the replicas are ergodic and independent from each other with identical states so that they have no correlations (or coupling strength) to each other, such as the local magnetizations in paramagnetic. The replica symmetry is broken when two replicas of the same disordered system stay in different states so that the correlations between the two of them are determined by the two specific chosen replicas, which is the case of the local magnetizations in spin glass. In [106], the intensity fluctuation spectra of the random lasing radiation is the analogy replica that represent the state of the RFL. By calculating the distribution of correlations between intensity fluctuation spectra of the RFL from pulse to pulse, the authors in [106] found that the RFL in identical conditions can reach different states, which is called as the photonic spin glass state since it has the same statistical property as the local magnetizations in spin glass.

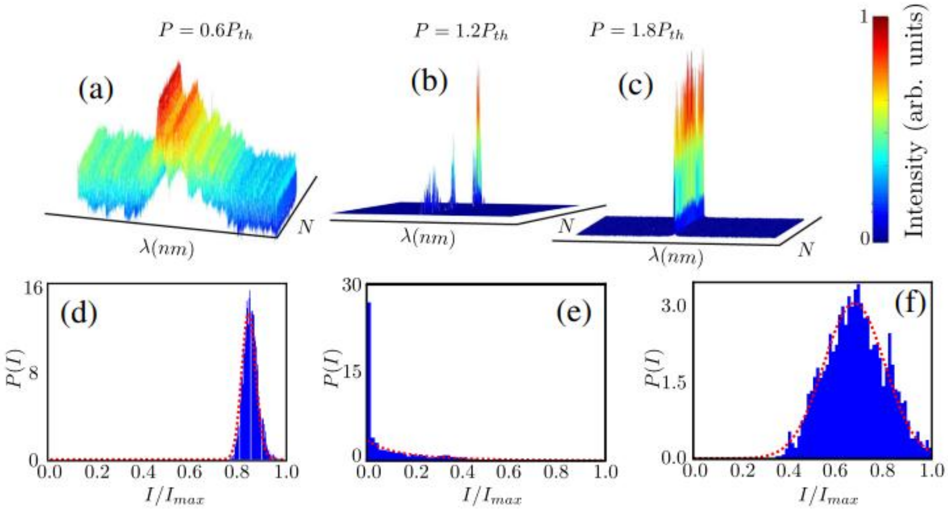

Figure 1-10 (a)-(c) Intensity spectra of a Er-based RFL system at input power (a) below (b) around (c) above the threshold; (d)-(f) Probability density function of maximum intensities obtained from the data shown in (a)-(c) [103].

One of the drawbacks of RFLs is the high relative intensity noise (RIN) arising from the intensity noise transfer from pump sources, environmental perturbations and a large number of random lasing modes. The RIN transfer from a noisy pump to the generated Stokes component in random distributed feedback Raman fiber lasers was numerically investigated in [108] and experimentally observed in [109]. Several techniques have been employed to suppress the RIN of RFLs. For example, linear polarization operation of BRFL can reduce the RIN compared to that of a custom SMF based BRFL [59]. The intensity noise of a BRFL assisted by a random grating-based FP resonator was suppressed due to the reduced resonating modes and mode competition resulting from the random grating formed filters [110]. In order to alleviate the RIN transfer from the pump source, a single-end pump scheme instead of the bi-directional scheme was used to build the BRFL, which significantly reduced the lasing instabilities [111].

The output intensity modulation of RFLs has also attracted a lot of attention in the research field. The RFL was internally modulated by incorporating an electro-optical modulator (EOM) into the loop cavity in [15]. Unlike the conventional modulated lasers where the cavity length determines the repetition rate of the generated pulses, no distortion of the modulating frequency or self-mode-locking effects were observed in the RFL. External modulation of RFL based on saturable absorption of the monolayer was demonstrated in [112], in which temporal compressed pulses with minimum 900 ps pulse width were observed. Pulse generation of RFL was also realized by the Q switching mechanism [70, 113-115]. In [70], the Q switching process of RFL was based on rapid increasing of the Q factor resulting from SBS, which further lead to unstable pulse intensity and repetition rate. Stable pulsed RFL was realized in [115], in which spatial temporal gain modulation was implemented by modulating the power distribution of the pump source. In [116], selectable repetition rates of pulses were demonstrated by passive mode locking of a coherent RFL.

C. Spectral properties of RFLs

Research on output spectral properties of RFLs provides another method by which to explore the rich underlying physics behind the random optical system. At low pump power levels below the threshold, the RFL system indicated a spectral narrowing effect as pump power increased [46], while at high pump power above the threshold, spectral broadening effect was observed due to the nonlinear process. In [117], spectral width of a random distributed feedback fiber laser was optimized by adjusting the length of fiber which provides gain and random scattering. Multi-peak structure of the generation spectrum was observed in a distributed feedback fiber laser based on SRS [118]. Wave kinetic theory was developed to describe the spectral properties of RFL [119], which are defined by a large ensemble of nonlinearly interacting light waves. The model predicted the spectral evolution behavior of random fiber lasers well, e.g. the dramatic spectral linewidth decreases near the lasing threshold and the spectral broadening trend above the threshold. Spectral correlations in a random distributed feedback fiber laser were analyzed by the Pearson correlation coefficient in [120], which found secondary correlation peak at a wavelength spacing of 0.08 nm and an anti-correlation peak at a wavelength spacing of 20 pm, as shown in Figure 1-11. The secondary correlation peak indicated the existence of SBS process while the anti-correlation peak revealed the homogeneous gain dynamics. Extreme frequency shift of a phosphosilicate RFL was investigated in [121]. In [122], the internal interactions of different spectral components within a multi-wavelength random distributed feedback fiber laser was characterized by the Pearson correlation coefficient, which revealed the spatial location over the gain fiber where the interactions took place. Temporal variation of the spectrum in a continuously pumped RFL was studied in [123], where a phenomenological mathematical model was developed to describe the experimentally observed peculiarities of the spectrum temporal evolution.

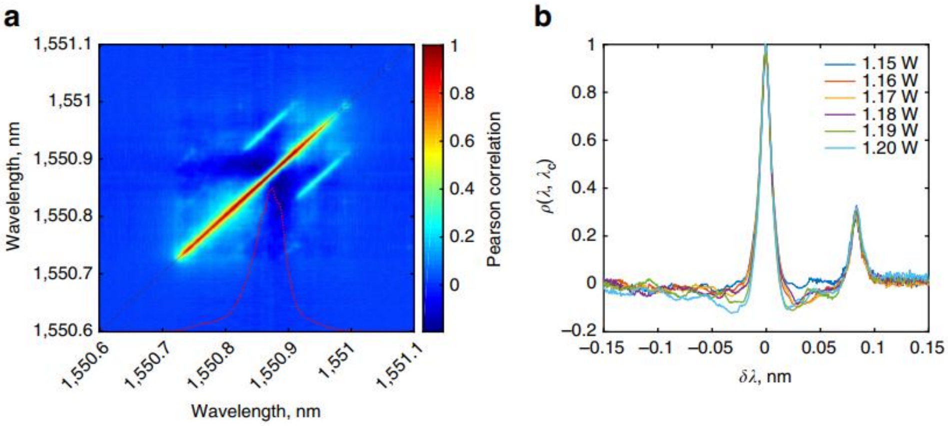

Figure 1-11 Spectral correlations in an RFL. (a) The Pearson correlation coefficient matrix, and (b) its cross-section for different pump powers [120].

Besides the fundamental physical research on the spectral properties of RFLs, their spectral management has also attracted a great deal of research interest. Narrow bandwidth emission of spectral width down to ~0.05 nm linewidth was achieved in a random distributed fiber laser enabled by fiber FP interferometer filters [124]. A ~10 Hz narrow linewidth lasing spike was observed in a coherent BRFL [56], which was then followed by a bidirectional pump scheme to reduce its frequency noise [125]. In [126], a tapered fiber was used to enhance Rayleigh backscattering and to increase power density of the BRFL. The wavelength of RFL could be tuned by incorporating tunable filters into the cavity of RFL, which was first demonstrated in [51] with broad range flat wavelength response and good spatial and spectral performance. Ultra-wide wavelength tuning range of up to 300 nm was achieved in a cascaded Raman RFL by adjusting the pump wavelength and power altogether [127]. The tunable RFL was also demonstrated at 1.7 μm wavelength region [128], with high spectral purity above 92% over a tuning range from 1705 nm to 1725 nm. In [129], the spectral purity of the RFL was optimized by selecting appropriate bandwidth of the pump source. Because of the flat wavelength reflectivity of the random feedback, RFLs naturally have the advantage in multi-wavelength generation [47, 130] compared to conventional fiber lasers. Various schemes of multi-wavelength Raman RFLs were employed, such as by using an all fiber Lyot filter [131, 132], Hi-Bi photonic crystal fiber [49, 133], external micro-air cavity [134] and broadband pumping source [135]. In [136], multi-wavelength tuning was demonstrated in a Raman fiber laser based on random Rayleigh backscattering. Multi-wavelength generation of RFLs based on Brillouin gain and hybrid gain was investigated in [60, 61, 72, 73]. Switchable multi-wavelength operation of RFLs was demonstrated in [137, 138]. Benefiting from the wide flat spectral response of the random distributed feedback, super-continuum generation in RFLs was also demonstrated [139, 140], providing a new method to generate low intensity noise super-continuum laser sources [141].

1.1.3 Applications of RFLs

A. Point sensing

It was found that the RFL is a temperature insensitive distributed lasing system [142]. By introducing some additional elements, such as an FBG, the RFL could operate as a sensing system with the output spectrum following the spectral response of the additional elements. Two 100 km FBG point sensing schemes based on RFLs were experimentally demonstrated in [142] based on the first-order and the second-order Raman random lasing respectively, suggesting that the length limit of the fiber sensing system can be significantly beyond 100 km. Two hundred kilometers long point-sensing systems were further realized based on similar methods in [143] and in [144]. In [145], the optical SNR of the long distance point sensing system was improved by introducing an active fiber into the RFL system. Temperature insensitive strain measurement was demonstrated in [146] based on the RFL with two FBGs, both of which had the same sensitivity to temperature but only one of the FBGs was sensitive to strain. A high resolution sensor system was demonstrated using a random distributed feedback fiber laser, where a phase shifted FBG was incorporated as the sensor [147, 148]. Besides regular FBG, other types of sensing elements were also employed in RFLs. In [149], a suspended-core FP interferometer acted as both the reflective mirror of the RFL and the sensing element for temperature measurement. RFG, as an important random feedback mechanism for RFL, was also used as the sensing head to realize a high signal to noise ratio of ultrasound detection in [150, 151]. In [152], a high resolution static strain sensor was demonstrated by the RFG enabled RFL.

B. Distributed sensing and light transmission

The realization of random lasing in long-distance fiber span makes the RFL naturally suitable for distributed gain amplification. It was demonstrated in [153] that the forward pumping of the Raman RFL could reduce the effective noise figure of the amplification process compared to conventional bidirectional Raman amplification, providing a low noise and stable long distance signal transmission method. The distributed Raman amplification in RFL was further applied to a 10×116 Gb/s dual polarization quadrature phase shift keying (DP-QPSK) wavelength division multiplexing (WDM) transmission [154], extending the maximum transmission length up to 7915 km. The distributed fiber sensing can also benefit from the RFL based distributed amplification. In [155], a configuration of hybrid distributed Raman amplification was demonstrated based on a second order pump and first order pump to achieve ultra-long distance distributed sensing in Brillouin optical time-domain analysis (BOTDA). In [156], a 175 km sensing length of a repeaterless BOTDA system was demonstrated based on the hybrid of forward second order and backward third order pump of Raman RFL amplification.

C. Other applications

The less phase-correlated random modes in RFLs lead to chaotic laser output intensity fluctuations, which can be used as the source for truly random bit generation [157-159]. Due to the uncorrelated temporal intensity fluctuations of the RFL, it achieved superior performance for ghost imaging compared to cavity based fiber lasers [160]. The narrow linewidth of the BRFL provided a novel method to generate the tunable ultra-narrow linewidth microwave signals by beating two Stokes beams from two different pump sources [161]. At the same time, the narrow linewidth enabled by the BRFL was used as a ruler to characterize the spectral width of other laser sources [162]. Owing to the low spatial coherence of the multi-transverse mode of the RFL [163-165], spectral free imaging was demonstrated by using the RFL with multi-transverse mode as the illumination light source [166].

1.2 Thesis motivation and contribution

1.2.1 Motivation

Since RFLs have wide potential applications, it has great significance to explore the underlying physics behind RFLs in order to further improve their performance. Although various RFLs have been demonstrated over the past ten years, most of the current works are utilizing SRS as the gain mechanism of RFLs. Compared to SRS, SBS with narrow gain bandwidth provide a method to generate highly coherent random lasing radiation. However, current RFLs based on Brillouin gain still suffer from large intensity noise due to mode hopping, which hinders its practical applications. The motivation of this thesis is to reduce the intensity noise of BRFL to get a low noise highly coherent random lasing source. To realize the purpose, it is important to first investigate the internal working state of BRFL and study its output characteristics. Therefore, in this thesis, the property of the acoustic wave generated by BRFL is first presented in Chapter 3. Then, the output characteristics of the BRFL enabled by artificial controlled random scattering is investigated in Chapter 4. Based on the results of Chapter 3 and Chapter 4, a low noise BRFL that is insensitive to the environmental perturbation is proposed in Chapter 5. Finally, the slowly varying frequency drift of a dual-wavelength BRFL is characterized in Chapter 6, as this property is a crucial factor for influencing laser's performance in the applications of distributed sensing, especially for the measurement ability of low frequency signal.

1.2.2 Thesis contribution

This thesis proposes a low noise BRFL based on a PM RFG, and studies the characteristics of BRFL, such as the property of the acoustic wave, statistics of the output intensity, longitudinal mode property, linewidth, intensity noise and frequency noise of the laser. Major contributions of the thesis include:

(1) The intrinsic spectral width and intensity dynamics of the acoustic wave generated by the BRFL are characterized experimentally by using a probe light for the first time. These are important to the understanding of the dynamic noise properties of RFLs based on SBS. The spectra of the acoustic wave in the gain medium are demonstrated to be determined by the spectral convolution of pump light and its Stokes light, which is further an influential factor on the narrow linewidth of the RFL resulting from the distributed feedback of coherent Rayleigh scattering. The power of the probe light is weak to ensure the minimum disturbance to the random fiber laser. In the time domain, the intensity of the reflected probe light exhibits a similar output property to that of the BRFL with Gaussian probability distribution when both narrow linewidth lasers (on the order of several kHz) are used as a pump light and a probe light. In contrast, stochastic noise features with an exponential probability

distribution are introduced to the intensity dynamics of the reflected probe light when the linewidth of the pump light or the probe light is several MHz. The phase noise and intensity noise of the reflected probe light prove that acoustic wave generation and detection are based on a FWM process, which enhances our understanding of the wave coupling in RFLs.

(2) By using the optical time domain reflectometry (OTDR) method, the time resolved distributed acoustic wave generated by a BRFL is characterized. The dynamic property of the acoustic wave reflects gain dynamics of the BRFL. Static measurements present exponentially depleted Brillouin gain along the gain medium in the BRFL, indicating the localized random SBS frequency change in maximum local gain region, which varies with time to contribute random laser noise as revealed in the dynamic measurement. The SBS induced birefringence change in the Brillouin gain fiber is approximately 10^{-7} to 10^{-6}. The phase noise of the BRFL is observed directly inside the random laser gain medium for the first time via time and spatially varied acoustic wave intensity. By counting the temporal intensity statistical distribution, optical rogue waves are detected near the lasing threshold of the BRFL. Different temporal intensity statistical distributions at high and low gain positions are found which are caused by the SBS nonlinear transfer function and localized gain. The distributed characterization methods in this paper provide a new platform to study the interaction of random lasers and random medium, giving us a new perspective to understand the fundamental physics of the random lasing process and its noise properties.

(3) The mode characteristics of the BRFL are manipulated by different distributed random feedbacks, which act as the longitudinal mode filter. A theoretical model is developed to analyze the mode characteristics of BRFL with varied lengths of weak FBG arrays. In the experiment, a single FBG, weak FBG arrays (reflection of -40 dB) at various lengths, and a Rayleigh scattering fiber are used to provide the random feedback. Both theoretical analysis

and experimental results show that single longitudinal mode operation can be realized with the distributed random feedback interferometer, leading to a stable temporal intensity output of the BRFL in the time domain.

(4) We report a high efficiency BRFL enabled by a RFG with demonstration of RSB. The RFG is characterized by the optical coherence tomography (OCT) method, which measures the spatially resolved reflectivity of RFG by a tunable delay line. Multiple narrow linewidth peaks appear in reflection spectrum of RFG, created by frozen scattering centers to select random modes in RFLs based on Brillouin gain. With the scattering from RFG as disordered feedback, a BRFL with slope efficiency of 29.3% and lasing threshold of 10.2 mW is demonstrated. Intensity dynamics show that RFG can reduce the noise of BRFL with a symmetric phase portrait, indicating the increased mean free path length and coherence time of the Stokes photons. The probability distribution of the Parisi overlap parameter of intensity fluctuation spectra from trace-to-trace reveal a photonic spin-glass phase with RSB in the RFG enabled BRFL, providing a photonic platform to study the photon glassy behavior of RFLs.

(5) RFGs with different degrees of randomness are characterized experimentally by optical frequency domain reflectometry (OFDR). Experimental results show that the high degree of randomness leads to a low backscattering strength of the grating and strong strength fluctuations in the spatial domain. The local spectral response of the grating exhibits multiple peaks and a large peak wavelength variation range when its degree of randomness is high. In order to find a quantitative relationship between the degree of randomness and spectrum property of RFG, entropy is introduced to describe the degree of randomness induced by period variation of the sub-grating. Simulation results show that the average reflectivity of the RFG in dB scale decreased linearly with increased sub-grating entropy, when the

measured wavelength range is smaller than that of the peak wavelength variation of the sub-grating. The peak reflectivity of the RFG is determined by $\kappa^2 L\Delta P$ (where κ is the coupling coefficient, L is the grating length, ΔP is period variation range of the sub-grating) rather than κL when ΔP is larger than 8 nm in the spatial domain. The experimental results agree well with the simulation results, which helps to optimize the RFG manufacturing processes for future applications in RFLs and sensors.

(6) Based on a PM RFG, we propose and demonstrate a thermal and acoustic noise insensitive BRFL. A theoretical model is developed to analyze environmental perturbation on the randomly induced refractive index modulation via a PM random grating. Both the theory and experiments show that the scattered optical intensity of the PM RFG exhibits a weak dependence on the temperature fluctuation and the acoustic noise perturbation compared to that of the Rayleigh scattering from hundreds of meters of PM fibers, leading to the Brillouin random lasing radiation with a 20 dB RIN suppression in the frequency range from 10 Hz to 1 kHz.

(7) The dynamic spectral properties of a dual-wavelength BRFL with orthogonal polarization are characterized experimentally for the first time. The dual-wavelength BRFL are enabled by launching a 45^0 linearly polarized pump light to the PM Brillouin gain fiber, so that two lasing peaks are generated in fast axis and slow axis respectively. It is found that the spectra of the BRFL varies in either same or different manner between the orthogonal polarizations due to the environmental perturbation and gain competition. Discrete random lasing modes of the BRFL are demonstrated, with the probability distribution of the lasing frequency affected by spectral hole burning of the Brillouin gain. Pearson correlation coefficient of the spectra of the BRFL are analyzed, reflecting the internal correlations

between different part of the spectra. The analysis of the dynamic frequency drift enhances our understanding of the properties of the BRFL for its further applications in distributed sensing and high precision metrology.

1.3 Thesis outline

This thesis contains six chapters and is organized as follows:

Chapter 1 reviews the background of the RFL, including different types of RFLs, its development and applications. Thesis motivation, contribution and outline are also given in this chapter.

Chapter 2 presents a theoretical description involved in BRFL. The theory includes Rayleigh scattering theory, Brillouin scattering theory, light localization theory in random medium, noise source analysis in RFLs and laser property characterization method that are used in the thesis.

Chapter 3 presents a detection method of the acoustic wave in BRFL and the detection results are analyzed. The intrinsic spectral width of the acoustic wave is measured by using the continuous probe light, while the intensity statistics of the distributed acoustic wave is characterized by the pulsed probe light based on OTDR technique.

Chapter 4 studies the output characteristics of BRFL enabled by artificially controlled random mediums. Two types of artificial random mediums are investigated in this chapter. One is the FBG array with varied length and random spacing, and the other is RFG inscribed by femtosecond laser with random periods.

Chapter 5 proposes and demonstrates a low noise BRFL that are insensitive to the environmental perturbation. The BRFL is based on a PM RFG which can reduce the mode number of BRFL and tolerate environmental perturbation. OFDR method is used to characterize the property of the RFG.

Chapter 6 characterizes the dynamic frequency drift of a dual-wavelength BRFL with orthogonal polarization. Relative frequency drift of the BRFL are statistically analyzed. Pearson correlation coefficient of the spectra are calculated to reflect the internal correlations of the spectrum of the BRFL.

Chapter 7 concludes all the work in this thesis and proposes possible directions for future research.

Chapter 2 Theory of BRFL

2.1 Introduction

BRFL is a kind of one dimensional RFL based on SBS as the gain mechanism. Different from conventional fiber lasers that have fixed cavity length, the distributed random scattering in RFL creates a large amount of random modes, leading to various unique laser properties. At the same time, narrow linewidth of lasing spikes was previously reported due to the combined Brillouin gain and Rayleigh scattering mechanism. In order to better understand and further improve the performance of BRFL, it is important to study the fundamental lasing mechanism behind BRFL. In this chapter, the theory of BRFL is summarized in three sections. First, the mechanism of light scattering originated from inhomogeneity of the medium and the SBS effect are presented. In the microscopic view, light scattering is the radiation from induced oscillating dipoles. When the light propagates in the one dimensional random medium, light localization occurs which manifests as the exponential intensity decay rather than linear intensity decay. The SBS process is described as light scattered by the sound wave in the fiber, which is induced by the dynamic refractive index modulation of a pump and probe interference pattern due to the electrostriction effect. Then, the spectral properties of the Rayleigh scattering and noise source of RFL are analyzed theoretically. Due to the random phase superposition, the spectral linewidth of Rayleigh scattering in ultra-long fibers is determined by the loss that is on the order of several kHz. Thermal noise induced frequency noise of RFL is analyzed, where the $1/f$ noise is due to the additional heat generated by the spontaneous emission. At last, the characterization methods of the intensity noise, frequency noise and linewidth of a laser are described. The linewidth of BRFL is measured by delayed self-heterodyne (DSH) method, while the frequency noise is measured by a 3×3 fiber interferometer.

2.2 Random scattering and SBS

2.2.1 Random scattering from inhomogeneity

Light scattering in the medium results from superposition of the electromagnetic field generated by the dipole radiation of molecules. If the optical properties of the medium are completely homogeneous, the superposition of the radiation only has constructive interference at exact forward direction. Due to the destructive interference at other directions, scattering cannot occur in a completely homogeneous medium. However, inhomogeneity of the medium disturbs the interference condition of radiation, leading to light scattering in other directions. When an electric field is incident on a molecule whose dimensions are much smaller than the wavelength of the light, the molecule develops the dipole moment [167]:

$$\tilde{\mathbf{p}} = \mathbf{p}e^{-i\omega t} + c.c. = \varepsilon_0 \alpha(\omega)\mathbf{E_0}e^{-i\omega t} + c.c. \tag{2.1}$$

where $\mathbf{p}$ is the complex amplitude of the dipole moment, ε_0 is the permittivity in vacuum, $\alpha(\omega)$ is the polarizability of the molecule, $\mathbf{E_0}$ is the complex amplitude of the incident electric field, ω is the optical frequency, t is the time, and *c.c.* denotes the complex conjugation and the bold font in the equation denotes the vector. The electric field and magnetic field produced by the oscillating dipole at the position of $\mathbf{r}$ can be expressed as:

$$\begin{aligned}\tilde{\mathbf{E}} &= \frac{1}{4\pi\varepsilon_0}\left\{\frac{\omega^2}{c^2 r}(\mathbf{r}\times\mathbf{p})\times\mathbf{r} + \left(\frac{1}{r^3} - \frac{i\omega}{cr^2}\right)\left[3\mathbf{r}(\mathbf{r}\cdot\mathbf{p}) - \mathbf{p}\right]\right\}e^{\frac{i\omega r}{c}}e^{-i\omega t}\\ \tilde{\mathbf{B}} &= \frac{\omega^2}{4\pi\varepsilon_0 c^3}(\mathbf{r}\times\mathbf{p})\left(1 - \frac{c}{i\omega r}\right)\frac{e^{i\omega r/c}}{r}e^{-i\omega t}\end{aligned} \tag{2.2}$$

where c is the light velocity in vacuum and $r = |\mathbf{r}|$ is the distance from the dipole to the observed point. The time varying electromagnetic field leads to power radiation, which is given by the Poynting vector as:

$$I_s = \frac{n\omega^4 \varepsilon_0 |\alpha(\omega)|^2 |\mathbf{E}_0|^2}{8\pi^2 c^3 r^2} \sin^2 \phi \tag{2.3}$$

where n is the refractive index of the medium, ϕ is the angle between the induced dipole moment of the molecule and the direction $\mathbf{r}$ to the point of observation, as shown in Figure 2-1.

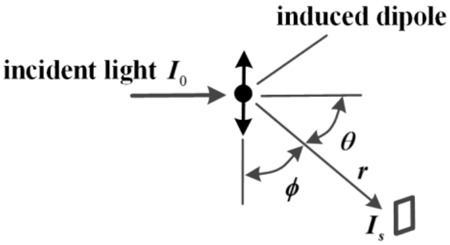

Figure 2-1 Geometry of light scattering from an molecule induced dipole.

The differential scattering cross section of a molecule is defined as [167]:

$$\frac{d\sigma}{d\Omega} = \frac{1}{I_0}\frac{dP}{d\Omega} = \frac{I_s r^2}{I_0} \tag{2.4}$$

where P is the total power of the radiation scattered by the molecule, Ω is the solid angle, and $I_0 = 2nc\varepsilon_0 |\mathbf{E}_0|^2$ is the intensity of light that is incident on the molecule. If we substitute Equation 2.3 to Equation 2.4, the differential cross section can be expressed as:

$$\frac{d\sigma}{d\Omega} = \frac{1}{16\pi^2}\frac{\omega^4}{c^4}|\alpha(\omega)|^2 \sin^2 \phi \tag{2.5}$$

In the classical theory, the Lorentz model uses the simple harmonic oscillator to describe the optical properties of the medium. The polarizability of an atom in the classical theory is given by:

$$\alpha(\omega) = \frac{e^2 / m\varepsilon_0}{\omega_0^2 - \omega^2 - 2i\omega\gamma} \tag{2.6}$$

where ω_0 is the resonance frequency, γ is the dipole damping rate, and m is the mass of the electron. Using the expression of the polarizability in Equation 2.6, we can calculate the scattering cross section by integrating $d\sigma / d\Omega$ over all solid angles:

$$\begin{aligned} \sigma &= \int_{4\pi} d\Omega \frac{d\sigma}{d\Omega} = \frac{8\pi}{3} \frac{1}{16\pi^2} \frac{\omega^4}{c^4} \left|\alpha(\omega)\right|^2 \\ &= \frac{8\pi}{3} \left(\frac{e^2}{4\pi\varepsilon_0 mc^2} \right)^2 \frac{\omega^4}{(\omega_0^2 - \omega^2)^2 + 4\omega^2\gamma^2} \end{aligned} \tag{2.7}$$

If the optical frequency is much smaller than the resonance frequency $\omega \ll \omega_0$, the scattering cross section is simplified to:

$$\sigma = \frac{8\pi}{3} \left(\frac{e^2}{4\pi\varepsilon_0 mc^2} \right)^2 \frac{\omega^4}{\omega_0^4} \tag{2.8}$$

Scattering in the limit of $\omega \ll \omega_0$ is known as Rayleigh scattering. Equation 2.8 reveals that the cross section of Rayleigh scattering is determined by the fourth power of the optical frequency. In optical fibers, Rayleigh scattering is a fundamental loss mechanism that originates from the density variations of the silica fiber due to the manufacture flaw. The typical value of the loss in current standard telecommunication SMF is 0.2 dB/km. Because the intrinsic density variation of the fiber is static and non-propagating, Rayleigh scattering is an elastic process which means that energy of the scattered photons is equal to the energy of incident photons. Due to the waveguide confinement of the optical fiber, Rayleigh scattering in the fiber can only be detected at the counter-propagating direction with respect to the incoming light.

2.2.2 Light localization in random medium

When the light propagates in a random medium, the light wave nature leads to the localization effect due to multi scattering and coherent interference. The inhomogeneity of the fiber creates many “frozen scattering centers” that reflect light with random amplitude and phase. Considering the light travelling along a one dimensional random medium consisting of arbitrary combination of scattering centers, the transmission and reflection amplitude of light after the whole medium can be calculated by the recursion method. Assume that T_s and R_s are the transmission and reflection amplitudes of the s-th “frozen scattering center”, the combined transmission amplitude T_{12} for the first two random scattering centers is a geometrical series of the sum of all reflected and transmitted waves [168]:

$$T_{12} = T_1T_2 + T_1R_2R_1T_2 + T_1R_2R_1R_2R_1T_2 + \cdots = \frac{T_1T_2}{1-R_1R_2} \tag{2.9}$$

If all the wave interactions are regarded as incoherent, the field amplitude in Equation 2.9 can be replaced by the intensity:

$$\tau_{12} = \frac{\tau_1\tau_2}{1-\rho_1\rho_2} \tag{2.10}$$

where $\tau_s = |T_s|^2$ is the intensity transmissivity of the s-th scattering center and $\rho_s = |R_s|^2$ is the intensity reflectivity of the s-th scattering center. Using the relationship of $\tau_1 + \rho_1 = \tau_2 + \rho_2 = 1$, Equation 2.10 can be written as:

$$\frac{1}{\tau_{12}} = \frac{1}{\tau_1} + \frac{1-\tau_2}{\tau_2} \tag{2.11}$$

If the intensity transmissivity of all the scattering centers are the same, Equation 2.11 can be applied iteratively. The transmission of the whole random medium is:

$$\tau_N = \frac{\tau}{\tau + N(1-\tau)} \qquad (2.12)$$

where τ is the average intensity transmissivity of the scattering center, and N is the total number of “frozen scattering centers”. Equation 2.12 manifests that the transmitted intensity decreases linearly as the number of scattering centers increases when the phase superposition is not considered in the multi scattering of optical waves. However, for a coherent laser propagating in the random medium, the light interference lead to exponential decay of the wave intensity, indicating localization of light in the random medium.

For the coherent light, Equation 2.9 can be rewritten as the average of the logarithmic of the transmitted intensity over the random phase:

$$\left\langle \ln\left(\left|T_{12}\right|^2\right)\right\rangle = \ln\left(\left|T_1\right|^2\right) + \ln\left(\left|T_2\right|^2\right) - \frac{1}{\pi}\mathrm{Re}\left[\int_0^{2\pi} d\phi \ln\left(1-\left|R_1R_2\right|e^{i\phi}\right)\right] \qquad (2.13)$$

Because $\left|R_1R_2\right| < 1$, the integral vanishes by expanding the logarithm in Equation 2.13:

$$\left\langle \ln\left(\left|T_{12}\right|^2\right)\right\rangle = \ln\left(\left|T_1\right|^2\right) + \ln\left(\left|T_2\right|^2\right) \qquad (2.14)$$

Using iteration for all the scattering centers in the random medium, the total transmission of the whole random medium can be expressed as:

$$\tau_N = \exp\left(\sum_{s=1}^{N} \ln \tau_s\right) \approx \tau^N \qquad (2.15)$$

The result in Equation 2.15 shows that the transmissivity of the random medium decrease exponentially rather than linearly as the number of scattering centers increases. The transmission through a set of randomly spaced scatters in a one-dimensional system only includes the multiplication of single scatters transmission because the destructive interference of light in the random medium cancels the effect of multiple reflections. Figure 2-2 shows the transmissivity difference of the coherent scattering with phase superposition and incoherent scattering without phase superposition under the condition of $\tau = 0.99$. Due to the localization of light, the travelling time of photons in the random medium increases, which is beneficial to generate long lifetime photons and high coherent RFLs. The derivation of the light localization in random medium was inspired from past contributions in [168].

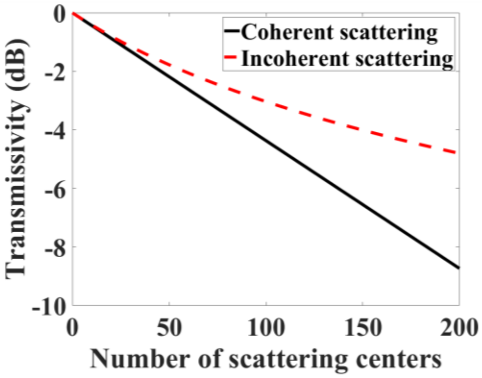

Figure 2-2 Transmissivity of light as the increase of the scattering centers [calculated from Equation 2.15 (black) and Equation 2.12 (red)].

2.2.3 SBS in optical fibers

The SBS in material originates from the nonlinear interaction among the pump wave, Stokes wave, and acoustic wave through the process of electrostriction. Electrostriction induce density variation of the material through the electrostrictive pressure, which is given by [167]:

$$\Delta p = -\frac{1}{2}\varepsilon_0 \gamma_e E^2 \tag{2.16}$$

where ε_0 is the permittivity in vacuum, E is the electric field, $\gamma_e = \rho(\partial\varepsilon / \partial\rho)$ is the electrostrictive constant, and ρ is the density of the material. The density change of the material is calculated as:

$$\Delta\rho = -\left(\frac{-\partial\rho}{\partial p}\right)\Delta p = \frac{1}{2}\varepsilon_0 \rho C \gamma_e E^2 \tag{2.17}$$

where $C = \rho^{-1}(\partial\rho / \partial p)$ is the compressibility of the material. The material density variation in an optical fiber propagates as the acoustic wave:

$$\tilde{\rho}(z,t) = \rho_0 + \left[\rho(z,t) e^{i(qz - \Omega t)} + c.c. \right] \tag{2.18}$$

where ρ_0 is the mean density of the fiber, $q = |\mathbf{q}|$ is the wave vector of the acoustic wave, and Ω is the frequency of the acoustic wave. The pump wave and Stokes wave are expressed as:

$$\tilde{E}_p(z,t) = A_p(z,t) e^{i(k_p z - \omega_p t)} + c.c. \tag{2.19}$$

$$\tilde{E}_s(z,t) = A_s(z,t) e^{i(-k_s z - \omega_s t)} + c.c. \tag{2.20}$$

where $A_p(z,t)$ and $A_s(z,t)$ are the amplitude of the pump wave and probe wave respectively. $k_p = |\mathbf{k_p}|$ and $k_s = |\mathbf{k}_s|$ are wave vectors of the pump wave and probe wave respectively. ω_p and ω_s are the frequency of the pump wave and the probe wave respectively. According to the conservation of momentum and conservation of energy, the frequency relationship and wave vector relationship among the pump wave, the Stokes wave and the acoustic wave follow the relationship:

$$\Omega = \omega_p - \omega_s, \mathbf{q} = \mathbf{k_p} - \mathbf{k_s} \tag{2.21}$$

The frequency of the acoustic wave is related to the acoustic wave vector by the phonon dispersion relationship:

$$\Omega = qv \approx 2vk_p \sin(\theta / 2) \tag{2.22}$$

where v is the velocity of the acoustic wave, and θ is the angle between the propagation direction of the pump wave and the Stokes wave. Therefore, the frequency shift of the Stokes light reaches maximum when $\theta = 180^0$ and vanishes when $\theta = 0^0$. In the fiber, SBS only occurs in the backward direction if the guided acoustic wave is not considered.

In order to find the solution of the pump wave, Stokes wave and acoustic wave, the material density variation is assumed to obey the acoustic wave equation:

$$\frac{\partial^2 \tilde{\rho}}{\partial t^2} - \Gamma' \nabla^2 \frac{\partial \tilde{\rho}}{\partial t} - v^2 \nabla^2 \tilde{\rho} = \nabla^2 (\Delta p) \tag{2.23}$$

where Γ' is the acoustic wave damping parameter. The pump wave and probe wave are described by the wave equation:

$$\frac{\partial^2 \tilde{E}_i}{\partial z^2} - \left(\frac{n}{c}\right)^2 \frac{\partial^2 \tilde{E}_i}{\partial t^2} = \frac{1}{\varepsilon_0 c^2} \frac{\partial^2 \tilde{P}_i}{\partial t^2}, i = s, p \tag{2.24}$$

The nonlinear polarization induced by the density variation is given by:

$$\tilde{P} = \varepsilon_0 \Delta \chi \tilde{E} = \varepsilon_0 \Delta \varepsilon \tilde{E} = \varepsilon_0 \rho_0^{-1} \gamma_e \tilde{\rho} \tilde{E} \tag{2.25}$$

Combining Equation 2.18-2.20, Equation 2.23-2.25 and Equation 2.16 and using the slow varying amplitude approximation, the coupled equation of the pump wave and probe wave can be written as:

$$\frac{\partial A_p}{\partial z} + \frac{n}{c} \frac{\partial A_p}{\partial t} = \frac{i \omega_p \gamma_e}{2 n c \rho_0} \rho A_s \tag{2.26}$$

$$-\frac{\partial A_s}{\partial z} + \frac{n}{c} \frac{\partial A_s}{\partial t} = \frac{i \omega_s \gamma_e}{2 n c \rho_0} \rho^* A_p \tag{2.27}$$

where A_p and A_s are the complex amplitude of the pump wave and probe wave respectively. If continuous pump light with a power above the SBS threshold is launched into the optical fiber, under steady state, the coupled wave equation of 2.26 and 2.27 can be simplified to:

$$\frac{dI_p}{dz} = -gI_pI_s \tag{2.28}$$

$$-\frac{dI_s}{dz} = gI_pI_s \tag{2.29}$$

where g is the Brillouin gain factor:

$$g = g_p \frac{\left(\Gamma_B / 2\right)^2}{\left(\Omega_B - \Omega\right)^2 + \left(\Gamma_B / 2\right)^2} \tag{2.30}$$

with Γ_B is the full width at half maximum (FWHM) of the SBS gain spectrum, g_p is the peak value of the SBS gain given by:

$$g_p = \frac{\gamma_e^2 \omega_p^2}{nvc^3 \rho_0 \Gamma_B} \tag{2.31}$$

2.3 Spectral property and thermal noise of random scattering

2.3.1 Spectral property of Rayleigh scattering

In standard telecom SMFs, light from Rayleigh backscattering can be regarded as a collection of lights reflected by a cascade of multiple small segments at equal geometrical length ΔL. For a fiber with total length of L, the total number of segments $N = L / \Delta L$. At *k*th segment, the light of Rayleigh backscattering can be expressed as:

$$\rho_k = a_k e^{-i\theta_k} \tag{2.32}$$

where a_k is a random complex amplitude and θ_k a random phase variable. The total backward radiation within the fiber can be written as:

$$E_R = \sum_{k=1}^{N} \rho_k e^{-\alpha k \Delta L} e^{-i2\pi n f k \Delta L / c} \tag{2.33}$$

where α is the attenuation coefficient of the optical fiber and f is the optical frequency of light. Because θ_k and $|a_k|$ are random independent variables, it is reasonable to have following relationships [169]:

$$\left\langle e^{i\theta_k} \right\rangle = 0 \tag{2.34}$$

$$\left\langle e^{i(\theta_k - \theta_l)} \right\rangle = \delta_{kl} \tag{2.35}$$

$$\left\langle a_k^2 \right\rangle = \beta \Delta L \tag{2.36}$$

where $\langle \ \rangle$ denote the mean value of a random variable, and β is the backscattering strength per length. According to Equation 2.34 to Equation 2.36, one can get:

$$\left\langle \rho_k \right\rangle = \left\langle a_k \right\rangle \left\langle e^{-i\theta_k} \right\rangle = 0 \tag{2.37}$$

$$\begin{aligned} \left\langle \rho_k^* \rho_l \right\rangle &= \left\langle a_k^* a_l e^{i(\theta_k - \theta_l)} \right\rangle \\ &= \left\langle a_k^* a_l \right\rangle \left\langle e^{i(\theta_k - \theta_l)} \right\rangle \\ &= \left\langle a_k^* a_l \right\rangle \delta_{kl} = \beta \Delta L \delta_{kl} \end{aligned} \tag{2.38}$$

The expected value of the beat note of Rayleigh scattering at frequency f and frequency $f + F$ can be expressed as:

$$\begin{aligned} \left\langle B(F) \right\rangle &= \left\langle E_R^*(f) E_R(f+F) \right\rangle \\ &= \left\langle \sum_{k=1}^{N} \rho_k^* e^{-\alpha k \Delta L} e^{i 2\pi n f k \Delta L / c} \sum_{l=1}^{N} \rho_l e^{-\alpha l \Delta L} e^{-i 2\pi n (f+F) l \Delta L / c} \right\rangle \\ &= \sum_{k,l=1}^{N} \left\langle \rho_k^* \rho_l \right\rangle e^{-\alpha (k+l) \Delta L} e^{i 2\pi n f (k-l) \Delta L / c} e^{-i 2\pi n F l \Delta L / c} \\ &= \sum_{k,l=1}^{N} \beta \Delta L \delta_{kl} e^{-\alpha (k+l) \Delta L} e^{i 2\pi n f (k-l) \Delta L / c} e^{-i 2\pi n F l \Delta L / c} \\ &= \beta \sum_{k=1}^{N} \Delta L e^{-\alpha k \Delta L} e^{-i 2\pi n F k \Delta L / c} \end{aligned} \tag{2.39}$$

In the limit $\Delta L \to 0, L \to \infty$, the summation becomes an integral:

$$\langle B(F) \rangle = \beta \int_0^{\infty} e^{-\alpha x} e^{-i2\pi n F x / c} dx = \frac{1}{\alpha + i2\pi n F / c} \qquad (2.40)$$

In order to calculate the relative intensity of the beat signal, $\left| \langle B(F) \rangle \right|$ is normalized by its peak value $\left| \langle B(0) \rangle \right|$:

$$\frac{\left| \langle B(F) \rangle \right|^2}{\left| \langle B(0) \rangle \right|^2} = \frac{1}{1 + (2\pi n F / \alpha c)^2} = \frac{1}{1 + (F / \Gamma)^2} \qquad (2.41)$$

where $\Gamma = \alpha c / 2\pi n$ represents the linewidth of the beat signal, which is determined by the loss and refractive index of the fiber. The α value and refractive index in typical low loss fibers are around $5 \times 10^{-5} m^{-1}$ and 1.45 respectively, corresponding to a linewidth of $\sim 1.65 kHz$. As F exceeds $1.65 kHz$, the intensity of the beat signal decreases rapidly, indicating that statistical correlation of the Rayleigh scattering light between frequency f and frequency $f + F$ disappears. At the same time, Equation 2.41 shows that the linewidth of the beat pattern increases as fiber loss increases. The physical reason for the loss dependent spectral width comes from the interference of light. The random scattering medium can be regarded as a superposition of a large number of random FP cavities where the cavity length determines the linewidth of the spectral peak. In the long random scattering medium, the loss of the fiber determines the effective length of the fiber that can generate a visible interference signal. The smaller the loss, the longer effective length of the scattering fiber, which further leads to smaller spectral linewidth. The results manifest that the accumulated Rayleigh scattering in ultra-long optical fiber creates randomly distributed narrow linewidth spikes in the spectral domain, providing a theoretical background to study the spectral properties of RFLs enabled by random distributed scattering.

2.3.2 Thermal induced frequency noise of RFL

The fundamental frequency noise limit of a laser is affected by the spontaneous emission, which is known as the Schawlow-Townes noise limit. However, thermal perturbations in the laser cavity leads to a noise limit that is significantly higher than the Schawlow-Townes limit. Therefore, the thermal induced frequency noise of RFL is analyzed in this part. Temperature variations lead to refractive index changes of the fiber material, which further change the distributed cavity properties and result in frequency deviation of the laser. The frequency deviation of the laser that depends on the temperature change can be written as:

$$\Delta\upsilon(t,\mathbf{r}) = -\upsilon\left(\frac{d\varepsilon}{dT}+\frac{1}{n}\frac{dn}{dT}\right)\Delta T(t,\mathbf{r}) = -\upsilon p\Delta T(t,\mathbf{r}) \tag{2.42}$$

where p containing the strain ε and refractive index n is known as the thermo-optic coefficient of the fiber. The autocorrelation function of the optical frequency is given by:

$$\left\langle\Delta\upsilon(t,\mathbf{r})\Delta\upsilon(t+\Delta t,\mathbf{r})\right\rangle = \upsilon^2 p^2\left\langle\Delta T(t,\mathbf{r})\Delta T(t+\Delta t,\mathbf{r})\right\rangle \tag{2.43}$$

Taking Fourier transformation of Equation 2.43, the left hand side is the frequency noise spectrum according to the Wiener-Khinchin theorem, which can be expressed as:

$$S_{\Delta\upsilon}(\omega) = \upsilon^2 p^2 S_{\Delta T}(\omega) \tag{2.44}$$

Therefore, the question to solve the frequency noise spectrum of lasers (left hand side of Equation 2.44) is transformed to the question to solve the frequency noise spectrum of random temperature fluctuation (right hand side of Equation 2.44). The thermal fluctuations of the optical fiber are governed by the inhomogeneous Langevin heat diffusion equation:

$$c_v\Delta\dot{T}(t,\mathbf{r}) - \kappa_t\nabla^2\Delta T(t,\mathbf{r}) = -\nabla\cdot\mathbf{h} \tag{2.45}$$

where c_v is the specific heat at a constant material element, κ_t is the thermal conductivity, and $\mathbf{h}$ is the random Langevin heat current that acts as a source of energy fluctuations within the given material element. The source of the energy fluctuations at equilibrium state comes from the random exchanges of energy between neighboring elements due to the heat flow, which are uncorrelated in space and time:

$$\left\langle h_i(\omega,\mathbf{k})h_j^*(\omega',\mathbf{k}')\right\rangle = \frac{\kappa_t K_B T^2}{8\pi^4}\delta(\omega-\omega')\delta^3(\mathbf{k}-\mathbf{k}') \tag{2.46}$$

where K_B is the Boltzmann constant. Equation 2.45 combined with Equation 2.46 was derived in [170] in detail to solve the frequency noise spectrum of the temperature fluctuation. Considering the geometry distribution of the fiber laser with effective cavity length of L and mode field radius of a, the laser frequency noise contributed by the random heat flow is given by:

$$S_{\upsilon,h}(\omega) = \frac{2\upsilon^2 p^2}{L}\frac{K_B T^2}{2\pi\kappa_t}\mathrm{Re}\left[\int_z^\infty \frac{e^{-t}}{t}dt\right] \tag{2.47}$$

where $z = ik_h^2 a^2/4\exp(ik_h^2 a^2/4)$ and $k_h^2 = \omega c_\upsilon/\kappa_t$ is the wavenumber of the thermal wave. The model can describe the laser frequency noise at the high frequency range. However, at low frequency, the $1/f$ noise is not predicted by the Langevin noise source of random heat flow, as shown in Figure 2-3.

To explain the $1/f$ noise, the heat dissipation induced by the spontaneous emission of photons was studied in [171]. Another kind of noise source is then added to the inhomogeneous heat diffusion equation:

$$c_v\Delta\dot{T}(t,\mathbf{r}) - \kappa_t\nabla^2\Delta T(t,\mathbf{r}) = -\nabla\cdot\mathbf{h}+Q \tag{2.48}$$

where Q represents the average heat dissipation per unit volume caused by the spontaneous emission. The frequency noise of the laser induced by the heat dissipation Q from spontaneous emission is given by:

$$S_{\upsilon,Q}(\omega) = -\frac{\pi^2 \upsilon^2 L^{-1} Q}{2\omega^2 c_\upsilon^2} \mathrm{Im}\left[\int_z^\infty \frac{e^{-t}}{t} dt\right] \tag{2.49}$$

Figure 2-3 compares the theoretical frequency noise of an RFL based on Equation 2.47 and 2.49. The theoretical prediction agrees well with measurement results after considering the spontaneous emission induced additional thermal variations. The mechanism of the additional heat induced by the spontaneous emission relies on the entropy change of the ground state of the atoms. The ground state consists of a collection of closely spaced states of energy, which can be called the absorption manifold. It is assumed that no radiative transitions at wavelengths comparable to the laser transition occurs between states within the manifold. The entropy variations within the manifold induce additional released heat governed by the equation $\Delta Q = T\Delta S$. When compared with the conventional thermal noise caused by random heat current, the additional heat caused by the spontaneous emission is a kind of non-equilibrium transport process rather than equilibrium thermal noise. Mathematically, the non-equilibrium source term in the inhomogeneous heat equation lead to $1/f$ noise or flicker noise, which interprets the origin of the $1/f$ noise in RFLs.

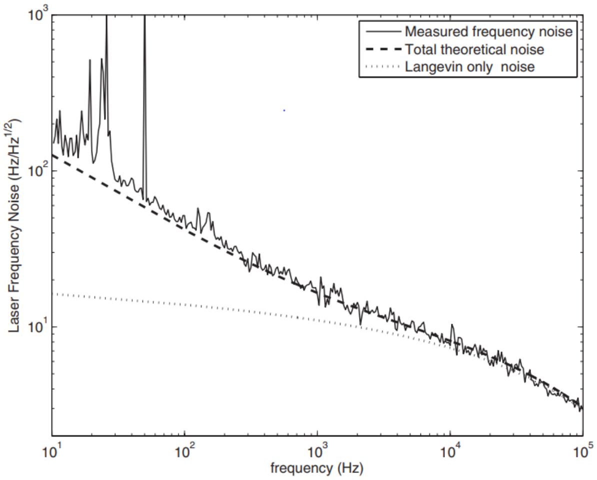

Figure 2-3 Comparison of theoretical thermal induced laser frequency noise based on Equation 2.49 and 2.47 with experimental frequency noise of an RFL [171].

2.4 Characterization method of laser property

2.4.1 RIN measurement

RIN is an important parameter to evaluate the performance of a laser. The fundamental noise source for intensity fluctuation of a laser is the random spontaneous emission from the gain medium, leading to random intensity fluctuations of the laser output. Besides the intensity fluctuation originated from spontaneous emission, the large amount of random modes competition is a dominant noise source in distributed RFLs due to the wavelength non-selectivity of the random medium. At the same time, the Rayleigh scattering generated by the long length fiber is naturally susceptible to environmental perturbation, such as temperature fluctuation and vibration. Therefore, the amplitude and phase of light reflected by each small scattering center are changing with time, which further lead to the variation of output intensity. The output intensity of a laser can be written as the summation of the average output intensity and its noise fluctuation:

$$I(t) = I_0 + \Delta I(t) \tag{2.50}$$

The RIN is defined as the ratio between the intensity (power) of noise fluctuation and the average output intensity (power):

$$RIN = \frac{\langle \Delta I(t) \rangle}{I_0} = \frac{\langle \Delta P(t) \rangle}{P_0} \tag{2.51}$$

The spectral density of the intensity noise can be calculated through the Fourier transform of the autocorrelation function of the power fluctuation [172]:

$$RIN(f) = \frac{1}{P_0^2} \int_{-\infty}^{+\infty} \langle \Delta P(t) \Delta P(t+\tau) \rangle e^{i2\pi f\tau} d\tau \tag{2.52}$$

In the experiment, the output intensity of the laser can be detected by a wide band photodetector. Because of the square law detection principle of the photodetector, the current generated by the photodetector is proportional to the power or intensity of the light rather than the field amplitude. In order to get the spectral density of the intensity noise, the electrical signal from the photodetector is either analyzed by an electrical spectrum analyzer (ESA), or alternatively recorded by an oscilloscope and then processed manually by the Fourier transform, as shown in Figure 2-4.

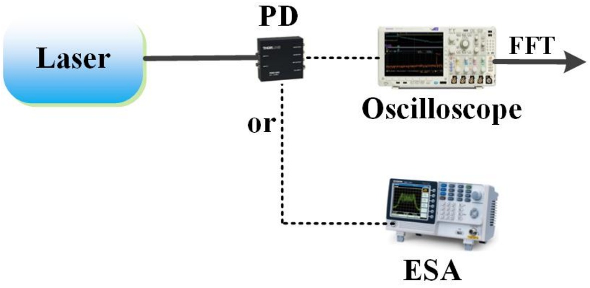

Figure 2-4 Schematic of the RIN measurement setup.

2.4.2 Laser linewidth measurement

High precision linewidth characterization can be realized by the delayed self-heterodyne (DSH) method based on the Mach-Zehnder interferometer (MZI), which was proposed in 1980s by T. Okoshi [173]. The basic experimental configuration of the DSH method is shown in Figure 2-5. Light from the laser under test is split into two parts by a coupler with 95/5 splitting ratio and then launched into two paths of the MZI. In one path, a sufficient long delay fiber with a length longer than the laser coherence length is used to decorrelate the light from another path. In order to compensate the light loss in the delay fiber, the arm of the coupler with a 95% power ratio is connected to the long length delay fiber. In another path, the frequency of light is shifted by an acoustic optical modulator (AOM), thus the beat signal of the light in the two paths is centered at the frequency of the shifted frequency. The beat signal is detected by a photodetector and analyzed by an ESA. At the second coupler, the power of the two paths light should be approximately equal to ensure the optimized contrast of the beat signal measured on the ESA. In practical operations, an optical attenuator and a polarization controller (PC) are inserted into one beam of the MZI for fine control of the transmitted light power and polarization state to obtain the optimum contrast of the beat signal.

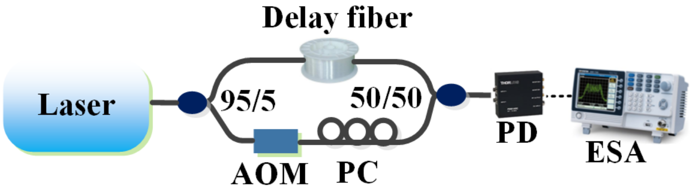

Figure 2-5 Schematic of the DSH method for laser linewidth measurement.

Next, we proceed with a theoretical analysis of the DSH method. The optical field of the laser is modeled as a quasi-monochromatic wave with a constant amplitude and a phase variation as:

$$E(t) = E_0 e^{i[2\pi\upsilon_0 t + \phi(t)]} \tag{2.53}$$

where υ_0 is the optical frequency of the laser under test and $\phi(t)$ are the laser phase fluctuations. The optical field at the output of the MZI is a superposition of the delayed light and the frequency shifted light:

$$E_T(t) = E_1 e^{i[2\pi(\upsilon_0 + f_M)t + \phi(t)]} + E_2 e^{i[2\pi\upsilon_0(t+\tau_d) + \phi(t+\tau_d)]} \tag{2.54}$$

where E_1 and E_2 are the field amplitude of the light after passing through the two arms, f_M is the modulation frequency of the AOM, τ_d is the optical delay time in the fiber delay line, and $\phi(t+\tau_d)$ are the time-delayed phase fluctuations. The intensity of the optical beat signal was detected by the photodetector and then converted to photocurrent. The autocorrelation function of the photocurrent can be written as [174, 175]:

$$C(\tau) = RG_E^1(\tau)\delta(\tau) + R^2 G_E^2(\tau) \tag{2.55}$$

where R is the responsivity of the photodiode, $G_E^1(\tau)$ and $G_E^2(\tau)$ are the first order and second order correlation function of the optical field:

$$G_E^1(\tau) = \left\langle E^*(t)E(t+\tau) \right\rangle \tag{2.56}$$

$$G_E^2(\tau) = \left\langle E(t)E^*(t)E(t+\tau)E^*(t+\tau) \right\rangle \tag{2.57}$$

Because the first term of Equation 2.55 is a constant value, we only consider the contribution of the second term of Equation 2.55. Combining Equation 2.55 and Equation 2.57, we can get:

$$G_E^2(\tau) = \left\langle \begin{array}{l} \left(E_1 e^{i[2\pi(\upsilon_0 + f_M)t + \phi(t)]} + E_2 e^{i[2\pi\upsilon_0(t+\tau_d) + \phi(t+\tau_d)]} \right) \cdot \\ \left(E_1 e^{-i[2\pi(\upsilon_0 + f_M)t + \phi(t)]} + E_2 e^{-i[2\pi\upsilon_0(t+\tau_d) + \phi(t+\tau_d)]} \right) \cdot \\ \left(E_1 e^{i[2\pi(\upsilon_0 + f_M)(t+\tau) + \phi(t+\tau)]} + E_2 e^{i[2\pi\upsilon_0(t+\tau_d+\tau) + \phi(t+\tau_d+\tau)]} \right) \cdot \\ \left(E_1 e^{-i[2\pi(\upsilon_0 + f_M)(t+\tau) + \phi(t+\tau)]} + E_2 e^{-i[2\pi\upsilon_0(t+\tau_d+\tau) + \phi(t+\tau_d+\tau)]} \right) \end{array} \right\rangle \tag{2.58}$$

The average value of the term $e^{\pm i 2\pi f_M t}$ that contains time is 0. Therefore, Equation 2.58 is simplified to:

$$\begin{aligned} G_E^2(\tau) &= (E_1^2 + E_2^2)^2 + 2E_1^2 E_2^2 \cos(2\pi f_M \tau) \left\langle e^{j[\phi(t+\tau_d+\tau) - \phi(t+\tau_d)]} \right\rangle \\ &= (E_1^2 + E_2^2)^2 + 2E_1^2 E_2^2 \cos(2\pi f_M \tau) e^{-\frac{1}{2}\left\langle \Delta\phi^2(\tau) \right\rangle} \end{aligned} \tag{2.59}$$

where $\Delta\phi(\tau) = \phi(t+\tau_d+\tau) - \phi(t+\tau_d)$. A reasonable assumption is then made that the mean square phase jitter of the laser increases linearly with the time delay as:

$$\left\langle \Delta\phi^2(\tau) \right\rangle = 2\pi\Delta\upsilon |\tau| \tag{2.60}$$

where $\Delta\upsilon$ is the 3 dB linewidth of the laser. Therefore, Equation 2.59 can be further written as:

$$G_E^2(\tau) = (E_1^2 + E_2^2)^2 + \begin{cases} 2E_1^2E_2^2\cos(2\pi f_M\tau)e^{-2\pi\Delta\upsilon\tau}, |\tau| < \tau_d \\ 2E_1^2E_2^2\cos(2\pi f_M\tau)e^{-2\pi\Delta\upsilon\tau_d}, |\tau| > \tau_d \end{cases} \tag{2.61}$$

According to the Wiener-Khinchine theorem, the spectrum of the photocurrent is the Fourier transform of its autocorrelation function:

$$\begin{aligned} S_i(f) &= \int_{-\infty}^{+\infty} C(\tau)e^{-2i\pi f\tau}d\tau \\ &= R^2\left\{\begin{aligned} &\left(E_1^2+E_2^2\right)^2\delta\left(\frac{f}{\Delta\upsilon}\right) + E_1^2E_2^2e^{-2\pi\Delta\upsilon\tau_d}\delta\left(\frac{f-f_M}{\Delta\upsilon}\right) + E_1^2E_2^2e^{-2\pi\Delta\upsilon\tau_d}\frac{\left(\pi\Delta\upsilon\right)^{-1}}{1+\left(\frac{f-f_M}{\Delta\upsilon}\right)^2} \\ &\cdot\left[e^{2\pi\Delta\upsilon\tau_d} - \frac{2\pi\Delta\upsilon\tau_d\sin\left(\frac{f-f_M}{\Delta\upsilon}\right)}{\left(\frac{f-f_M}{\Delta\upsilon}\right)} + 2\pi\Delta\upsilon\tau_d\cos\left(\frac{f-f_M}{\Delta\upsilon}\right)\right] \end{aligned}\right\} \end{aligned} \tag{2.62}$$

In the DSH method, the time delay τ_d is much larger than the coherent time of the laser, which means $\tau_d \gg \frac{1}{\Delta\upsilon}$. Under this requirement, Equation 2.46 is simplified to:

$$S_i(f) = R^2\left[(E_1^2+E_2^2)^2\delta\left(\frac{f}{\Delta\upsilon}\right) + E_1^2E_2^2\frac{\left(\pi\Delta\upsilon\right)^{-1}}{1+\left(\frac{f-f_M}{\Delta\upsilon}\right)^2}\right] \tag{2.63}$$

Therefore, the spectrum of the photocurrent has a Lorentzian shape with full linewidth at maximum (FWHM) of $2\Delta\upsilon$, which is twice the linewidth of the laser under test. The linewidth of the laser can be characterized by measuring the linewidth of the electrical beat signal in the DSH method.

2.4.3 Frequency noise measurement

The random phase fluctuations $\phi(t)$ in Equation 2.53 correspond to the random frequency fluctuation of the laser:

$$\upsilon_0 + \upsilon(t) = \upsilon_0 + \frac{d\phi(t)}{dt} \tag{2.64}$$

where $\upsilon(t)$ is the instantaneous frequency deviation of the laser. The frequency deviation is assumed to be a stationary (meaning that the probability density function is time invariant) and zero mean random variable. The auto-correlation function of the frequency deviation is written as:

$$C_l(\tau) = \langle \upsilon(t)\upsilon(t+\tau) \rangle = \int_{-\infty}^{+\infty} \upsilon(t)\upsilon(t+\tau)dt \tag{2.65}$$

The spectral property of the frequency noise is the Fourier transform of the autocorrelation function:

$$S_\upsilon(f) = \int_{-\infty}^{+\infty} C_l(\tau) e^{-2i\pi f\tau} d\tau \tag{2.66}$$

In the experiment, the frequency noise of the laser could be measured by an imbalanced symmetric 3×3 coupler fiber interferometer based on demodulation of the phase difference reflected by two arms, as shown in Figure 2-6. The interferometer consists of a commercially available 3×3 optical fiber coupler, a circulator, two Faraday rotator mirrors (FRMs), three photodetectors, and a digital oscilloscope. The laser under test is launched from the left port 1 of the coupler after the circulator and then is split into 3 parts. Two of them are reflected by FRMs with a delay time of τ, and one of them is tightly bent to prevent back reflections. The FRM reflects light with 90^0 rotation of the polarization state to remove the polarization fading of the interferometer.

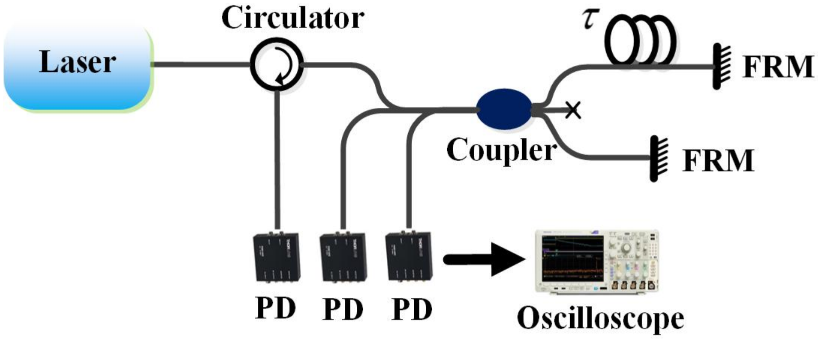

Figure 2-6 Experimental setup for laser frequency noise measurement.

The interference fringes are obtained from the left ports of the coupler and read by a digital oscilloscope. The transfer matrix for the 3×3 coupler is [176]:

$$M_{3\times 3}=\frac{e^{-iKl}}{3}\begin{bmatrix}1 & 1 & 1\\ 1 & 1 & 1\\ 1 & 1 & 1\end{bmatrix}+\frac{e^{iKl}}{3}\begin{bmatrix}2 & -1 & -1\\ -1 & 2 & -1\\ -1 & -1 & 2\end{bmatrix} \tag{2.67}$$

where K is the coupling coefficient, and l is the length of the coupling section. At the same time, the path length difference of the interferometer induce a relative phase shift $\Delta\phi(t)=2\pi\upsilon(t)\tau$, which can be expressed by the transfer matrix as:

$$D=\begin{bmatrix}1 & 0 & 0\\ 0 & 0 & 0\\ 0 & 0 & e^{i\Delta\phi(t)}\end{bmatrix} \tag{2.68}$$

Considering the incident beam of the laser under test is written as $E_{in}=\begin{bmatrix}E(t)\\ 0\\ 0\end{bmatrix}$, the resulting interference field from the interferometer becomes:

$$\begin{aligned}E_{out} &=[M_{3\times 3}][D][M_{3\times 3}]E_{in}\\ &=\frac{E(t)}{9}\begin{bmatrix}\left(3\cos Kl-i\sin Kl\right)^2-4e^{i\Delta\phi}\sin^2 Kl\\ 2i\sin Kl\left(3\cos Kl-i\sin Kl\right)-4e^{i\Delta\phi}\sin^2 Kl\\ 2i\sin Kl\left(3\cos Kl-i\sin Kl\right)\left(e^{i\Delta\phi}+1\right)\end{bmatrix}\end{aligned} \tag{2.69}$$

The 3×3 coupler is made with the relation $Kl = 2\pi/3$ so that the intensity measured on the three photodiodes are:

$$\begin{aligned}
I_1 &= E^*_{out,1}E_{out,1} = \frac{2}{9}\left|E(t)\right|^2\left[1+\cos(\Delta\phi+2\pi/3)\right] \\
I_2 &= E^*_{out,2}E_{out,2} = \frac{2}{9}\left|E(t)\right|^2\left[1+\cos(\Delta\phi-2\pi/3)\right] \\
I_3 &= E^*_{out,3}E_{out,3} = \frac{2}{9}\left|E(t)\right|^2\left(1+\cos\Delta\phi\right)
\end{aligned} \tag{2.70}$$

The phase variation $\Delta\phi(t)$ can then be demodulated from the intensity measured on the photodiodes. The demodulation process is shown in Figure 2-7.

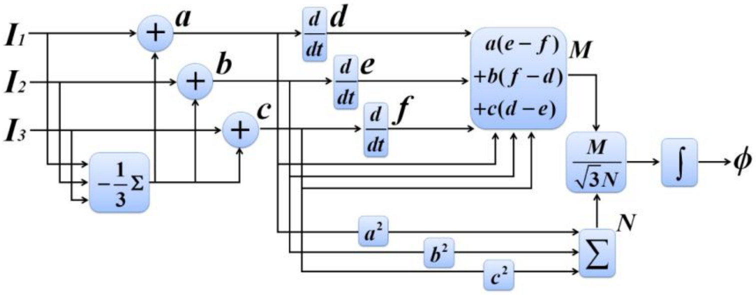

Figure 2-7 Demodulation algorithm of phase change based on 3×3 coupler [177].

After the phase difference demodulation using the method shown in Figure 2-7, the spectrum of the phase difference can be calculated by applying the Fourier transform to the demodulated time varying phase difference. Because $\Delta\phi(t) = 2\pi\Delta\upsilon(t)\tau$, the relationship between the spectrum of phase difference noise and spectrum of optical frequency difference noise is:

$$S_{\Delta\upsilon}(f) = \left(\frac{1}{2\pi\tau}\right)^2 S_{\Delta\phi}(f) \tag{2.71}$$

Further, by using the relationship between the spectrum of optical frequency difference noise and spectrum of optical frequency noise, the frequency noise is expressed as:

$$S_{\upsilon}(f)=\frac{1}{\left[\sin c(\pi f\tau)\right]^{2}}S_{\Delta\upsilon}(f)=\left[\frac{(2\pi\tau)^{-1}}{\sin c(\pi f\tau)}\right]^{2}S_{\Delta\phi}(f) \tag{2.72}$$

2.5 Conclusion

In this chapter, the theory involved in BRFL are presented in three sections. Starting from the fundamental scattering theory, we show that Rayleigh scattering in the fiber is originated from the random refractive index variation due to the fabrication flaw. The strength of the Rayleigh scattering is inversely proportional to the fourth power of the wavelength; thus a shorter wavelength would experience stronger scattering strength. Localization of light is analyzed in the random medium, which lays the foundation for using RFG to provide random feedback for BRFL. SBS is a nonlinear process between the coupled pump wave, Stokes wave and acoustic wave, in which the acoustic wave is described as the dynamic refractive index variation of the fiber. The analysis provides a novel idea for the detection of the acoustic wave in BRFL, which will be shown in Chapter 3. In the second section, the spectral properties of random scattering are analyzed, which can illustrate the narrow linewidth properties of BRFL that were reported before. The influence of the thermal noise, a dominating noise source to the distributed feedback fiber laser, is also briefly presented. Finally, in the third section, the characterization methods and the corresponding principle of the laser properties are analyzed in detail, which will be used to characterize the intensity noise, frequency noise and linewidth of BRFL in the following chapters.

Chapter 3 Acoustic wave detection in BRFL

3.1 Introduction

RFLs have attracted a great deal of attention due to their novel underlying physics and great potential applications. Different from the conventional lasers that require a cavity with a fixed length to trap light, RFLs make use of the multiple scattering of photons in a disordered medium to provide optical feedback. Lasing occurs when the total gain in the random cavity overcomes the total loss. The characteristics of RFLs are determined by the radiation build-up by multiple scattering of the disordered medium and the light amplifying process in the gain medium, resulting in versatile unique output properties in different RFL schemes. Recent research found the statistical turbulence signatures in the distribution of intensity fluctuations in a continuous wave pumped Erbium based RFL with random Bragg grating scatters [105, 178], which provide a platform to study the challenging turbulent behavior in photonics. Near lasing threshold, the statistical distribution of RFL was characterized by a power law tailed function consistent with a Lévy α-stable distribution as a universal existence of such statistical properties in random lasing systems [101, 104]. The simple architecture of RFL has provided a perfect photonics platform to study the fundamental physics in various random systems. SBS is a major noise source in various RFL systems, especially with Raman gain medium based random laser, which has a higher threshold than the SBS threshold. The stochastic behavior of RFL originated from the SBS process was studied in an RFL based on Raman gain recently [98]. As an interaction between the optical field and the traveled acoustic wave, SBS with a narrow gain bandwidth provides interesting properties for the BRFL, which is quite different from RFLs using Raman gain or

Erbium-doped fiber gain. SBS is a three wave coupling process where the pump, probe, and acoustic wave interact with each other. The phase noise of the pump laser could be transferred to the emitted Stokes wave under the combined influence of cavity feedback and damping of the acoustic wave [179]. To fully understand the lasing mechanism and its statistical characteristics, both the properties of the RFL and the accompanied acoustic wave inside the gain fiber should be studied. A population inversion based dynamic grating was formed and studied in an open cavity Yb-doped fiber laser with distributed feedback [180]. Similarly, the acoustic wave generated by the SBS can modulate the refractive index of the SBS gain medium periodically through electrostriction in the fiber [181], which makes it possess both grating properties and wave properties. The feature of the moving Brillouin dynamic grating (BDG) can be read by a laser that satisfies the phase matching condition [182, 183], where the linewidth of BDG in the conventional SBS process has been measured by sweeping the frequency and recording the reflection intensity of probe light. However, the dynamic properties of the distributed grating, such as its phase noise and intrinsic wave spectral width, were seldom studied. In fact, the reflection of the probe light also carries the phase information on the acoustic wave, and the direct detection of acoustic wave properties in the BRFL is important for researchers to understand the underlying fundamental physics but has not been analyzed so far.

In this chapter, the acoustic wave generated in the BRFL was characterized by continuous probe light in Section 3.2 and by pulsed probe light in Section 3.3 respectively. The acoustic wave was generated by a linearly polarized high power pump laser in the gain medium of BRFL and detected by a second low power probe laser with orthogonal polarization. In Section 3.2, the phase noise and intensity noise properties of the acoustic wave was measured by the continuous probe light. Different linewidths of lasers were utilized as the pump source, where the phase noise and spectral width of the acoustic wave was found to be determined by the spectral convolution of pump light and its Stokes light. In Section 3.3, pulsed probe light was used to realize distributed detection of the acoustic wave by employing OTDR technique. The distributed measurement results provided a new perspective to study the performance and noise properties of BRFL, which enhanced our understanding about the fundamental physics behind RFLs.

3.2 Continuous probe wave detection

3.2.1 Principle of acoustic wave detection in BRFL

In the configuration of BRFL, the pump laser with linear polarization is injected into the slow axis of the 2 km PM fiber, and the backward Stokes light experiences the distributed Rayleigh scattering along 500 m PM fiber, providing feedback for BRFL's radiation. The refractive index of the 2 km PM fiber is modulated periodically by the acoustic wave generated in the BRFL, which can be expressed as:

$$\delta n = \overline{\delta n}\left[1 + v\cos\left(2\pi\upsilon_B t \pm \frac{2\pi}{\Lambda}z + \phi(t)\right)\right] \tag{3.1}$$

where $\overline{\delta n}$ is the average refractive index change, v is the fringe visibility of the index change, Λ is the period of the acoustic wave, $\phi(t)$ are the phase uncertainties of the acoustic wave, and υ_B is the Brillouin frequency shift. The Brillouin frequency shift is determined by frequency difference between the pump wave and the backward Stokes wave, which is given by the following equation:

$$\upsilon_B = \frac{2nV_a}{\lambda} \tag{3.2}$$

where n, V_a and λ are the fiber refractive index, the velocity of the acoustic wave, and the wavelength of the pump laser, respectively. To detect the acoustic wave generated by the BRFL, a probe laser is also injected to the 2 km SBS gain fiber with orthogonal polarization to a pump laser. The dynamic refractive index change induced by the acoustic wave in the fiber periodically modulates the phase of the probe light, leading to a frequency shift with the same value as the frequency of the acoustic wave υ_B. The phase uncertainties $\phi(t)$ of the acoustic wave introduce additional phase noise to the probe light and broaden its linewidth, which could be measured by the heterodyne method. At the same time, the periodically modulated refractive index has uniform structures in the spatial domain, leading to grating properties where light at resonant frequency would experience strong reflection by the refractive index structures. Due to different refractive indices between the slow axis and the fast axis in the PM fiber, the resonant light wavelength for orthogonal polarization is different in the same acoustic wave modulated refractive index structures. This provides us a tool to detect the acoustic wave properties by using a probe light with different frequency from the pump light, where the reflected probe light can be separated from other light by an optical filter and to do further analysis. The relationship of the resonant frequency difference between x and y polarization optical waves has been analyzed in the detection of the conventional BDG [181], which can be expressed as:

$$\Delta\upsilon = -\frac{\Delta n}{\bar{n}}\bar{\upsilon} \tag{3.3}$$

where $\bar{n} = \left(n_x + n_y\right)/2$, $\Delta n = n_x - n_y$, $\bar{\upsilon} = \left(\upsilon_x + \upsilon_y\right)/2$, n_x and n_y are the refractive index of the PM fiber in the slow and fast axis, respectively. υ_x is the optical frequency of the pump laser for BRFL's radiation, and υ_y is the optical frequency of the probe laser for acoustic wave detection. The operation principle is schematically shown in Figure 3-1. When the pump laser (x polarization) with frequency υ_x is launched in the slow axis of the PM SBS gain fiber through circulator 1, SBS is initiated from thermal noise in the Brillouin gain fiber and its Stokes light propagates in the opposite direction that has a frequency downshift with respect to the pump laser. After passing through circulator 2, the backward Stokes light would be reflected by Rayleigh scattering of the feedback fiber and provide the distributed feedback for the BRFL. The acoustic wave generated by the BRFL induces periodic structures in the spatial domain acting as a dynamic grating. Therefore, when the probe laser with orthogonal polarization operating at frequency υ_y is injected into the BRFL's cavity, it would be reflected by the BDG in the Brillouin gain fiber. The reflected probe light experiences a red shift that could be interpreted from two perspectives. One illustration is that the dynamic grating moves away from the incident probe light; thus, the red shifted frequency of the reflected probe light is caused by the Doppler effect. Another illustration is that the periodically modulated refractive index modulates the phase of probe light periodically in the time domain and introduces a frequency shift with the same frequency of modulation. The phase noise of the acoustic wave is passed to the reflected probe light and broadens its linewidth, and the spectra of the reflected probe light are the spectral convolution between the original probe light and the acoustic wave. When the linewidth of probe light is much smaller than the spectral width of the acoustic wave, the spectra of the reflected probe light are similar to the intrinsic spectra of the acoustic wave. From the second perspective, the dynamic grating generation and detection is a FWM process [184, 185] between the pump light, BRFL, probe light, and reflected probe light, which are coupled by a dynamic material density variation in the fiber. The spectral width of the acoustic wave is characterized by the heterodyne method by measuring the beat signal between a local laser oscillator and the reflected probe light, and the intensity dynamics of the acoustic wave could be characterized by measuring the intensity fluctuation of the reflected probe light.

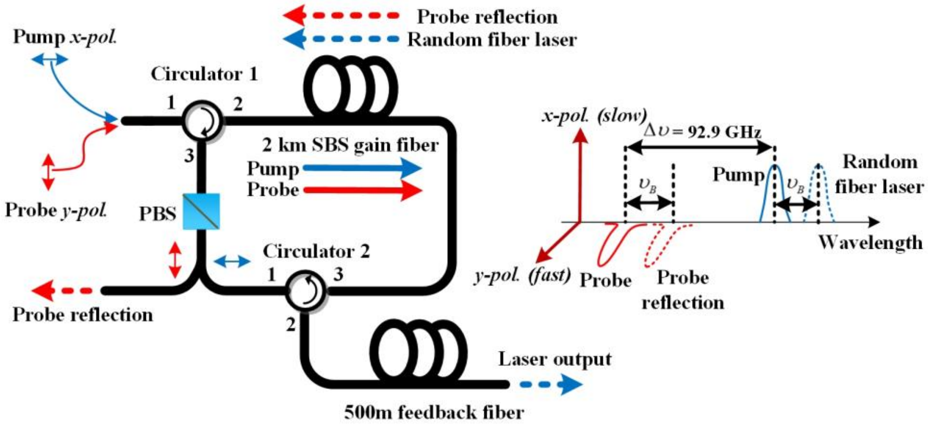

Figure 3-1 Schematic diagram of the operation principle of acoustic wave detection in the BRFL.

3.2.2 Experimental setup and results

Figure 3-2 depicts the experimental setup for the measurement of the acoustic wave. The BRFL was pumped by a laser with 3.5 kHz linewidth or 2 MHz linewidth. After it was amplified by an Erbium-doped fiber amplifier (EDFA), the pump laser was launched into a polarization controller (PC) and polarization beam splitter 1 (PBS 1) to generate a linearly polarized pump laser, which was then injected into the slow axis of a polarization beam combiner (PBC). The output of the PBC was connected with port 1 of circulator 1 to inject the pump laser into the random fiber laser cavity. The Brillouin gain medium was a 2 km Panda-type PM fiber with a fiber loss of 0.296 dB/km and a mode field diameter of 6.48 μm at the wavelength of 1550 nm. The backward Stokes light from the SBS in the Brillouin gain medium passed through port 2 and port 3 of circulator 1 and was then injected to the common port of PBS 2. Note that the polarization state of the pump laser was along the slow axis in the PM fiber cavity and the backward Stokes light would also have the polarization state along the slow axis. Therefore, after the Stokes light passed through the PBS 2, most of its energy went to the slow axis port of PBS 2 and be injected to port 1 of circulator 2. Then, the Stokes light was reflected by the 500 m PM Rayleigh scattering fiber to provide a randomly distributed feedback, which was injected back to the random laser cavity after port 3 of circulator 2. The intensity dynamics of the BRFL was measured by photo-detector 2 (PD 2) after the 500 m Rayleigh scattering fiber (RS fiber) and a filter. A local laser oscillator with the 0.1 kHz linewidth was used to generate the beat electrical signal between the BRFL and the local oscillator. The linewidths of the BRFL were measured by PD 4 and an ESA using the heterodyne method. To detect the acoustic waves generated in the 2 km PM Brillouin gain medium, a linearly polarized probe laser was aligned to the fast axis of PBC. After the PBC, the probe laser was injected into the fast axis of the Brillouin gain medium through circulator 1. At a certain wavelength, the probe laser would be resonant with the BDG and experience strong reflection in the 2 km Brillouin gain medium. After passing through circulator 1, the reflected probe light with the polarization state along the fast axis was injected to the fast axis port of PBS 2. The spectrum of the reflected probe light was measured after PBS 2 and coupler 2 by an optical spectrum analyzer (OSA) with 0.02 nm resolution. To measure the intensity dynamics and linewidth of the reflected probe laser, a tunable bandpass filter with 3 GHz bandwidth was used, which only let the reflected probe light with red shift passing through. After the narrow linewidth filter, the reflected probe light with the red shift was amplified by EDFA 2 and was then split into two arms. One arm was used for the direct detection of the intensity dynamics of the reflected probe light using PD 1 and an oscilloscope, and the other arm was used to generate the beat signal between the reflected probe light and a local laser oscillator with the 0.1 kHz linewidth. The beat signal was measured by PD 3 and ESA. The red line in Figure 3-2 represents a PM fiber or component, while the black line represents a single mode fiber or component.

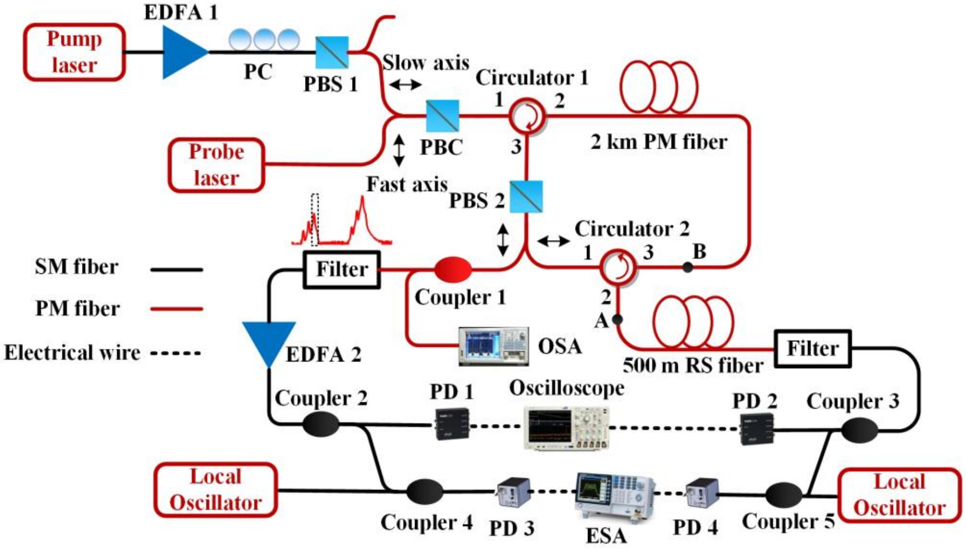

Figure 3-2 Experimental setup for acoustic wave detection in the BRFL. SM fiber: single mode fiber; PM fiber: polarization maintaining fiber.

In order to calculate the resonant wavelength difference between the pump light in the slow axis and the probe light in the fast axis, birefringence of the 2 km Brillouin gain fiber was first characterized by measuring the Brillouin frequency shift along its fast and slow axis before the experiment. The Brillouin frequency shift was characterized by launching the pump laser with the 3.5 kHz linewidth into the slow or fast axis of the PM fiber and measuring the beat signal between the pump laser and backscattered Stokes light generated by SBS. Figure 3-3 shows the measured Brillouin gain spectrum in both axes. It was shown in Figure 3-3 that the Brillouin frequency shifts along fast axis and slow axis were 10.3304 GHz and 10.3354 GHz, respectively. The Brillouin frequency shift difference was 5 MHz, corresponding to $\Delta n \sim 6.94\times10^{-4}$ birefringence of the PM fiber by Equation 3.2. The strong internal birefringence can not only enable a high degree of laser polarization stability against external perturbations during its propagation in one principal axis of the PM fiber but also gives a large wavelength separation between the pump laser and the probe laser in our experiment, which makes it easier to separate the reflected probe light from pump light. According to Equation 3.3, the theoretical frequency separation between pump and probe lasers would be 92.9 GHz, corresponding to the wavelength separation of 0.744 nm.

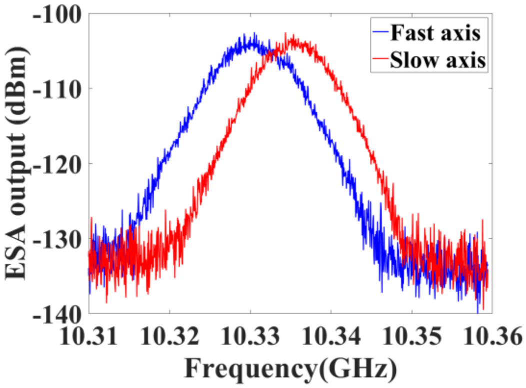

Figure 3-3 Measured Brillouin gain spectrum in the fast axis and slow axis of the 2 km PM Brillouin gain fiber.

For the detection of acoustic waves in the BRFL, the spectrum from the fast axis after PBS 2 and coupler 2 was first measured by the OSA, which was shown in Figure 3-4. The power of the probe laser was relatively small (~0.25 mW) to avoid SBS generation induced by itself. The blue curve in Figure 3-4 (a) was the spectrum of the reflected probe light from the 2 km Brillouin gain fiber when there was no pump laser launched into the BRFL's cavity. It can be seen that when the BRFL was turned off, the probe laser in the fast axis was mainly reflected by Rayleigh scattering in the 2 km Brillouin gain fiber. The two side peaks were caused by spontaneous Brillouin scattering in the fast axis due to the long length of the Brillouin gain fiber. After the pump laser was turned on and the BRFL was above its lasing threshold, most of the reflected probe light would experience a red shift, as shown of the red curve in Fig 3-4 (a). Due to the finite extinction ratio of the polarizing components and relatively high power of the pump laser (~50 mW), the spectrum of the pump laser and the generated BRFL could also be observed on the OSA. The central wavelengths of probe laser and pump laser were 1549.552 nm and 1550.296 nm, respectively, with a wavelength separation of 0.744 nm, which agreed well with the theoretical prediction. In order to characterize the spectral width of the generated acoustic wave, the beat signal between the local laser oscillator with the 0.1 kHz linewidth and the reflected probe light was measured. Note that the linewidth measured here by the heterodyne method was different from the BDG linewidth measured in the previous literature. In the previous literature [181-183], the BDG linewidth was measured by sweeping wavelength of the probe light and then the reflected light intensity was recorded at different wavelengths, which was similar to the spectrum characterization in a regular FBG. However, in our experiment, by injecting a single frequency probe light to the Brillouin gain medium, the linewidth broadening of the reflected probe light was characterized. The phase of the probe light was modulated by the dynamic refractive index change of the fiber, and the acoustic wave would pass its phase noise to the reflected probe light, leading to its linewidth broadening. Therefore, the linewidth measured in our experiment characterizes the phase noise and intrinsic spectral width of the acoustic wave rather than the BDG linewidth or spectrum referred in the previous literature. The beat signals on PD 3 were shown in Figure 3-4 (b) when the linewidths of the pump laser and the probe laser were 3.5 kHz and 0.1 kHz, respectively. The spectra of the acoustic wave stimulated in the BRFL had a single narrow linewidth peak with the 20 dB linewidth of 90 kHz, as shown of the red curve. To compare the difference between random fiber lasers and regular cavity lasers, point A in the experimental setup in Figure 3-2 was disconnected and a 4% Fresnel reflection point was created. Thus, the distributed feedback from Rayleigh scattering was replaced by a single point reflection from the fiber end, and a Brillouin fiber laser with the fixed cavity length was formed. In the conventional cavity Brillouin fiber laser, the acoustic wave possessed multimode structures, as shown of the blue curve in Figure 3-4 (b). This was because the cavity of the BRFL in our experiment had a long cavity length, resulting in a free spectral range that was much smaller than the Brillouin gain bandwidth. Meanwhile, the weak reflection from the fiber end provided a low Q laser cavity, which further increased the phase noise of the Brillouin fiber laser. In a previous experiment [186], a typical Brillouin laser based on a high Q resonator with a large free spectral range showed a low phase noise and a single narrow linewidth spectral peak. However, it required that the frequency difference of a pair of cavity modes precisely matches the Brillouin frequency shift. The pump wavelength must be aligned to one of the resonator's cavity modes to ensure that the energy of the pump light can be injected to the high Q resonator. The threshold of the Brillouin laser changed dramatically with different pump wavelengths and free spectral ranges of the resonator. The frequency of the acoustic wave was detuned from the Brillouin frequency shift when the threshold of the Brillouin laser is high. In contrast, in our experiment, random laser generation does not require the wavelength alignment of pump light. The distributed feedback enabled by coherent Rayleigh scattering forms a "modeless" random distributed cavity, which could be injected by the pump light at any wavelength. The random distributed cavity always selects a narrow lasing spectral peak at the highest gain, leading to the frequency of the acoustic wave being precisely aligned to the Brillouin frequency shift of the Brillouin gain fiber. Meanwhile, the BRFL possesses a narrow linewidth spectral peak and low phase noise, regardless of the long cavity length and relative weak feedback provided by Rayleigh scattering, which results from the distributed feedback provided by coherent Rayleigh scattering. The distributed feedback could eliminate the multimode structures of the acoustic wave, which are similar to the mode structures of BRFL that can be manipulated by different feedback mechanisms [187].

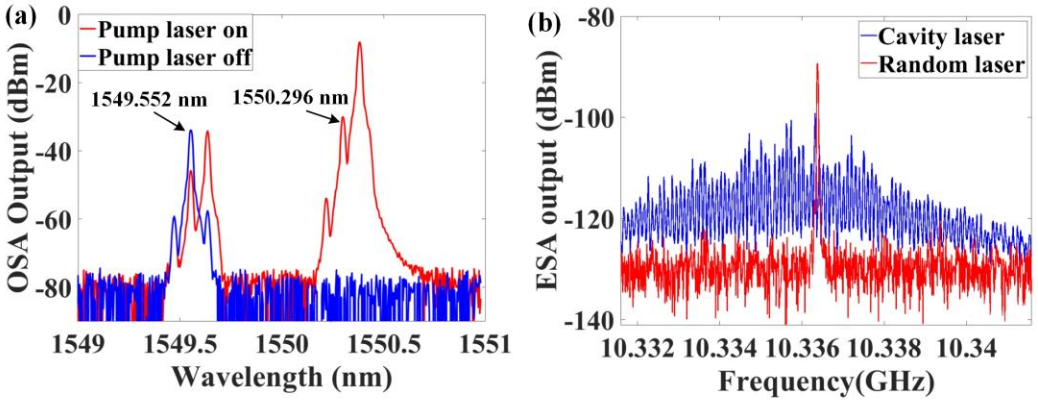

Figure 3-4 (a) Spectrum of the reflected probe light after coupler 2 when the pump laser is turned on (red) and turned off (blue). (b) Beat spectra of the reflected probe light with a local laser oscillator in the regime of BRFL (red) and regular cavity laser (blue) when the linewidths of pump and probe lasers are 3.5 kHz and 0.1 kHz.

In order to study the influence of pump lights and probe lights on the property of the reflected probe light, different linewidths of pump and probe lasers were utilized in the experiment. The linewidth of the local laser oscillator for heterodyne detection was kept at 0.1 kHz to ensure the proper linewidth measurement of the reflected probe light. First, a semiconductor DFB laser with 2 MHz linewidth was used as a probe laser when the linewidth of the pump source for the BRFL was kept at 3.5 kHz. The beat spectral measurement results on PD 3 and ESA were shown as the blue curve in Figure 3-5 (a) with the 20 dB linewidth of 30 MHz–40 MHz, corresponding to the 3 dB linewidth of 1.5 MHz–2 MHz [59]. The reflected probe light had a similar linewidth to the original probe light, indicating that the intrinsic spectral width of the acoustic wave was much smaller than the linewidth of the probe light. Then, the 2 MHz semiconductor DFB laser was used as a pump source, and the linewidth of the probe laser was chosen to be 0.1 kHz. The measured beat spectra were shown as the red curve in Figure 3-5 (a), which was very similar to the blue curve. Due to the dynamic refractive index modulation of the acoustic wave in the Brillouin gain fiber, the probe laser experienced a huge linewidth broadening from 0.1 kHz to 2 MHz after reflection by the dynamic grating. Compared to the acoustic wave spectral width measurement result in Figure 3-4 (b), it can be seen that the intrinsic spectra of the acoustic wave were determined by the spectral convolution of the pump light and its Stokes light. For example, in the regular cavity laser when the linewidth of the pump light was 3.5 kHz, the spectral convolution between the narrow linewidth pump light and the Stokes light showed multimode structures [blue curve in Figure 3-4 (b)], which was similar to the multimode structures of a regular Brillouin fiber laser. In the BRFL, the Stokes light possessed a narrow linewidth spectral peak; thus, the spectral convolution result between the Stokes light and the pump light was mainly determined by the spectra of the pump light. When the linewidth of the pump light for the BRFL was 3.5 kHz, the 20 dB spectral width of the acoustic wave was measured to be 90 kHz, corresponding to the 3 dB linewidth of 4.5 kHz [red curve in Figure 3-4 (b)]. When the linewidth of pump light for the BRFL was 2 MHz, the 3 dB spectral width of the acoustic wave was measured to be 1.5 MHz–2 MHz [red curve in Figure 3-5 (a)]. The spectral width of the acoustic wave was very close to the linewidth of pump light in the BRFL. Note that although the blue curve in Figure 3-5 (a) also showed the broad linewidth, it could not represent the intrinsic spectral width of the acoustic wave in the gain medium as the linewidth of the probe laser was broader than the linewidth of the acoustic wave in this case. The power of probe light was much smaller than the power of pump light so that probe light had little influence on the property of the acoustic wave. The measured beat spectra in Figure 3-5 (a) were the convolution result among the spectra of pump light, BRFL, and probe light. Because the frequency drift range of BRFL was slightly larger when the 2 MHz linewidth laser was used as pump light, the linewidth of the red curve was slightly broader than the linewidth of the blue curve in Figure 3-5 (a). The influence of different linewidths of pump sources and acoustic waves on the property of BRFL was further studied by measuring the linewidth of BRFL using different pump sources. The beat spectra between local laser oscillator and BRFL were measured on PD 4 and ESA. Figure 3-5 (b) shows that the random fiber lasers always possess narrow linewidth spectral peaks no matter whether the linewidths of the pump laser are 3.5 kHz or 2 MHz, which is determined by the coherent feedback provided by the distributed Rayleigh scattering [56]. However, the pump laser with different linewidths introduces different phase noises to the acoustic wave in the fiber, which further affects the linewidth of BRFL. The 20 dB linewidth of BRFL is 24 kHz when the linewidth of the pump laser was 3.5 kHz, while the corresponding 20 dB linewidth is broadened to 51 kHz when the linewidth of the pump laser is 2 MHz. Although the dominating factor that determines the linewidth of BRFL comes from the coherent nature of distributed Rayleigh scattering, the phase noise of the acoustic wave could be another factor to influence the linewidth of BRFL. The linewidth relationship among pump light, probe light, BRFL, and reflected probe light manifests that acoustic wave generation and detection in the experiment is a FWM process, where phase noise is transferred from one light to another that could further affect the intensity dynamics of the reflected probe light.

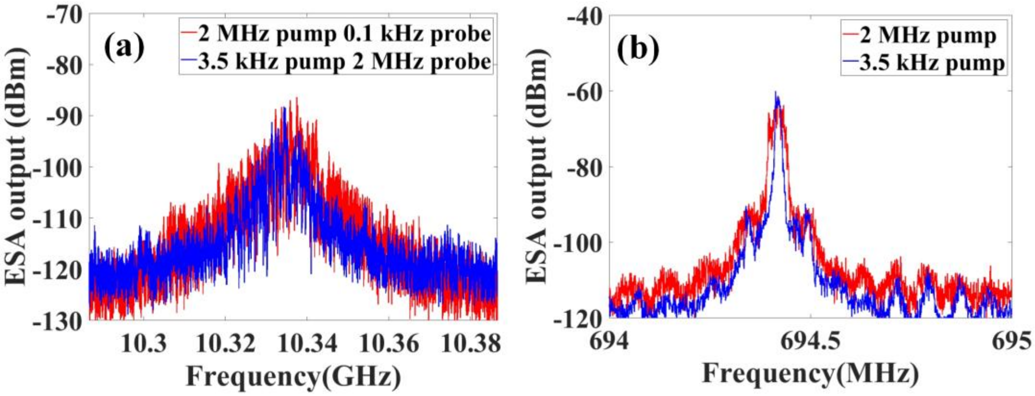

Figure 3-5 (a) Beat spectra of the reflected probe light with a local laser oscillator in the regime of BRFL when the linewidths of pump and probe lasers are 2 MHz and 0.1 kHz, respectively (red), or when the linewidths of pump and probe lasers are 3.5 kHz and 2 MHz, respectively (blue). (b) Beat spectra of BRFL with a local laser oscillator when the linewidth of the pump laser is 2 MHz (red) or 3.5 kHz (blue).

The output intensities of reflected probe light and BRFL were investigated simultaneously in the time domain by using an oscilloscope on different channels, as shown in Figure 3-6. The left column in Figure 3-6 presents the intensity dynamics of probe reflection and BRFL (or SBS noise), collected from the oscilloscope with different linewidths of pump and probe lasers, and the two right figures are histograms of their corresponding intensity statistical distribution. Figure 3-6 (a) corresponds to the case when the linewidths of pump light and probe light were 3.5 kHz and 0.1 kHz, respectively, where the 20 dB spectral width of the acoustic wave was measured to be 90 kHz in Figure 3-4 (b). The output intensity of BRFL (black curve) showed that strong spikes randomly appeared in the time domain due to mode hopping, which was affected by local gain competition at different positions of the Brillouin gain medium with different Brillouin shift frequencies. At the same time, the intensity of the reflected probe light showed a strong correlation with BRFL's output intensity as similar spikes appear simultaneously in the intensity dynamics of the reflected probe light, indicating that the probe light could be modulated by the dynamic grating, which carried similar intensity dynamic properties to BRFL. However, when the pump laser or probe laser was substituted by the semiconductor DFB laser with the 2 MHz linewidth, the intensity modulation of probe light by the dynamic grating showed different characteristics. Figure 3-6 (b) corresponds to the case when the linewidths of pump light and probe light were 3.5 kHz and 2 MHz, respectively, and Figure 3-6 (c) corresponds to the case when the linewidths of pump light and probe light were 2 MHz and 0.1 kHz, respectively. Although in those two cases, the intensity spikes of reflected probe light and BRFL appeared at the same time, the intensity spikes of the reflected probe light missed some information without the downward beat pattern part, as shown of the red curve in Figure 3-6 (b) and (c). Because pump light, BRFL, probe light, and reflected probe light are coupled by the same dynamic material density variation in the fiber, a phase matching condition plays an important role in determining the coupling process. When a relatively broadband light, such as the DFB laser in our experiment, interacts with other light in the FWM process, only a small portion of frequency component is aligned to the frequency that satisfies the phase matching condition, which makes it a weak coupling process. When the phase matching condition is not satisfied, a large amount of thermal noise is introduced in the wave coupling process, and the intensity dynamics of four lasers are not following each other. The noise properties of the conventional SBS process were measured by disconnecting point B in the experimental setup in Figure 3-2. The intensity of the backscattered SBS was plotted as the black curve in Figure 3-6 (d), and the red curve was the intensity of the reflected probe light in this process. The intensity statistics of SBS initiated from thermal noise showed an exponential law of probability distribution, indicating a Gaussian stochastic process that has been analyzed in the previous literature [54]. Although a narrow linewidth (0.1 kHz) laser was used to detect the acoustic wave in this process, the intensity of the reflected probe light also showed the stochastic process with the exponential law of probability distribution. Because the acoustic wave in SBS initiated from thermal noise has large phase fluctuations and ~10 MHz linewidth, the phase of probe light is modulated by the thermal noise and a large phase noise is introduced to the reflected probe light. The coherent superposition of phase noise leads to the stochastic intensity noise property of the reflected probe light. In the FWM process, the stochastic noise property is transferred to the reflected probe light with a large phase noise, which can be proven by analyzing the intensity statistics of BRFL and the corresponding reflected probe light with different pump and probe lasers, as shown in the right part of Figure 3-6. For the BRFL, narrow linewidth peaks are formed by the coherent feedback of Rayleigh scattering in the random distributed cavity; thus, the intensity probability distribution of BRFL always shows Gaussian statistics, regardless of the linewidth of the pump laser. However, when the linewidth of the pump laser or probe laser is broadened to ~2 MHz, the reflected probe light exhibits a stochastic process with an exponential law of intensity probability distribution, as shown in Figure 3-6 (b) and (c). In contrast, when both the pump laser and the probe laser have a narrow linewidth, the reflected probe light also has a narrow linewidth in Figure 3-4 (b) with Gaussian intensity statistics in Figure 3-6 (a). The noise features measured from intensity dynamics confirm with the phase noise of the reflected probe light from linewidth measurement, which further proves the FWM process and explains intensity dynamic relations between BRFL and reflected probe light in different pump and probe conditions.

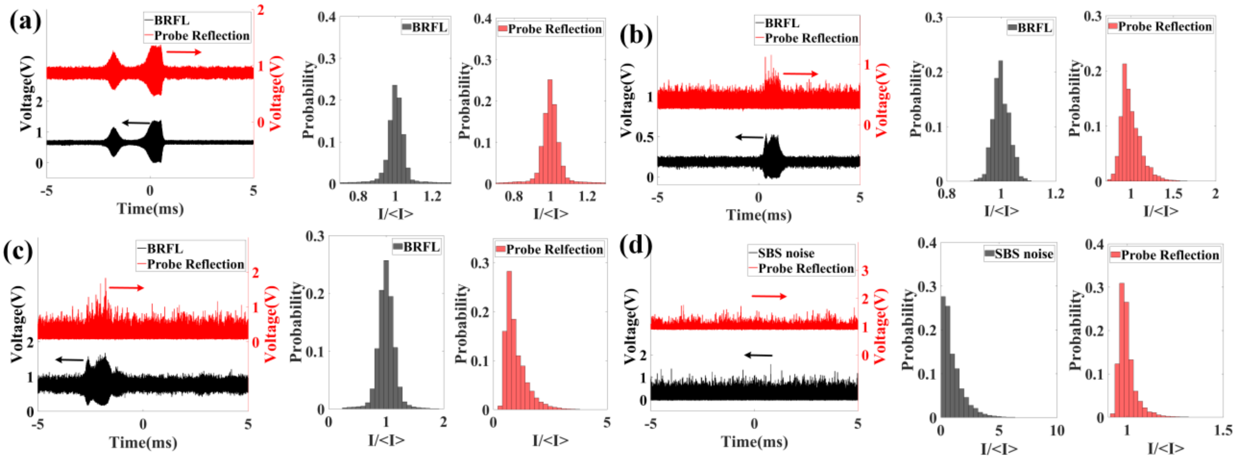

Figure 3-6 (a) Intensity dynamics (left) and its statistics probability distribution (right) of BRFL (black) and reflected probe light (red) when the linewidth of the pump laser for the BRFL is 3.5 kHz and the linewidth of the probe laser is 0.1 kHz. (b) Intensity dynamics (left) and its statistics probability distribution (right) of BRFL (black) and reflected probe light (red) when the linewidth of the pump laser for the BRFL is 3.5 kHz and the linewidth of the probe laser is 2 MHz. (c) Intensity dynamics (left) and its statistics probability distribution (right) of BRFL (black) and reflected probe light (red) when the linewidth of the pump laser for the BRFL is 2 MHz and the linewidth of the probe laser is 0.1 kHz. (d) Intensity dynamics (left) and its statistics probability distribution (right) of SBS noise (black) and reflected probe light (red) when the linewidth of the pump laser for SBS is 3.5 kHz and the linewidth of the probe laser is 0.1 kHz.

3.3 Distributed detection of the acoustic wave

In Section 3.2, the intrinsic spectral width and intensity dynamics of the acoustic wave in a polarized BRFL were characterized experimentally. However, the distributed spatial information of the acoustic wave still remains unclear because a single frequency continuous probe wave was used in the previous characterization. By either linearly sweeping the probe light frequency in OFDR [188, 189] or using the pulsed probe light in OTDR [190, 191], the distributed spatial information can be obtained, which provides a visual picture of acoustic wave evolution in the spatial domain for us to further understand noise properties of the acoustic wave. The requirement of the frequency sweeping in the OFDR technique usually takes a long time, thus hindering its dynamic applications (up to kHz) in the distributed sensing. By sending a series of probe pulses and measuring the time resolved traces in the oscilloscope, OTDR is a good technique for the distributed static and dynamic detection of the acoustic wave in BRFLs.

In this section, the acoustic wave in a Brillouin gain fiber generated by BRFL was measured by the OTDR technique for the first time. A dynamic grating was introduced by the acoustic wave, where its detection was an SBS enhanced polarization decoupled FWM process. Based on the measurement time of one detection process, the distributed detection could be divided into static measurement and dynamic measurement. The static measurement characterized the time averaged property of the acoustic wave, in which the frequency of probe light was swept in several minutes. In dynamic measurement, a series of pulsed probe light with 10 kHz repetition rate at fixed optical frequency under phase matching condition was launched into the Brillouin gain fiber, thus the fast change of the acoustic wave intensity was obtained.

3.3.1 Principle of distributed acoustic wave detection

BRFL makes use of SBS as the gain mechanism, where the pump wave and Stokes wave beat together, giving rise to density variation associated with an acoustic wave through the electrostriction effect. The acoustic wave introduces a moving periodically modulated refractive index acting like a moving FBG which reflects light in its resonance frequency. In the PM fiber, the property of the moving grating could be detected by monitoring the reflected wave from a probe wave with orthogonal polarization when the phase matching condition is satisfied. The detection of the moving dynamic grating is a polarization decoupled FWM process among the pump wave, Stokes wave, probe wave and reflected probe wave. The detailed derivation of the four coupled wave can be seen in [185]. The probe light can be launched into the Brillouin gain fiber either from the initial end or the tail end. In both cases, the pump wave propagates along $+z$ direction and Stokes wave propagates along $-z$ direction with the same polarization state along the slow axis, so that the acoustic wave induced by SBS is propagating along the $+z$ direction, as shown in Figure 3-7 . When the probe light is launched from the initial end of the Brillouin gain fiber [Figure 3-7 (a)], the probe wave in y polarization has the same propagation direction as the acoustic wave, thus a reflected wave, whose frequency is downshifted from the frequency of probe wave by an amount of one Brillouin frequency, experiences a photon energy down conversion process, as shown in Figure 3-7 (a). On the other hand, if the probe light is launched from the tail end of the Brillouin gain fiber, the probe wave in y polarization has opposite propagation direction from the acoustic wave, and the reflected wave experiences a photon energy up conversion process whose frequency is upshifted from the frequency of the probe wave, as shown in Figure 3-7 (b). The SBS induced birefringence change of the Brillouin gain fiber in the polarization decoupled FWM process can be expressed as [185]:

$$\Delta B_{SBS} = \frac{4\pi n_x \Delta \upsilon_{SBS}}{\omega_s} \tag{3.4}$$

where n_x is the refractive index in the slow axis, ω_s is the optical frequency of Stokes light, $\Delta\upsilon_{SBS} = (\upsilon_p - \upsilon_{pr})_{with\ SBS} - (\upsilon_p - \upsilon_{pr})_{without\ SBS}$ is the change of frequency difference between the pump wave and probe wave induced by the SBS process. Therefore, the SBS induced birefringence change can be obtained by measuring the value of $\Delta\upsilon_{SBS}$ in the experiment.

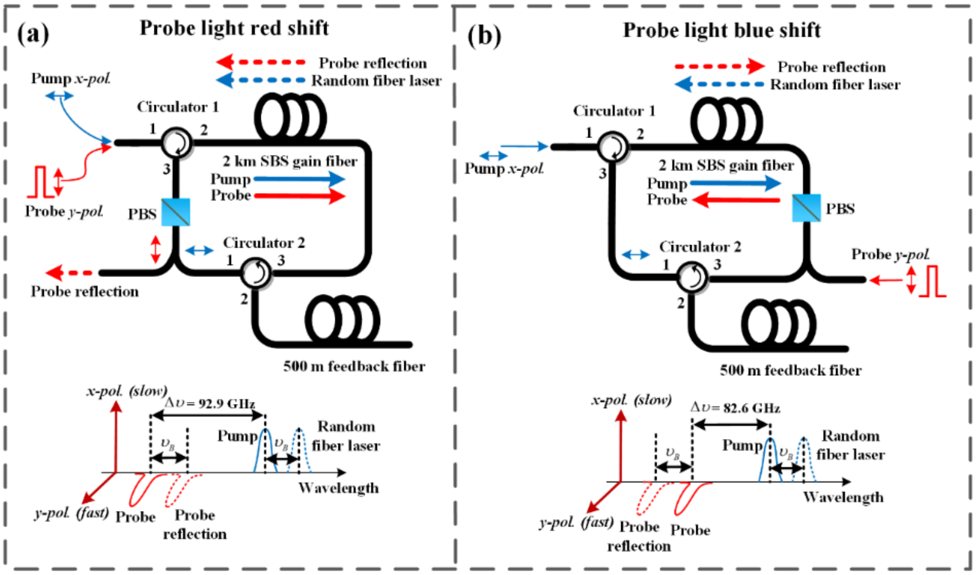

Figure 3-7 Configuration of the BRFL and the operation principle of acoustic wave detection when (a) probe light co-propagates with the acoustic wave and (b) probe light counter propagates with the acoustic wave.

3.3.2 Experimental setups

The experimental setups were mainly comprised of three parts: the pump and probe light generation part (part A), the BRFL configuration part (part B) and the reflected light detection part (part C). Figure 3-8 (a) shows the acoustic wave detection setup when the probe light propagated in the same direction with the pump light and acoustic wave. Both the pump light and probe light were generated from a single frequency laser with 0.1 kHz linewidth in order to make sure that the frequency difference between the pump light and probe light can be precisely controlled. When the probe light propagated in the same direction with the pump light, photons of the probe light experienced energy down conversion process. In this process, the frequency of the probe light in fast axis should be ~92.9 GHz away from the pump light in slow axis to make the frequency of the probe light being aligned to the central reflection bandwidth of the dynamic grating. The ~92.9 GHz frequency separation was determined by the birefringence of the Brillouin gain fiber in the setup [192].

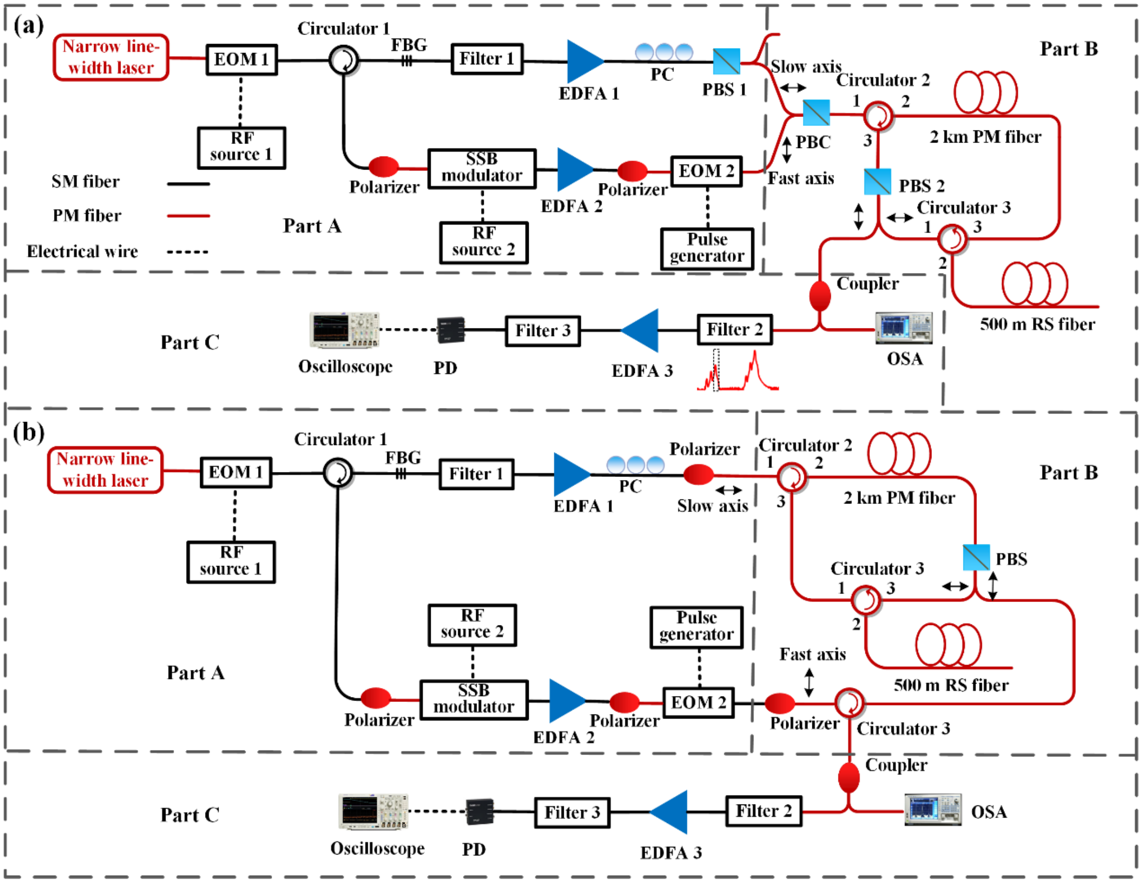

Figure 3-8 Experimental setup for acoustic wave detection in BRFL; (a) probe light co-propagates with the acoustic wave and (b) probe light counter propagates with the acoustic wave.

The large frequency separation between the pump light and the probe light were obtained by using a 40 GHz bandwidth electric-optic modulator (EOM 1) combined with a 20 GHz single side band (SSB) modulator. First, two light side bands with 80 GHz separation were generated after the narrow linewidth laser was modulated by EOM 1. Then, the two side bands were injected to a circulator and a 3 GHz bandwidth FBG, after which one of the side band was reflected back by the FBG and the other side band passed through a 3 GHz bandwidth optical filter to reject light with other optical frequencies. The light after filter 1 was the pump source for BRFL, which was then amplified by the EDFA 1. After EDFA 1, a PC combined with PBS 1 were used to align polarization of the pump light to the slow axis of the PM fiber. Before being modulated by the SSB modulator, the light from EOM 1 was reflected back by the 3 GHz bandwidth FBG and then passed through circulator 1. A polarizer before the SSB modulator was used to ensure the single polarization state of the light. The frequency of light was shifted 12.9 GHz away by the SSB modulator, after which it was amplified by EDFA 2 and then modulated by EOM 2 to generate 10 ns pulses with a 10 kHz repetition rate. The polarizer before EOM 2 was employed to optimize the pulse extinction ratio, which was important to reject noise during the distributed acoustic wave detection process. The pulse after EOM 2 had a single polarization state and was aligned to the fast axis of the PM fiber, which was the probe light in the setup. The pump and probe light were combined together by a PBC and then injected to the Brillouin gain fiber of BRFL through circulator 2. SBS was initiated by the pump light in the Brillouin gain fiber. In the slow axis, the backward Stokes light passed through PBS 2 and the 500 m PM Rayleigh scattering (RS) fiber. The backscattered light from the 500 m RS fiber was then injected back to the Brillouin gain fiber to provide distributed feedback for BRFL. In the fast axis, the probe light was reflected by the co-propagating dynamic grating and experienced an optical frequency red shift. The frequency red shifted probe light then passed through circulator 1 and PBS 2. After PBS 2, the light was split by a coupler, after which one of the paths was directly connected to an OSA to measure its spectrum property, and the other path passed through filter 2 with 3 GHz bandwidth to select the frequency red shifted probe light, which was then amplified by EDFA 3 and detected by a PD and an oscilloscope. Filter 3 after EDFA 3 was used to reject the spontaneous emission from EDFA 3 in order to further reject noise. For the probe light photon energy up conversion process, the probe light propagated in the opposite direction with the acoustic wave and pump light. The experimental setup for the probe light photon energy up conversion process in Figure 3-8 (b) was similar to the photon energy down conversion process in Figure 3-8 (a) except that the probe light was injected to the other end of the 2 km long Brillouin gain fiber in Figure 3-8 (b). The frequency separation between pump light and probe light was decreased to 82.5 GHz in the probe light photon energy up conversion process, which was the subtraction of 92.9 GHz and 10.4 GHz (Brillouin frequency shift of the 2 km long PM fiber).

3.3.3 Static measurement results

After the pulsed probe light was launched into the Brillouin gain fiber, it was reflected by the dynamic grating which was induced by the refractive index modulation of the acoustic wave. The reflected light was detected by the PD and the oscilloscope, where the time resolved traces on the oscilloscope showed the reflected light intensity distribution in the spatial domain. By sweeping the optical frequency difference between pump light and probe light, the distributed reflection spectra of the dynamic grating could be obtained. Figure 3-9 (a) shows the 3 dimensional reflected light intensity in the spatial domain at different optical frequency separation between pump light and probe light. The fitting dynamic grating spectra width is around 100 MHz, which results from the convolution of the probe pulse spectra and the intrinsic dynamic grating spectra, thus a longer probe pulse can give a narrower spectrum and a better frequency and birefringence accuracy at the expense of sacrificing the spatial resolution. The reflectivity of the dynamic grating is determined by the refractive index modulation depth (intensity of the acoustic wave) of the fiber, which is proportional to the Brillouin gain of the BRFL. This provides a direct distributed gain profile measurement method of BRFL in the spatial domain. The averaged reflectivity of the dynamic grating can be obtained by integrating the dynamic grating spectra in the frequency domain of Figure 3-9 (a).

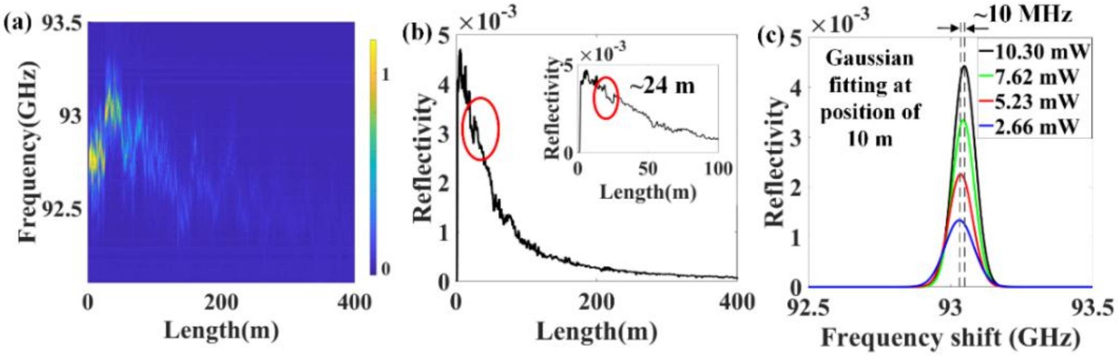

Figure 3-9 (a) Distributed reflection spectra of the dynamic grating induced by the acoustic wave in BRFL for the probe light photon energy down conversion process; (b) Reflectivity of the dynamic grating in the spatial domain along the Brillouin gain fiber; (c) Gaussian fitting of the reflection spectra of the dynamic grating at the position of 10 m at maximum gain when the output powers of BRFL are 10.3 mW, 7.62 mW, 5.23 mW and 2.66 mW respectively.

As shown in Figure 3-9 (b), the reflectivity of the dynamic grating decreases exponentially in the spatial domain, indicating that the gain of the BRFL decreases exponentially in the spatial domain due to the pump depletion. After the position of 400 m, almost all of the pump light is converted to its Stokes light and the Brillouin gain nearly drops to zero. At some particular position, such as the position around 24 m, the Brillouin gain is slightly deviated from the exponential curve due to the relatively large birefringence fluctuation at those positions, as can be seen in Figure 3-9 (a). This is because the linewidth of BRFL is on the order of sub kHz, which is much narrower than the Brillouin gain bandwidth. Any tiny birefringence fluctuation of the Brillouin gain fiber can lead to the frequency change of the

BRFL. The BRFL have optimized gain at the position where the central frequency of the Brillouin gain spectrum is aligned to the operation optical frequency of BRFL, while at other positions the Brillouin gain is decreased due to the misalignment of the local Brillouin gain spectra with the operation optical frequency of BRFL. The misalignment of the local Brillouin gain spectra and the operation optical frequency of BRFL are one of the noise sources for the mode hopping and laser intensity fluctuation. At a fixed position, the spectra of the dynamic grating show slightly central frequency variation at different operational powers of BRFL due to the SBS induced birefringence change of the fiber. For example, Figure 3-9 (c) shows that, at position of 10 m, the maximum central frequency change of the dynamic grating spectra is on the order of 10 MHz, corresponding to $\sim 10^{-7}$ birefringence change of the PM fiber according to Equation 3.4.

There is a problem using the probe light photon energy down conversion process to detect the acoustic wave in BRFL. Since the refractive index modulation depth of the dynamic grating at the beginning of the Brillouin gain fiber is much stronger than the latter part, it is hard to know whether the power of probe light is depleted or not at the beginning of the Brillouin gain fiber. To verify this point, the probe light was launched to the Brillouin gain fiber from the opposite direction to the propagating direction of pump light. In this detection mechanism, the reflected probe light experienced an optical frequency blue shift instead of red shift because of the counter propagating direction between acoustic wave and probe light. Figure 3-10 (a) shows the spectra measured on OSA when the optical frequency of the probe light is aligned or misaligned to the resonance frequency of the dynamic grating respectively. When the optical frequency of the probe light is aligned to the resonance frequency of the dynamic grating, the blue shifted reflected light can be detected by the OSA. Otherwise, there is no reflection of the probe light.

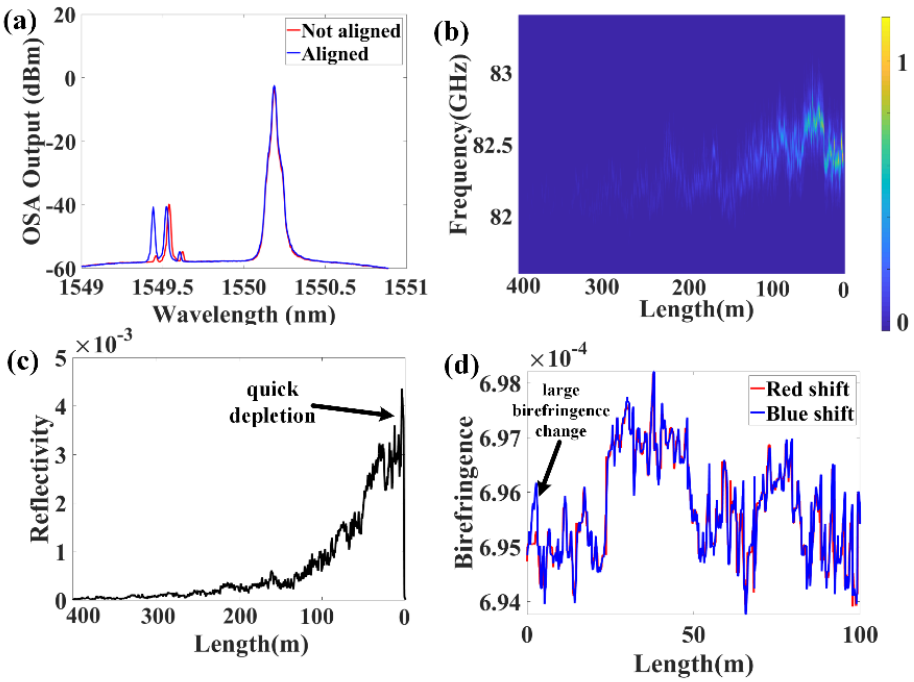

Figure 3-10 (a) Spectrum of the reflected probe light measured on OSA for the probe light photon energy up conversion process; (b) Distributed reflection spectra of the dynamic grating induced by the acoustic wave in BRFL; (c) Reflectivity of the dynamic grating in the spatial domain along the Brillouin gain fiber; (d) Birefringence of the Brillouin gain fiber measured by the optical frequency red shifted probe light and optical frequency blue shifted probe light.

The 3 dimensional distributed dynamic grating spectra in the spatial domain is plotted in Figure 3-10 (b). Because the quick depletion of pump light in the Brillouin gain fiber, the reflection of the probe light can only be detected at the first 400 m part after the pump light is launched to the Brillouin gain fiber. Therefore, only the 400 m part with the highest Brillouin gain is plotted in Figure 3-10 (b). Similar to Figure 3-9 (a), the central frequencies of the dynamic grating spectra, which is determined by the birefringence of the PM fiber, characterize the distributed birefringence of the Brillouin gain fiber. Because the probe light is injected from the other end of the Brillouin gain fiber, the distributed birefringence measurement result in Figure 3-10 (b) is the inverse of the distributed birefringence value in Figure 3-9 (a) in the spatial domain. The reflectivity of the dynamic grating, which is proportional to the local Brillouin gain, is also obtained by integrating the dynamic grating spectra in the frequency domain of Figure 3-10 (b). Figure 3-10 (c) shows that the overall trend of the distributed Brillouin gain exhibits an exponential increase in the spatial domain, which confirms the exponential decrease of the Brillouin gain measured by the probe light photon energy down conversion process. The result manifests that the probe light in the photon energy down conversion process is not depleted because of the weak reflectivity of the dynamic grating. The weak reflectance of the dynamic grating is caused by the non-uniform birefringence of the Brillouin gain fiber, leading to that the central reflection spectrum of the dynamic grating written by the acoustic wave is not perfectly aligned to the optical frequency of the probe light at most positions of the Brillouin gain fiber. For the probe light photon energy up conversion process, the pump light is depleted more quickly than the probe light photon energy down conversion process at the initial part of the Brillouin gain fiber. This is because in the photons energy up conversion process, the photons of probe light absorb energy from the acoustic phonons and pump light photons, which makes them depleted more quickly in the spatial domain. The quick depletion of pump light makes the gain of BRFL focus at the initial part of the Brillouin gain fiber, leading to a large birefringence change at the highest gain part of the Brillouin gain fiber. Figure 3-10 (d) compares the distributed birefringence of the Brillouin gain fiber measured by red shifted probe light and blue shifted probe light respectively. It can be seen that at the initial part of the Brillion gain fiber, the birefringence detected by the blue shifted probe light deviates approximately 10^{-6} from the birefringence detected by the red shifted probe light. At the rest of the positions, the birefringence measured by the two mechanisms agrees with each other well. This confirms the quick Brillouin gain depletion at the initial part of the Brillouin gain fiber in Figure 3-10 (c), proving that the focusing of the high gain leads to large birefringence change of the Brillouin gain fiber.

3.3.4 Dynamic measurement results

The dynamic gain profile measurement was implemented by sending a series of probe pulses at a repetition rate of 10 kHz to measure the distributed intensity of the acoustic wave in BRFL. These results are also plotted in 3 dimensional figures where the *x* axis represent the position and *y* axis represent the time, as shown in Figure 3-11 (a) and Figure 3-11 (b). The distributed dynamic gain profile of BRFL provides information on dynamic process of mode hopping and mode competition in BRFL. The interference fringes of BRFL in the Brillouin gain fiber in the spatial domain and in the time domain can be observed simultaneously. At a fixed position, the intensity of the acoustic wave fluctuates periodically in the time domain which is caused by mode hopping. Because the BRFL is easily disturbed by the environmental perturbation [193], the Brillouin gain profile and the feedback provided by the Rayleigh scattering is not ultra-stable. The operating mode of BRFL switches from one frequency to other frequencies from time to time due to the random mode competition in BRFL, which is the origin of mode hopping in BRFL. By measuring the distributed dynamic gain profile, the interference fringes of the Stokes light in the spatial domain are also obtained at a fixed time. The fringe patterns measured by the pulsed probe light for the photon energy up conversion process and the photon energy down conversion process exhibit different characteristics in the spatial domain. For the photon energy up conversion process in Figure 3-11 (b), the pulsed probe light propagates in the same direction and velocity with the beat pattern. For example, if the peak of the beat signal is detected by the probe light at time T_1, the pulsed probe light would propagate together with the same peak along the Brillouin gain fiber at time T_2 and time T_3, as shown in Figure 3-11 (d). The OTDR technique uses the time resolved trace to discriminate the backscattered light at different positions in a fiber. This explains why the dark spot (or bright spot) of the interference fringes in Figure 3-11 (b) always appears at all of the positions along the Brillouin gain fiber at a fixed time. This phenomenon proves that the mode hopping beat pattern co-propagates with the Stokes light in the Brillouin gain fiber during the random mode switching process. In contrast, when the probe light counter propagates with the Stokes light, a single pulse can detect all of the peaks of the beat pattern that are transmitted on the Brillouin gain fiber. For example, if a peak of the beat signal is detected by the probe light at time T_1, the following two peaks can also be detected by the probe light in sequence at time T_2 and T_3, as shown in Figure 3-11 (a) and Figure 3-11 (c). This provides us with a method to study how the fringes evolve dynamically in the spatial domain. In Figure 3-11 (a), the dynamic distributed acoustic wave measurement shows that the fringes always first appear at the initial position of the Brillouin gain fiber. The initial position means the fiber end where the pump light is first launched to the Brillouin gain fiber. The interference fringes are the envelope of the beat signal between different random modes of BRFL. If there is only one dominant lasing mode, no interference fringe can be detected. When the gain of the light inside the random cavity is greater than the loss at other frequencies, other random modes start to compete with the original dominant random modes in the Brillion gain fiber with limited Brillouin gain. As the initial part of the Brillouin gain fiber has the highest gain, it is also the place where the condition that the gain is greater than the loss can be first satisfied. The dark spot of the fringes measured by the pulsed probe light moves along the Brillouin gain fiber. However, the slope of these dark lines in Figure 3-11 (a) does not represent the real moving velocity of the beat pattern. As shown in Figure 3-11 (c), the time difference between two consecutive pulses is $\Delta T = T_1^{'} - T_1$. During this time interval, the displacement of the light is $(T_1^{'} - T_1)c/n$ and N periods of the beat pattern have passed the same position on the Brillouin gain fiber. N is the integer of $\frac{(T_1^{'} - T_1)c/n}{\lambda}$ and the slope of the dark lines in Figure 3-11 (c) can be expressed as $k = c/n - N\lambda/\Delta T$, where the λ is the wavelength of the envelope. With the fixed pulse repetition rate, the slope of the dark lines is determined by the envelope wavelength of the beat pattern. Therefore, the constant linear slope of these dark lines represents that no phase noise is detected on the beat pattern. Longer duration time of the linear dark lines represents smaller detected linewidth of the BRFL. The minimum detected 20 dB linewidth of BRFL in the experiment is 4.3 kHz, which is measured by Fourier transform of the output intensity of BRFL when the beat pattern occurs, as shown in the inset curve in Figure 3-11 (a). The phase noise of the beat pattern leads to nonlinear slope changes of the dark lines in Figure 3-11 (a) which is further caused by the frequency change of BRFL and nonlinear group index change induced by the acoustic wave. Due to the Kramers-Kronig relation, changes in the gain or loss of a medium are always accompanied by changes in the refractive index. Although the magnitude of the refractive index changes is relatively small, it varies rapidly with the frequency of Stokes light near the Brillouin gain peak [167]. Because the velocity of the beat pattern is the group velocity of the envelope which is related to $\frac{\Delta\omega}{\Delta k}$, rapid changes of the refractive index changes can change the group index considerably and affect the group velocity of the beat pattern. The distributed interference fringes measured by detecting the dynamic grating through pulsed probe light provide us a new method to study the phase noise of BRFL, which could help us to better understand the random nature of BRFL and to further improve its performance in practical applications.

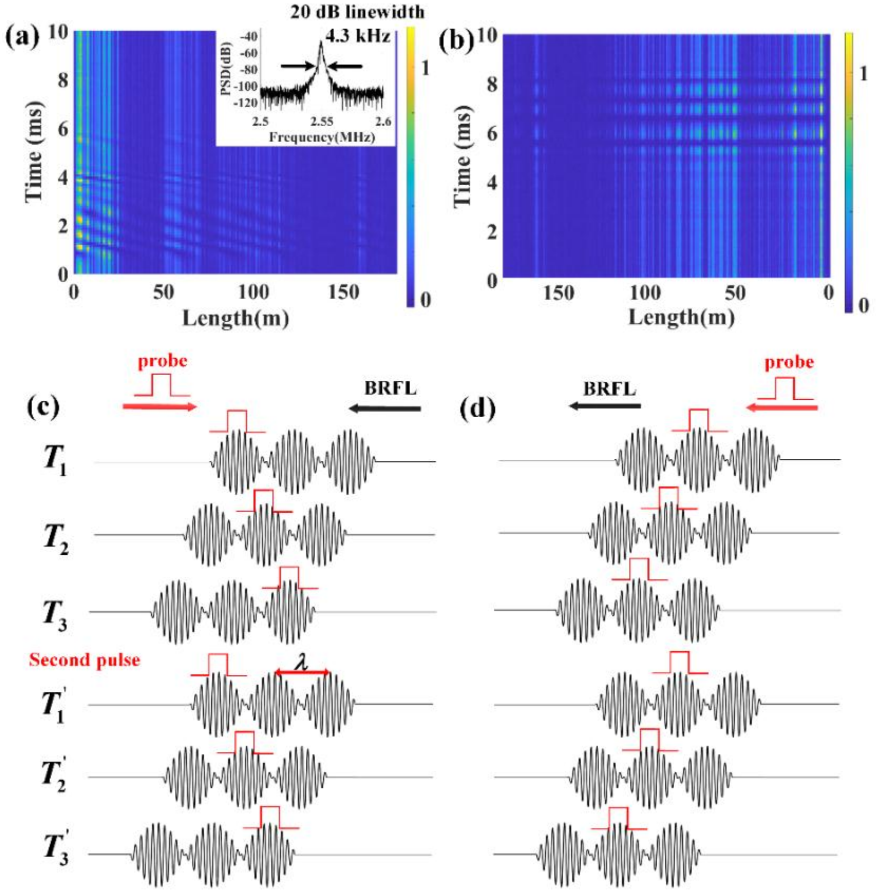

Figure 3-11 (a) The spatial-time map of the acoustic wave intensity when the probe light experiences the photon energy down conversion process. The inset figure is the spectra measurement of two beating modes when mode hopping occurs in BRFL; (b) The spatial-time map of the acoustic wave intensity when the probe light experiences the photon energy up conversion process; (c) Schematic diagram of the acoustic wave detection process when the probe light experiences the photon energy down conversion process; (d) Schematic diagram of the acoustic wave detection process when the probe light experiences the photon energy up conversion process.

The peak amplitude of the acoustic wave intensity fluctuation in one second is counted for the two detection mechanisms. Figure 3-12 (a) and Figure 3-12 (b) show its statistical distribution histograms at a high gain position and a low gain position respectively, when the BRFL is near the lasing threshold. The high gain position part refers to the position of the first 10 m of the Brillouin gain fiber and the low gain position refers to the position of 310 m to 320 m of the Brillouin gain fiber. Near the lasing threshold, the L-shaped long-tailed histograms characteristic of extreme value behavior are observed at both the high gain position and low gain position. The *x* axis in Figure 3-12 is normalized by the corresponding significant wave height (SWH), which is defined as the mean height of the highest third of the acoustic wave intensity [194]. When the event of the peak amplitude is more than twice the SWH, it can be considered as a rogue (extreme) event. Therefore, the generation of the optical rogue wave (RW) is detected in BRFL near the lasing threshold. Moreover, at the high gain position in Figure 3-12 (a), the highest recorded peak intensity reaches about 6 times that of the corresponding SWH, and the occurrence proportion of RW events is about 14%. At the low gain position in Figure 3-12 (b), the highest peak intensity is only about 4 times that of the corresponding SWH, and the generation probability of the RW decreases to 5.6%. The underlying physics for the RW generation is that the SBS process is initiated from the thermal noises in the fiber. The temporal output is a mixture of amplified noisy Stokes light and lasing Stokes light, depending on whether or not the stochastic lasing occurs [111]. The amplification of the thermal noise in BRFL is similar to the modulation instability seeded from noise that results in a series of high-contrast peaks of random intensity [195]. The higher proportion of the RW events at high gain position than low gain position indicates that the random intensity initiated from thermal noise is amplified nonlinearly on the Brillouin gain fiber. The SBS dynamics can be described by the amplitude coupled equations among the pump wave, the Stokes wave and the acoustic wave, where higher peak density variation of the acoustic wave leads to higher wave coupling between the pump wave and the Stokes wave. The nonlinear transfer function of the SBS process modifies the temporal intensity probability distribution of the mixing noisy Stokes light and the lasing

Stokes light, leading to a higher proportion of the RW events at the high gain position of the Brillouin gain fiber.

When the BRFL is far above the lasing threshold, the temporal statistical distribution histograms at high gain position and low gain position show a Gaussian distribution because of the stable establishment of the BRFL emission above the lasing threshold. Because the high coherent BRFL and acoustic phonons are established, the thermal noise is rejected and the optical RW cannot be detected anymore as there are no events of the peak amplitude more than twice the SWH, as shown in Figure 3-12 (c) and Figure 3-12 (d). However, the temporal intensity at high gain position exhibits more events with high peak intensity fluctuation than that of temporal intensity at low gain position when the BRFL is above the lasing threshold, which is mainly attributed to the following two reasons. First, the nonlinear transfer function of SBS process combined with the inhomogeneous gain in the spatial domain amplifies intensity fluctuation nonlinearly. Therefore, a small signal fluctuation at the position with low gain could lead to tremendous peak intensity fluctuation at the position with high gain. At the same time, intensity fluctuations are continuously introduced into the laser dynamics during the laser amplification process along the Brillouin gain fiber. The peak fluctuations at the high gain position are accumulated from multiple intensity fluctuations on the Brillouin gain fiber, which is the origin of the relative high peak fluctuation. Second, the non-uniform birefringence [as shown in Figure 3-10 (d)] of the Brillouin gain fiber corresponds to non-uniform gain spectra in the spatial domain, creating various localized gain areas since the optical frequency linewidth of BRFL is ultra-narrow. Because the localized gain area at the high gain position obtains high energy due to the mode competition with limited total Brillouin gain, it is also the place where the mode competition is fiercest, thus inducing a relative high peak intensity fluctuation when mode competition happens.

Figure 3-12 (a)-(d) are the results when the probe light co-propagates with the acoustic wave and experiences an optical frequency red shift, while Figure 3-12 (e)-(h) are the results when the probe light counter propagates with the acoustic wave and experiences an optical frequency blue shift. The blue shifted probe light measurement results agree with the red shifted probe light measurement results, which confirms the optical RW detection result of BRFL.

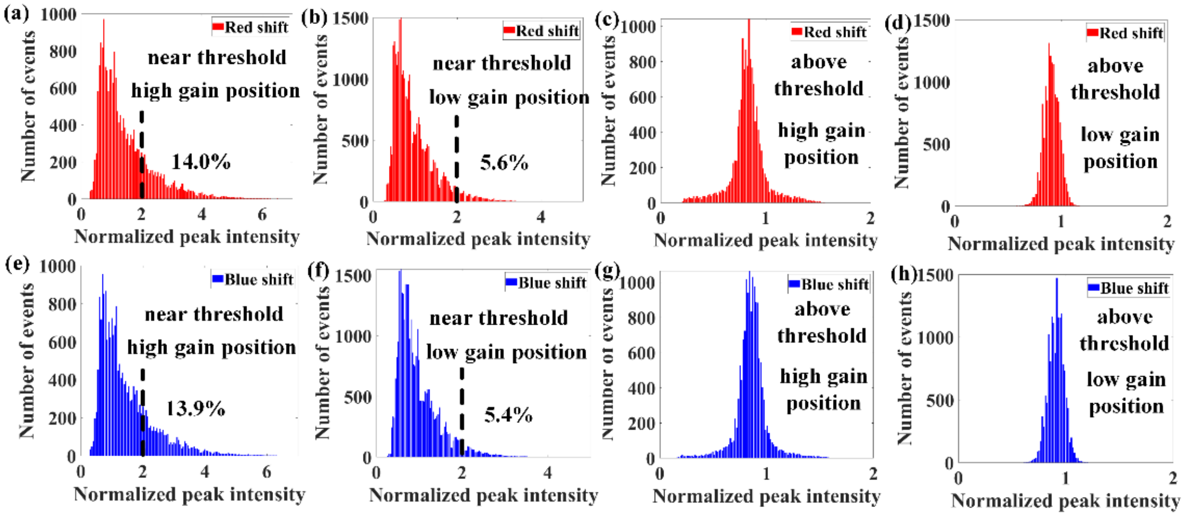

Figure 3-12 Histograms of the temporal intensity statistical distribution near the lasing threshold at (a) high gain position and (b) low gain position for red shifted probe light measurement; Histograms of the temporal intensity statistical distribution above the lasing threshold at (c) high gain position and (d) low gain position for red shifted probe light measurement; Histograms of the temporal intensity statistical distribution near the lasing threshold at (e) high gain position and (f) low gain position for blue shifted probe light measurement; Histograms of the temporal intensity statistical distribution above the lasing threshold at (c) high gain position and (d) low gain position for blue shifted probe light measurement.

3.4 Conclusion

In this chapter, the property of the acoustic wave generated in BRFL's gain medium is characterized by measuring the reflected light property of a second probe laser. First, by using a continuous probe light, the phase noise of the acoustic wave is determined by spectral convolution between the pump light and its Stokes light, which further modulates the phase of the reflected probe light and broadens its linewidth. The distributed feedback provided by coherent Rayleigh scattering determines the narrow linewidth spectral peaks of BRFL, which is also affected by the phase noise of the acoustic wave in the fiber gain medium. The relationship between the linewidth of the reflected probe light and the pump light (or probe light) proves that the acoustic wave generation and detection is a FWM process among the pump light, the probe light, BRFL, and the reflected probe light. When narrow linewidth pump and probe laser interact in the FWM process, the intensity dynamics of the reflected probe light have the same characteristics as the intensity dynamics of BRFL, and both of them have the Gaussian statistics distribution. However, when the semiconductor DFB laser with relative broadband spectra is used as a pump laser or probe laser, the intensity dynamics of the reflected probe light cannot follow the intensity dynamics of BRFL, which is caused by the introduced stochastic noise with the exponential intensity statistics distribution.

Then, the distributed detection of the acoustic wave generated by BRFL is realized based on the OTDR technique for the first time. Photons of probe light can either give energy to the acoustic phonons or absorb energy from the acoustic phonons, depending on the relative propagation direction of the acoustic wave and the probe light. In the static measurement, the distributed dynamic grating spectra are obtained by sweeping the frequency of probe light. The Brillouin gain depletes exponentially along the Brillouin gain fiber in BRFL. When the photons of probe light absorb energy from the acoustic wave, a quick depletion of the Brillouin gain is observed in the experiment. The SBS induced birefringence variations are estimated to be approximately 10^{-7} to 10^{-6} by measuring the central frequency change of the dynamic grating spectra. In the dynamic measurements, the intensity noise of the laser is found to first occur at the highest gain position of the Brillouin gain fiber. The phase noise of

BRFL leads to wavelength variation of the beat pattern, which further leads to nonlinear dark spot changes in the spatial-time acoustic wave intensity map. The spatial-time acoustic wave intensity map provides a new method to characterize the phase noise of BRFL and to study its dynamic evolution process. Optical RWs are found near the lasing threshold of BRFL, where the nonlinear transfer function of the SBS process modifies the temporal intensity probability distribution of the mixing noisy Stokes light and lasing Stokes light. Above the lasing threshold, the temporal intensity at high gain position exhibits more events with high peak intensity fluctuation than that of temporal intensity at low gain position, which is caused by the SBS nonlinear transfer function and the localized gain in BRFL. The detection results enhance our understanding of BRFL, paving the way for its performance improvement in future applications in the field of communication, high precision metrology, sensing and spectroscopy.

Chapter 4 BRFL based on artificial random scattering

4.1 Introduction

An RFL uses “disordered media” to provide distributed feedback. Compared to conventional fiber lasers, RFLs do not have a fixed optical resonator to form the longitudinal mode with equal phase separated by 2π in the cavity. Instead, multiple distributed cavities lead to many longitudinal modes with small frequency differences to compete the finite amount of the laser gain, which brings new laser physics features. There are two typical types of random medium in constructing the RFLs: one is the Rayleigh scattering fiber with the naturally inhomogeneous refractive index variation [86, 196], and the other is the artificially controlled random medium such as the nanoparticles scattering in colloidal suspension inserted in the microstructure fibers, or RFG that has intentionally induced refractive index modulation [61, 197]. Compared to the Rayleigh scattering from fiber’s intrinsic inhomogeneity, artificially introduced random scattering typically owns stronger random refractive index variations, which provide both stronger reflection as the distributed feedback for RFLs and localized FP period interferometers at varied periods to reject laser noise, leading to a lower lasing threshold, narrower linewidth and lower laser frequency noise [110]. The artificially introduced random scattering can be either FBG arrays or RFG inscribed by a femtosecond laser as described in [198]. In this chapter, both of FBG arrays and RFG were employed to provide random distributed feedback for BRFL. By using FBG arrays with different lengths, the longitudinal mode characteristics of BRFL were studied in Section 4.1. In Section 4.2, replica symmetry breaking (RSB) was demonstrated in the RFG based BRFL which indicated a photonic spin-glass state, providing a photonic platform to study the glassy behavior of RFLs.

4.2 Longitudinal mode characteristics of BRFL

Since the first observation of the random fiber lasing phenomenon, the RFL has attracted great research interest in revealing its lasing mechanisms, such as power, temporal and spectral properties [44, 199]. The power features such as the lasing threshold, slope efficiency, and power distribution in the RFL were described with the power balance model [79]. The spectrum broadening and narrowing effect of the RFL was further studied by the modified power balance model [53]. To describe the temporal and statistical properties of an RFL, the nonlinear Schrödinger equation based model was applied by taking account of gain, loss, dispersion, and nonlinear effects [95]. Wave kinetic theory was also developed to study the spectral and power properties of the RFL [119]. However, none of these models considered the mode characteristics in the random fiber laser cavity, which are particularly important in a BRFL with a ~100 MHz narrow gain bandwidth. A previous study showed that narrow linewidth spikes can be observed in the BRFL in single mode fiber feedback [56], and a subsequent detailed work revealed that BRFLs possess unique modeless characteristics with a narrow linewidth around 1 kHz in polarization maintaining fiber feedback [59]. At the same time, BRFLs also suffer from mode hopping effects, which could cause great intensity noise for random laser radiation. In order to design a low RIN laser, understanding of the mode structures is required, especially the longitudinal mode selection mechanism, as well as control of the distributed random feedback technique. Such a topic is important and unfortunately has not been studied and reported so far. Therefore, in this section, the mechanism of the distributed random feedback in BRFL was investigated by replacing the Rayleigh scattering fiber by FBG arrays with varied length.

4.2.1 Experimental setup

The experimental setup is illustrated in Figure 4-1. The pump laser for the BRFL was a fiber laser with 3.5 kHz linewidth (Rock Module, NP Photonics). After amplification by an EDFA, the pump laser was launched into a PC and then split into two arms. One arm acted as the reference to generate the beat signal with the BRFL, and the light in another arm was injected into the ring cavity of the BRFL through circulator 1. The Brillouin gain medium was a 1 km high nonlinear fiber with a large nonlinear parameter ($\gamma \geq 10\ W^{-1}km^{-1}$). Due to the high nonlinearity of the Brillouin gain medium, SBS occurred with the backward Stokes light traveling anticlockwise in the cavity. The Stokes light was reflected by the distributed random structures after passing through port 2 of circulator 2 and then returned to the ring cavity to provide the feedback for the BRFL. In order to compare the longitudinal mode characteristic of the BRFL with different kinds of feedback structures, a 500 m RS fiber in part A and a single FBG in part B were also used to replace the weak FBG array (part C) with various lengths in the setup. The pump laser was tuned to ensure that the wavelength of the Stokes light was aligned to the central wavelength of the weak FBG array. After the laser passed through the feedback part and the isolator (ISO), it was divided into two parts: one part was for direct temporal detection using PD 1 with a bandwidth of 350 MHz; the other part was combined with the reference light from the pump laser to generate the beat signal for heterodyne detection and measured by PD 2 with a bandwidth of 20 GHz. The temporal traces and the fast Fourier transformation (FFT) of the beat signal was measured by the oscilloscope and ESA, respectively.

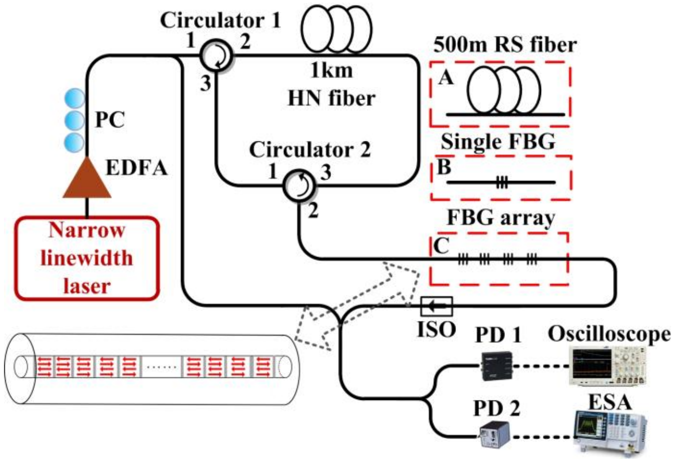

Figure 4-1 Schematic diagram of the experimental setup to characterize the mode property of BRFL. HN: high nonlinear.

4.2.2 Theoretical prediction

To predict the longitudinal mode property of the BRFL supported by the quasi-distributed weak FBG array or single FBG, a theoretical analysis based on the light interference and multi-reflection in the weak FBG array was first performed. Each of the weak FBGs can be regarded as a frozen scattering center, whose position is uniformly distributed along the fiber with a small standard deviation due to fabrication error. As shown in Figure 4-1, when the laser passes through these scattering centers, numerous Fabry–Perot cavities are formed as the light ray bounces back and forth with random phase. Light at some particular frequency that satisfies the boundary conditions of these cavities generates constructive interference and passes through the weak FBG array, while light at another frequency bounces back. The backscattered light is the coherent superposition of the reflected light from all these frozen scattering centers. It can be written as

$$\begin{aligned} E_s(f) &= \sum_{j=1}^{N} R_j E_0 \exp(-i\frac{4\pi n f z_j}{c}) \\ &+ \sum_{j=2}^{N} R_j^2 R_{j-1} E_0 \exp(-i\frac{4\pi n f z_j}{c}) \exp(-i\frac{4\pi n f (z_j - z_{j-1})}{c}) + \ldots\ldots \end{aligned} \tag{4.1}$$

where E_0 is the amplitude of the incident light, N is the total number of scattering centers, n is the refractive index of the fiber, f is the optical frequency, z_j is the position of j_{th} scattering center, c is the light velocity in vacuum, and R_j is scattering coefficient of j_{th} scattering center. The first term in Equation 4.1 describes the direct summation of all the backscattered light from each of the scattering centers, while the second term considers one round trip of the laser between two neighboring scattering centers. Because each of the scattering centers has a small scattering coefficient, only the first two terms of Equation 4.1 are considered in the simulation as the rest of the terms would have little effect on the result. After the light takes a round trip in the laser cavity, the backscattered light in Equation 4.1 would experience a $\frac{2\pi n f L_0}{c}$ phase change, so the total reflected intensity of the optical field can be written as [57]:

$$I_r(f) = \left| E_s(f) + E_s(f)\exp(-i\frac{2\pi n f L_0}{c}) \right|^2 \tag{4.2}$$

where L_0 is the length of the SBS gain fiber. The Brillouin gain has a Lorentz spectrum line shape with the form:

$$g_B(f) = \frac{g_p(\Gamma_B/2)^2}{(f - f_B)^2 + (\Gamma_B/2)^2} \tag{4.3}$$

where g_p is the peak value of the Brillouin gain at $f = f_B$, and Γ_B is the phonon lifetime. The mode characteristics of the BRFL are determined by the multiplication of the Brillouin gain and reflected laser intensity. The simulation results are shown in Figure 4-2.

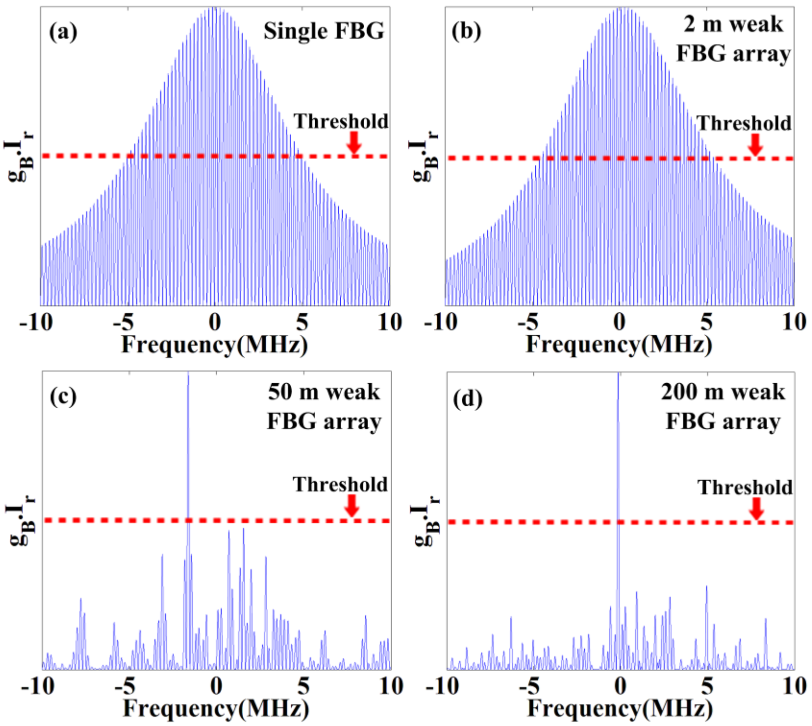

Figure 4-2 Simulation of the mode characteristic of the BRFL with (a) single FBG, (b) 2 m weak FBG array, (c) 50 m weak FBG array, and (d) 200 m weak FBG array as the feedback.

It can be seen in Figure 4-2 (a) that when the single FBG is used to provide feedback for the BRFL, multimode effects occur with a Lorentz spectrum line shape. The mode separation of the BRFL is 200 kHz, corresponding to the free spectral range (FSR) of the ring cavity with 1 km SBS gain fiber. When the feedback is provided by the 2 m FBG array instead of the single FBG, the multimode effects with 200 kHz longitudinal mode separation can still be observed, as shown in Figure 4-2 (b). Then, a 50 m weak FBG array is simulated as the feedback of the BRFL, which has only one dominant longitudinal mode, and the other longitudinal modes are largely suppressed, as shown in Figure 4-2 (c). The reason for the longitudinal mode suppressing is that the long weak FBG array generates more FP resonators with a high quality factor compared with the 2 m FBG array. A large number of FP resonators and the multi-reflection of the laser can trap light inside the cavity, thus enhancing the effective propagation length of the BRFL. Therefore, numerous high fitness FP cavities in the 50 m weak FBG array are formed, which also act as the mode filter with a narrow bandwidth to select only one longitudinal mode for the BRFL. The simulation result in Figure 4-2 (d) also proves the longitudinal mode filter function of the FBG array with single-mode operation. At the same time, the side peaks of the BRFL with 200m FBG array are further suppressed with a higher side-mode suppression ratio (SMSR).

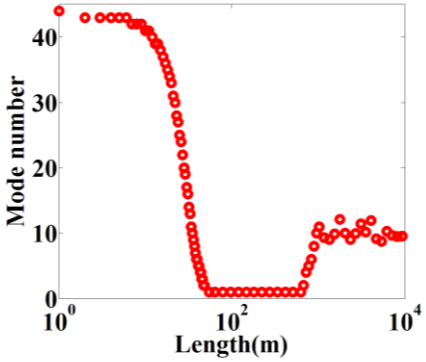

Figure 4-3 Simulation of the mode number of BRFL with different feedback length.

The mode number of the BRFL above the lasing threshold is also calculated at different lengths of the weak FBG array, as shown in Figure 4-3. It can be seen that the performance of the mode filter is determined by the length of the weak FBG array. When the length of the weak FBG array is less than 50 m, the mode number of the BRFL drops dramatically as the length of the weak FBG array increases gradually. This is because the long length of the FBG array gives rise to high-fitness FP cavities; thus, the bandwidth of the mode filter is reduced, and fewer modes can pass through the mode filter. Therefore, the BRFL exhibits single-mode operation when the weak FBG array is longer than 50 m. However, if the FBG array is overlong, then numerous scattering centers in the weak FBG array form a large number of FP resonators, leading to a high density of mode numbers within the 20 MHz Brillouin gain bandwidth [110]. Due to the high density of supported mode numbers inside the cavity, the mode filter exhibits multiple transmission peaks within the Brillouin gain bandwidth and leads to multimode operation for the BRFL. As shown in Figure 4-3, multimode effects start to appear again when the length of the weak FBG array is longer than 1 km. The optimum length of the weak FBG array ranges from 50 m to 1 km to ensure single-mode operation of the BRFL with 1 km SBS gain fiber.

4.2.3 Experimental results

In order to identify the mode characteristics of the BRFL with different kinds of feedback structures, the heterodyne technique was used in the experiment [200]. The pump laser with single frequency radiation served as the local oscillator to mix with the output of the BRFL under test. In the experiment, the FSR of the 1 km ring cavity was 200 kHz, which was sufficiently narrower than the linewidth of the pump laser (3.5 kHz). The convolution can effectively reproduce the spectrum in the radio-frequency spectral domain; thus, the mode characteristic of the BRFL can be identified by doing the FFT of the optical beat signal detected by PD 2. Figure 4-4 shows the mode distribution of the BRFL using a single FBG, 2 m weak FBG array, 50 m weak FBG array, 200 m weak FBG array, 5 km weak FBG array, and 500 m RS fiber as the feedback, respectively. It can be seen in Figure 4-4 (a) and (b) that the temporal traces and mode characteristics of the BRFL are similar between the single FBG feedback case and 2 m weak FBG array feedback case. Both have a large number of longitudinal modes with Lorentz spectrum line shape above the lasing threshold, which agrees well with our simulation results. The inset red curve is the temporal trace of the BRFL detected by PD 1, which exhibits the self-pulsing effects caused by the large number of longitudinal modes. The repetition rate of the generated pulses is also 200 kHz, indicating the spontaneous mode locking of the BRFL as being related to periodic pump depletion in the Brillouin medium [201, 202]. In order to verify the mode filter function of the FBG array, the 50 m FBG array is used to provide feedback for the BRFL. It can be seen in Figure 4-4 (c) that there is only one dominant peak with two small side peaks on the spectrum of the BRFL for the 50 m FBG feedback case. The output intensity of the BRFL in the time domain with the 50 m FBG array is quite stable, as shown in the inset red curve in Figure 4-4 (c). When the 50 m weak FBG array is replaced by the 200 m weak FBG array, the multimode effect of the BRFL is further suppressed with improved SMSR, which is increased from 35 dB for the 50 m weak FBG array case to 55 dB for the 200 m weak FBG array case [Figure 4-4 (d)]. However, the temporal trace exhibits slowly varying fluctuation in the time domain, even though single-mode operation is realized by using the 200 m weak FBG array, which is caused by environmental perturbation on the long-length feedback fiber. Both the 50 m weak FBG array and 200 m weak FBG array are long enough to mimic the random distributed feedback of the RS in the BRFL, as the single longitudinal mode operation can be realized with them. The BRFL using the 500 m RS fiber as feedback also exhibits single longitudinal mode operation [Figure 4-4 (e)]. The physical reason of the so called “modeless spectrum” of a random laser relies on the reflected spectrum modification of the distributed feedback medium. At the same time, the inset temporal trace in Figure 4-4 (e) shows a large output intensity fluctuation in the time domain, resulting from environmental perturbation [18] and high cavity loss when the RS fiber is used. Therefore, the long-length quasi-distributed weak FBG array can not only support the single longitudinal mode operation like the distributed RS fiber, but also reduce the output intensity fluctuation and intensity noise of the BRFL. However, there is an optimum feedback length range, considering the single longitudinal mode operation of the BRFL. When an ultra-long feedback medium such as the 5 km weak FBG array is used as the feedback medium, multimode effects start to occur again, as shown in Figure 4-4 (f). This is attributed to the significant increase in the number of longitudinal modes supported by the 5 km weak FBG array, which also confirms our theoretical analysis in Figure 4-3. As a result, the mode hopping and mode competitions are intensified, leading to unstable oscillations on the temporal trace [Figure 4-4 (f)].

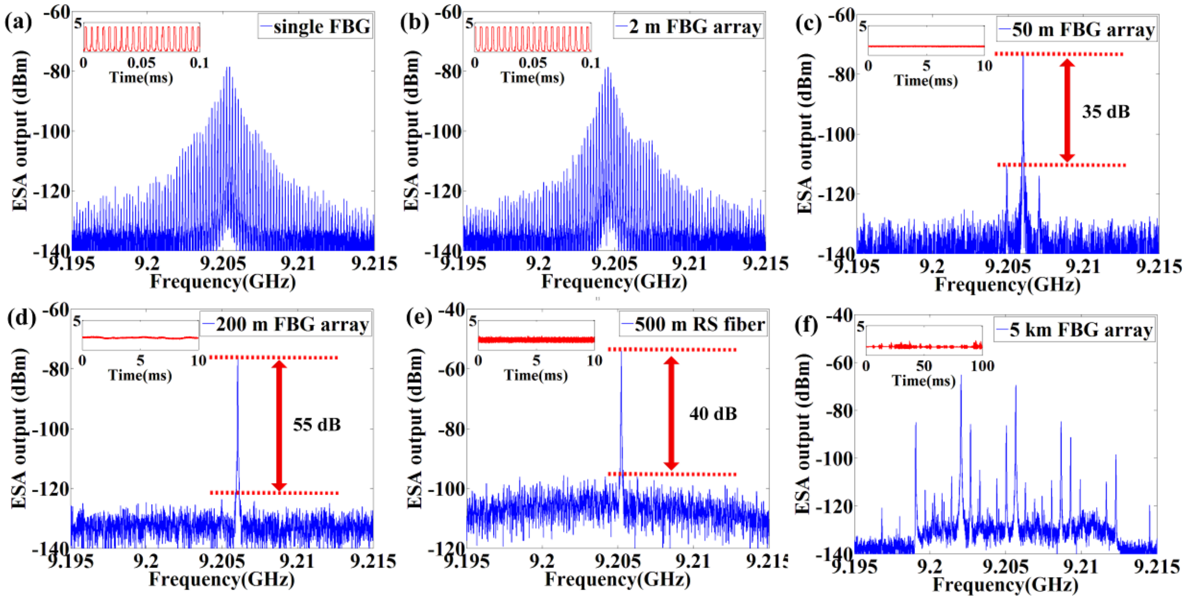

Figure 4-4 Experimental results of the mode characteristics and temporal traces (inset red curve) of the BRFL with (a) single FBG, (b) 2 m weak FBG array, (c) 50 m weak FBG array, (d) 200 m weak FBG array, (e) 500 m RS fiber, and (f) 5 km FBG array as the feedback.

4.3 RSB enabled by RFG

Light localization in the random medium provides a good platform to study the intensity statistics of RFLs. The intensity noise and multimode structures of a Raman RFL enabled by a long RFG as a random coherent feedback mechanism was studied for the applications in chaotic communication and random number generation [41]. RSB was recently found in a RFG based Erbium-doped RFL [103], which demonstrated the transition from a photonic paramagnetic to a photonic spin-glass state. However, the RSB is only demonstrated in RFLs based on Erbium-doped formed stimulated emission of molecules in microscopic states, it is vital to examine if RSB holds for the superposition of local wavelength scale structural changes under macroscopic states in RFLs based on Brillouin gain. Besides, since the physical origin behind the new phenomenon of RSB was not analyzed, it is important to characterize the distributed scattering strength of the RFG in order to better understand the underlying physics behind the one dimensional RFG, which provides versatile new laser dynamics and phenomena. OCT [203-205] can form images of the random scattering medium with micrometers resolution using incoherent light, which is a good method to characterize the local optical property without the interference from other scattering sources. The spectral response of the RFG could also be retrieved by taking Fourier transform of the measured interference pattern.

In this section, an RFG with random phase shifts was first characterized based on the time domain OCT technique. By using a light source with 40 nm bandwidth, the spatial resolution of the OCT setup was around 60 μm. The average reflectivity of the RFG remained constant, while local frozen scattering centers were found in the detailed structure of the reflectivity in the spatial domain. Then, a BRFL based on RFG as random distributed feedback was built to illustrate the difference between RFG based BRFL and Rayleigh scattering based BRFL. Compared to the Rayleigh scattering based BRFL, the BRFL enabled by RFG showed a reduced lasing threshold and high lasing efficiency. Parisi overlap parameter was calculated based on the output intensity fluctuation spectra of the BRFL, revealing a photonic spin-glass phase of the BRFL enabled by the RFG for the symmetry breaking property.

4.3.1 RFG characterization by OCT

The experimental setup consisted of a Michelson interferometer with a low coherence broad bandwidth light source, which was an amplified spontaneous emission noise source with 40 nm bandwidth at wavelength of 1530 nm to 1570 nm, as shown in Figure 4-5. Light was split into two arms through the 3 dB coupler and then recombined from reference and sample arms respectively. The reference arm was composed of a Faraday mirror and a variable delay line. The variable delay line had a resolution of less than 1 fs, corresponding to a 0.2 μm spatial resolution in the fiber. The PC before the RFG in the sample arm was used to optimize the polarization state of the light to get a signal with the highest signal to noise ratio. The combination of reflected light from the sample arm and the reference arm gave rise to an interference pattern, but only if the travelling distance difference of light from the two arms was less than the coherence length of the light source. Due to the broad bandwidth of the light source, the coherence length was shortened to 60 μm. By scanning the delay time of the delay line, a reflectivity profile of the sample was obtained.

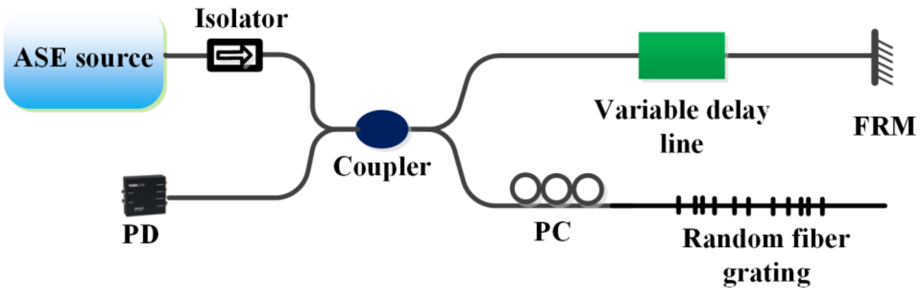

Figure 4-5 RFG characterization setup based on time domain OCT method.

The intensity detected by the photodetector (PD) is proportional to the real part of the inverse Fourier transform of the product of the source spectrum and the complex reflection spectra of the RFG [204]:

$$I(\delta) \propto 1/4\pi \operatorname{Re}\left\{\int_{-\infty}^{+\infty} S(\sigma)\tilde{r}(\sigma)\exp(j2\pi\sigma\delta)d\sigma\right\} \tag{4.4}$$

where Re means the real part, $\sigma = 1/\lambda$ is the wave number, $\tilde{r}(\sigma) = r(\sigma)\exp(j\phi(\sigma))$ is the complex reflection spectra of the RFG, $S(\sigma)$ is the power spectral density of the source, and $\delta = 2(L_2 - L_1)$ is the optical path difference between the reference arm and the sample arm.

Therefore, the complex field reflection spectra of the RFG can be given by the Fourier transform of the intensity detected on the PD:

$$\tilde{r}(\sigma) = F(I(\delta)) / S(\sigma) \tag{4.5}$$

The intensity detected on the PD at different delay times of the delay line is shown in Figure 4-6 (a). It is seen that the total length of the RFG is approximately 50 mm starting from the delayed length of 10 mm to 60 mm. The amplitude of the beat pattern remains almost constant at all positions, indicating a constant average reflectivity of the RFG in the spatial domain. Figure 4-6 (b) is the detailed reflectivity at a local position of the RFG, which shows that localized frozen scattering centers are created due to the random grating period fluctuation of the RFG. Those localized frozen scattering centers can provide distributed feedback for generations of RFLs, creating random modes in the multi-scattering cavity with increased mean free path of photons. The reflectivity of the RFG calculated from Fourier transform in the OFDR method in [206] showed noise tails after the grating part, which was caused by multiple resonant light scattering in the RFG. By comparison, the reflectivity of the RFG measured by OCT shows a clean noise floor after the grating part without disturbance from other noise interference pattern. The incoherent light used in the OCT method ensures the discrete frozen scattering centers characterization while those frozen scatterings are blurred in the OFDR measurement results due to the disturbance of the multiple resonant light scattering sources. The reflection spectra of the RFG can be calculated according to Equation 4.5 in the OCT method. The calculated reflectivity of the RFG (~-30 dB reflection) is calibrated by measuring the actual reflectivity of RFG using an OSA. The RFG has a broad bandwidth reflection spectrum with a flat envelope in the spectral domain from 1530 nm to 1570 nm, as shown in Figure 4-6 (c). This is because the grating period variations of RFG that are characterized in the setup randomly ranges from 0 to 2.5 μm [198], which is larger than the optical wavelength of around 1.5 μm, thus lead to totally uncorrelated phase superposition of light from random scattering centers. The detailed reflection spectra of the RFG in Figure 4-6 (d) around 1550 nm shows that numerous narrow linewidth peaks are formed, which can act as narrow linewidth filters in the application of RFLs. The minimum spectral peak width measured by OFDR in [206] is around 16 pm while ~10 pm spectral width is found in Figure 4-6 (d). The enhanced spectral resolution is enabled by the broad bandwidth light source combined with the high spatial resolution of the tunable optical fiber delay line.

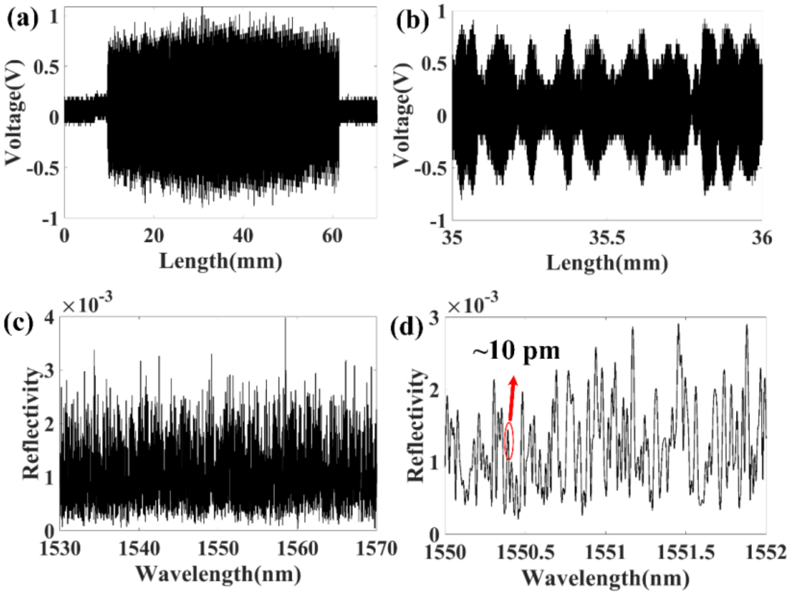

Figure 4-6 (a) Interference pattern detected on PD at different delay length of the delay line; (b) Detailed structure of interference pattern from position 35 mm to 36 mm; (c) Reflection spectra of the RFG calculated from the Fourier transform of the interference pattern; (d) Detailed reflection spectra of the RFG from 1550 nm to 1552 nm.

4.3.2 Demonstration of RSB

The experimental setup of RFG based BRFL is shown in Figure 4-7. The pump light source was based on a 3.5 kHz linewidth fiber laser which was amplified by an EDFA. After the EDFA, a PC combined with a PBS was used to generate a linearly polarized pump light. Then, the pump laser was injected to the random fiber laser cavity through circulator 1. The Brillouin gain medium was a 2 km Panda-type PM fiber with fiber loss of 0.296 dB/km and a mode field diameter of 6.48 μm at a wavelength of 1550 nm. The pump light in the Brillouin gain medium could stimulate backward Stokes light which travelled anticlockwise between circulator 1 and circulator 2. The utilization of the linear polarization of pump light and PM fiber as Brillouin gain medium can greatly reduce the lasing threshold of the BRFL. After port 2 of circulator 2, the backscattered Stokes light from SBS was reflected by the RFG, which enabled random distributed reflection of the light through the multi-reflection of various scattering centers. The RFG scattered Stokes light was then injected back to the Brillouin gain medium after port 3 of circulator 2, providing distributed feedback for the BRFL. As the pump power increased, the distributed feedback was amplified by the SBS to compensate for the round trip loss. The laser emitted after an isolator that was placed after the RFG to block the Fresnel reflection from the fiber connectors.

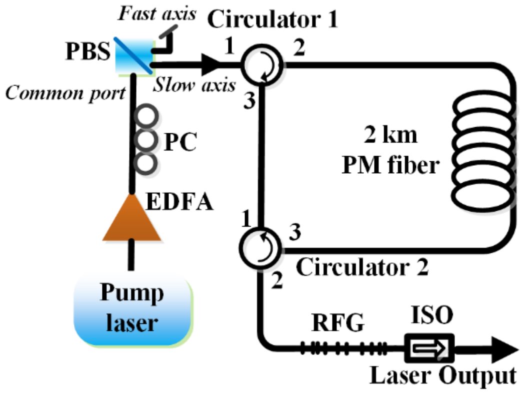

Figure 4-7 Experimental setup of the RFG based BRFL.

Figure 4-8 shows the measured output power of BRFL against the injected pump power. The threshold was measured to be 10.2 mW of injected pump power, and the slope efficiency was measured to be 0.293. Compared to the BRFL enabled by the distributed Rayleigh scattering in [58] that had a threshold power of 14.6 mW and slope efficiency of 0.254. The threshold power of the BRFL enabled by the RFG in our setup was decreased by 30.1%, and the slope efficiency was increased by 15.4%. Due to the intentionally induced large refractive index variation (10^{-4}-10^{-5}) by the femtosecond pulse laser, the reflection coefficient of the RFG was relatively high. The RFG had a reflection coefficient of around -30 dB while the reflection coefficient of the 500 m Rayleigh scattering fiber in [58] was around -50 dB. The relative high reflection coefficient leads to a low cavity loss and thus a high quality factor, which further improves the slope efficiency of BRFL. Therefore, the utilization of RFG is important to improve the lasing efficiency of BRFL.

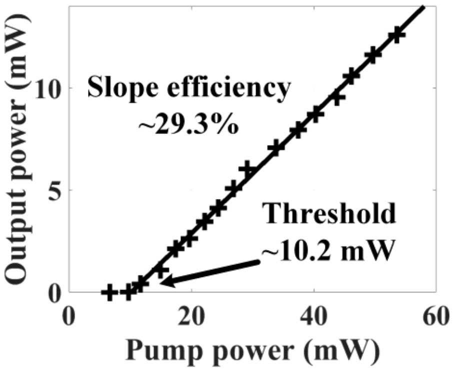

Figure 4-8 Laser output power versus pump power of the BRFL.

The intensity dynamics and the statistical features of the RFG enabled BRFL were characterized by measuring the temporal trace of the laser output through a PD and an oscilloscope. For comparison, SBS emission without distributed feedback from RFG was also characterized. When there was no distributed feedback, stochastics intensity fluctuation with an exponential probability distribution was observed in Figure 4-9 (a) and Figure 4-9 (b). The phase portrait was constructed by the two dimensional plot of temporal trace data points I_N vs I_{N+k} for delay $k = 1$, which exhibits motion on an outward spiraling and folding trajectory.

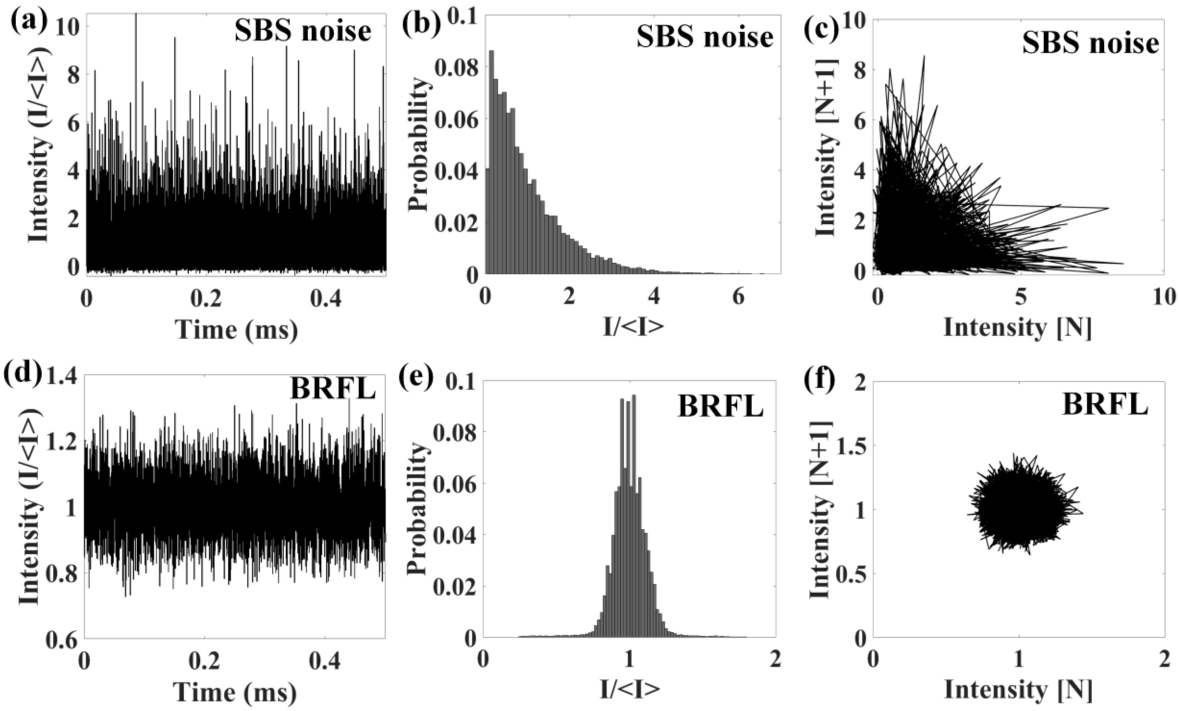

Figure 4-9 (a) temporal trace (b) power density distribution (c) phase portrait of intensity dynamics of SBS without distributed feedback from RFG; (d) temporal trace (e) power density distribution (f) phase portrait of intensity dynamics of Brillouin random lasing with distributed feedback from RFG.

Figure 4-9 (c) shows that there is little phase relation between the successive temporal points and reveals the chaotic nature of the amplified spontaneous Brillouin scattering process without lasing. In contrast, the statistical property of the temporal intensity traces is significantly modified as random lasing occurs that is enabled by the distributed feedback from the RFG. The temporal output trace of the BRFL follows a Gaussian probability distribution in Figure 4-9 (e) instead of the exponential probability distribution owing to the establishment of the random laser emission. The corresponding phase portrait in Figure 4-9 (f) shows a confined cycle signature, which means the successive temporal points are coherently related in phase with each other with the increasing mean path length and coherence time of the Stokes photons. The statistical feature of BRFL reveals that the thermal noise characteristics of lasing emission can be tamed by the distributed scattering from RFG, which shows promising prospects in generating the coherent narrow linewidth lasers.

The characteristic of the intensity fluctuations of the BRFL can be analyzed in a way comparable to RSB [207], which was used to quantify the phase transition from the paramagnetic to spin glass state in spin glass theory. To do the RSB analysis, the spectra of the intensity fluctuation was calculated by doing FFT of the temporal traces, as shown in Figure 4-10 (a)-(c). In order to compare the different properties of the temporal traces generated by different mechanisms, three types of Stokes light are analyzed which are SBS noise, Rayleigh scattering based BRFL, and RFG based BRFL, respectively. The Rayleigh scattering based BRFL was obtained by changing the RFG in the experiment setup to a 500 m long Rayleigh scattering fiber. The overlap of the intensity fluctuation spectra from trace to trace, which is known as Parisi parameter, can be calculated by the correlation between intensities of two traces a and b as [106]:

$$q_{ab} = \frac{\sum_{k=1}^{N} \Delta_a(k)\Delta_b(k)}{\sqrt{\sum_{k=1}^{N} \Delta_a^2(k)}\sqrt{\sum_{k=1}^{N} \Delta_b^2(k)}} \tag{4.6}$$

where N is the number of spectral points, $a,b=1,2,...,N_s$ denotes the trace labels, $N_s=100$ is the total number of traces, $\Delta_a(k)=I_a(k)-\bar{I}_a(k)$ is the intensity fluctuation, and the average intensity at the frequency indexed by k is $\bar{I}(k)=\sum_{a=1}^{N_s} I_a(k)/N_s$. Figure 4-10 (d)-(f) depict histograms including the probability distribution of q calculated for $a,b=1,2,...,100$ traces providing a total $100\times(100-1)/2$ values of q. For the SBS noise, values of q in Fig. 6 (d) are centered around the zero value, meaning the intensity fluctuation spectra from trace to trace are independent to each other. A similar phenomenon is found in the Rayleigh scattering based BRFL in Figure 4-10 (e), which also shows little correlation of the intensity fluctuation spectra from trace to trace, indicating a photonic paramagnetic regime that the lasing modes do not interact with each other. In the RFG based BRFL, with all modes highly interacting and frustrated by the disorder, q have all possible values in the range of (-1,1), with two maxima at $q = \pm 1$ and an emptied region around $q = 0$. Such behavior of the probability distribution of q reveals that the correlation between intensity fluctuation spectra in any two traces depends on the traces selected, which is a manifestation of RSB. In order to realize the replica symmetry breaking, it is important to use enhanced scatters of random configurations to enable their contributions are above noise floor among different traces, so that they are considered as “stable optical paths”. That is, the dynamics of their positions evolves on time scales much longer than the experiment time [208]. The difference of RFG based BRFL and Rayleigh scattering based BRFL relies on that the random lasing modes of the BRFL provided by the frozen scattering centers in RFG are more stable than that in Rayleigh scattering based BRFL. The Rayleigh scattering is susceptible to the environment, leading to uncorrelated intensity fluctuations of the BRFL from trace to trace. In contrast, the relatively large intentional induced refractive index variation of the RFG could tolerate environmental perturbation, which makes two traces have correlated intensity fluctuations. The result is consistent with that in Figure 4-6 (d), in which many narrow spectral peaks in reflection spectrum of random grating correspond to a large number of the random modes. Those distinct modes include different numbers of photons; the highest peak mode will generate random lasers. Because of a small spatial distance between neighboring grating periods, the radiation frequency difference is small within the same longitudinal mode, and hence the laser frequency fluctuation is much smaller compared with longitudinal mode spacing change in cavity laser. The manifestation of the RSB in the RFG based BRFL indicates a photonic spin-glass state, providing a photonic platform to study the glassy behavior of RFLs [209].

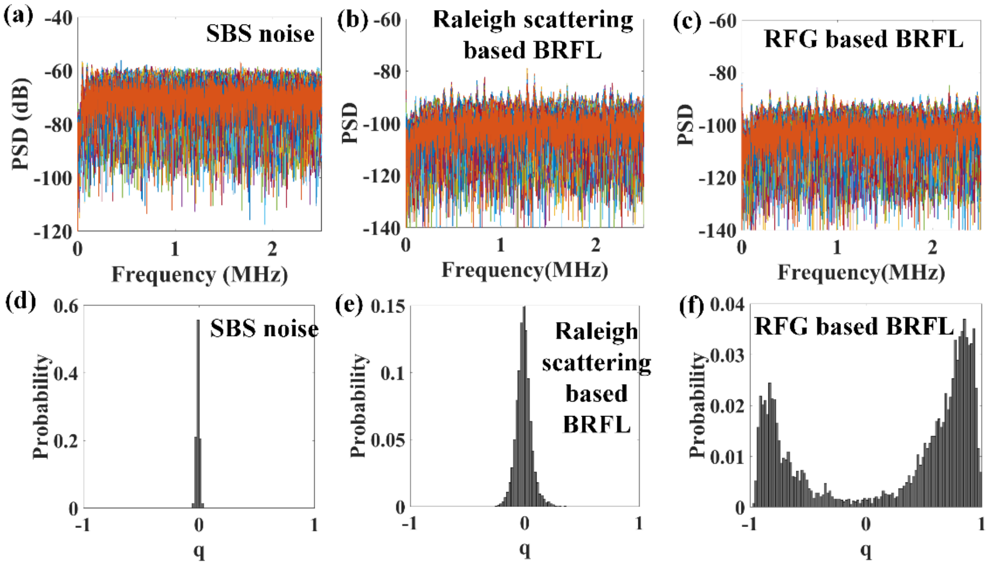

Figure 4-10 Intensity fluctuation spectra of (a) SBS noise (b) Rayleigh scattering based BRFL (c) RFG based BRFL; Probability distribution of q value of (d) SBS noise (e) Rayleigh scattering based BRFL (f) RFG based BRFL.

4.4 Conclusion

In this chapter, the property of the BRFL enabled by artificial random scattering is studied. First, the single longitudinal mode filter function of the weak FBG array or the Rayleigh scattering fiber in a BRFL is analyzed theoretically and demonstrated experimentally. The lights scattered by various scattering centers with random phase build interference with each other inside the distributed feedback medium, which is the multimode suppressing mechanism of the mode filter. To ensure the single longitudinal mode operation, the optimum length ranges from 50 m to 1 km for the BRFL with 1 km SBS gain fiber. Experimental results show that the weak FBG array within a certain length can not only provide single longitudinal operation, but also reduce the output temporal intensity fluctuation and intensity noise of the BRFL.

Then, a high efficiency BRFL constructed by the RFG is built and experimentally realized. The RFG that is used in the BRFL experiment is characterized by the time domain OCT method. Characterization results show constant average reflectivity of the RFG in the spatial domain. Frozen scattering centers are detected in the detailed structure of the RFG reflectivity in the spatial domain. The reflection spectra of RFG have a broad bandwidth due to the random phase shifts introduced in the RFG. A large number of narrow linewidth peaks were observed in the fine spectra structures of the RFG, which can act as narrow linewidth filters to select random lasing modes in random lasers. The slope efficiency of the RFG based BRFL is increased to 29.3%, demonstrating a high efficiency BRFL compared to the Rayleigh scattering based BRFL. Narrow linewidth of the random laser radiation on the order of kHz is characterized using DSH method. The RFG exhibits noise rejection effect in the output intensity dynamics of BRFL, which further show RSB in its spectra after doing the FFT analysis. The BRFL based on artificial controlled random scattering show improved performance at particular aspects, providing us a new perspective to understand the fundamental physics of the random lasing process.

Chapter 5 RFG enabled low noise BRFL

5.1 Introduction

Thermal and acoustic noises are crucial to the long-term stability of fiber lasers, as they introduce the fluctuation of optical path length on the laser cavity, and hence imposing undesirable intensity noise and frequency noise, particularly for an RFL with distributed Rayleigh scattering feedback from a long length fiber. Although the laser can be stabilized by the phase-locked loops at higher cost and complexity, its low frequency noise is limited by the response time of the feedback loop [210]. To reduce the intensity noise of BRFL, a linearly polarized BRFL with reduced frequency and intensity noise was developed with bidirectional pumping [59], which was then followed by a PM ring configuration with improved laser efficiency [58]. However, owing to the intrinsic susceptible nature of Rayleigh scattering along optical fibers, BRFLs based on Rayleigh scattering exhibit intensity fluctuation due to the unstable optical phase and amplitude of the feedback. Although the intensity noise of the BRFLs could be partly suppressed with the assistance of a RFG in SMF [110], the weak birefringence along the SMF-based random grating is sensitive to the external perturbation, which would deviate the state of laser polarization and impede further intensity noise suppression. Up to now, the role of polarization variation in an SMF-based random grating for RFLs has not yet been systematically studied. Especially in terms of the polarization-dependent SBS gain, the noise feature of the BRFL under environmental perturbations in a RFL has never been reported.

In the last chapter, the RFG has shown the potential capability of generating high efficiency and low noise BRFL. In this chapter, the properties of RFG was further studied experimentally by OFDR technique and theoretically simulated by the transfer matrix method in Section 5.1. Compared to the OCT method in the last chapter, the OFDR technique has higher SNR by employing the coherent detection technique [211]. Theoretically, the transfer matrix method [35] was used to simulate the grating properties by calculating the input and output fields over a short section of the sub-grating. The degree of randomness was introduced in the RFG in the simulation in order to study how the degree of randomness affects the grating's properties. In Section 5.2, we introduced a PM fiber-based random grating to provide the distributed feedback with maintained polarization for the thermal and acoustic noise insensitive BRFL for the first time. Compared to the Rayleigh scattering along PM fibers, the PM random grating fabricated by a femtosecond laser provided enhanced reflections with a high immunity to ambient temperature variance and acoustic noise. A theoretical model was developed to simulate the impact of environmental perturbations on the backscattering of a RFG and RS fiber, and the mitigated reflection fluctuation from the RFG was confirmed. Experiment results showed that the PM RFG-based BRFL exhibited 20 dB intensity noise suppression in the low-frequency domain (i.e., 10 Hz to 1 kHz), which was verified by intentionally introducing external temperature and sound disturbance on the PM random grating.

5.2 RFG characterization based on OFDR and transfer matrix method

5.2.1 OFDR Characterization setup

The OFDR setup is shown in Figure 5-1. The optical system was comprised of a tunable laser source, an auxiliary interferometer, a measurement interferometer, and an optical receiver system. With the tunable laser sweeping its output frequency linearly, an optical beat wave was generated in the auxiliary interferometer, which was used to trigger the sampling of the signal from the measurement interferometer at equal intervals of wavelength. In the measurement interferometer, the tunable light was launched into two arms: one arm was the reference arm and the other arm was connected to the grating under test. Light reflected from different positions along the grating generate different beat frequencies with the light in the reference arm. The beat signal was then collected by the photodetector and sent to the analog to digital conversion (ADC) system, which was the original real-valued signal that we got from the OFDR setup in the wavelength domain.

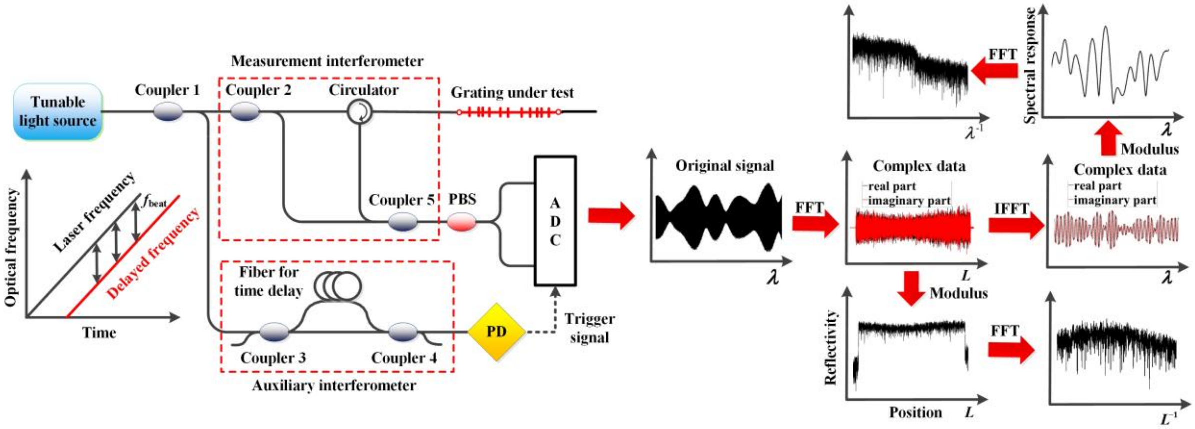

Figure 5-1 Experiment setup for RFG characterization and data processing method.

The data processing method that was used to characterize the RFG is shown on the right side of Figure 5-1. First, by doing FFT of the original real-valued signal in the wavelength domain, a complex data set containing the amplitude and phase of the reflectivity was calculated in the spatial domain. The reflectivity of RFG at different positions was then obtained by taking the modulus of the complex signal in the spatial domain. In order to study the reflectivity characteristics of the RFG along the spatial domain, an FFT was also applied to the modulus of the reflectivity for further analysis. At the same time, an appropriate window was applied to the complex data in the spatial domain with an inverse FFT to transform the signal back to the wavelength domain. The restored data in the wavelength domain was also a complex data set with its modulus representing the local spectral response of the selected locations of the RFG. The fine structures of the spectral response of the RFG was then analyzed with another FFT calculation.

In the experiment, two RFGs with different sub-grating period variation ranges were characterized. Both of the RFGs were inscribed by a femtosecond laser with the same pulse energy and comprised of a large number of uniform sub-gratings. The length of each sub-grating was 0.025 mm, and the total length of each grating was 50 mm. The difference was that the periods of the sub-gratings in the first RFG were randomly distributed between 0.5328 and 0.5436 µm with 10.8 nm maximum difference, which was much smaller than optical wavelength of 1.5 µm. In the second RFG, the period of each sub-gratings were randomly distributed from 0 to 2.5 µm [198]. The different scale of random period fluctuation in the RFG gave different degrees of randomness within the fiber medium. The degree of randomness describes the disorder of the system. For example, the RFG with a large sub-grating's period variation range has a relatively high degree of randomness and vice versa. In the following, we name the RFG with a high degree of randomness as a “high disordered RFG” and the other as a “low disordered RFG” for the convenience of description.

5.2.2 Reflectivity characterization of RFG in position domain

In order to characterize the reflectivity induced by the random period change of sub-gratings, the backscattering level was first measured by OFDR at different locations along the RFG, as shown in Figure 5-2. Figure 5-2 (a) and (b) show the backscattering strength of high and low disordered RFGs, respectively. The average backscattering strength per unit length of the low disordered RFG (-34 dBV/mm) was higher than that of high disordered

RFG (-54 dBV/mm) even though the refractive index modulation and grating length for both types of RFG are identical. In other words, a high degree of randomness reduced the reflection intensity of the RFG.

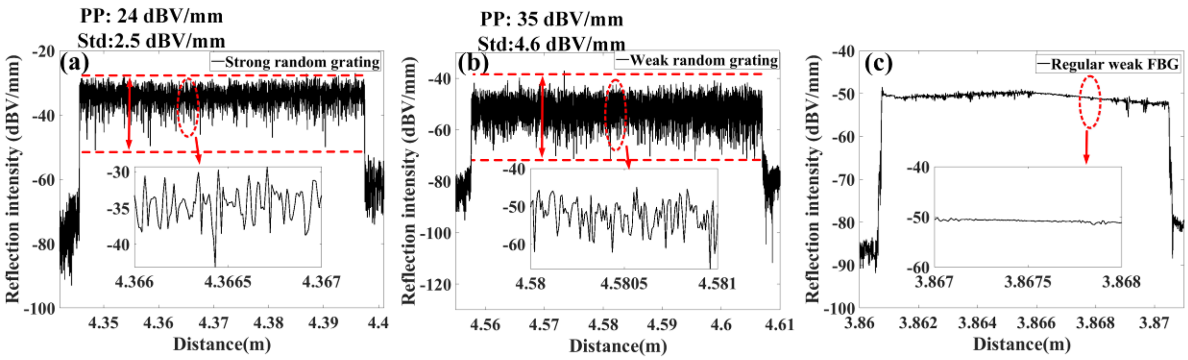

Figure 5-2 Reflectivity versus distance of (a) low disordered RFG, (b) high disordered RFG, and (c) regular weak FBG.

The reason behind the different reflectivity is that with a lower degree of randomness and smaller sub-grating's period variation (<10.8 nm) in the low disordered RFG, the random phase change of the backscattered light in a local region is less stochastic than that in the high disordered RFG with larger grating period fluctuation (<2.5 μm, which is larger than optical wavelength around 1.5 μm). This leads to partially correlated phase superposition in the low disordered RFG and uncorrelated phase superposition in high disordered RFG. As a comparison, the reflectivity of a regular uniform weak FBG was also measured. It can be seen in Figure 5-2 (c) that the reflection intensity of the regular weak FBG in the spatial domain was quite smooth, except for some small fluctuation at particular positions, which were caused by fabrication flaws. With an 8 μm spatial resolution of the OFDR setup, the measured data can be considered as reflection intensity from discrete reflectors separated by 8 μm along the RFG. The random period changes of the sub-gratings lead to reflection intensity fluctuations of these reflectors. The peak to peak value and standard deviation of these reflector's reflection intensity in the high disordered RFG were 35 dBV/mm and

4.6 dBV/mm, respectively. These values were much larger than the corresponding values (24 dBV/mm and 2.5 dBV/mm) for the low disordered RFG. Though higher degrees of randomness in the high disordered RFG gave rise to lower average reflection strength of each reflector, the local reflection strength fluctuation was much stronger in the high disordered RFG than that in the low disordered RFG.

To further illustrate the influence of the degree of randomness to the grating's reflectivity property, a probability histogram of the reflection intensity fluctuation period at every 1 mm range of the RFG was plotted. The reflection intensity fluctuation period here refers to the distance between two adjacent local minima points in Figure 5-2. It can be seen from Figure 5-3 (a) that for the low disordered RFG, the fluctuation period was most likely located at 50 μm. In contrast, Figure 5-3 (b) shows that the fluctuation period in the high disordered RFG was most likely located between 10 μm and 50 μm. Because the spatial resolution of the OFDR setup in the experiment was 8 μm, each point in Figure 5-2 represents the light reflection strength in the local area. The histograms of Figure 5-3 (a) and (b) indicates that the low disordered RFG showed periodical reflectivity features in the spatial domain, while the high disordered RFG exhibited stochastic reflection intensity distribution. The difference was also caused by the partially correlated phase superposition in the low disordered RFG and the stochastic phase superposition in the high disordered RFG. By selecting the RFG part in Figure 5-2 and doing a Fourier transform of the modulus of the reflection intensity, the intensity fluctuation frequency was calculated, as shown in Figure 5-3 (c) and (d). It can be seen that the relative intensity at each fluctuation frequency in the high disordered RFG was quite flat, indicating that there was no particular fluctuation frequency and the reflection intensity at different positions was totally randomly distributed. In contrast, the fluctuation frequency of the low disordered RFG showed an envelope where the maximum value was located between 10 mm^{-1} and 25 mm^{-1}, corresponding to the approximately 20 oscillations in the 1 mm range of the inset figure in Figure 5-2 (a). The periodic intensity fluctuation feature in Figure 5-2 (a) resulted from the relatively small period fluctuation range of the sub-gratings in the low disordered RFG. It is interesting to note that there was a small sharp peak at 38 mm^{-1} in Figure 5-3 (c), although it is hard for us to directly see the 38 oscillations of intensity fluctuation in the 1 mm range. The 38 mm^{-1} oscillation frequency in the spatial domain came from the inverse of the sub-grating's length (~0.025 mm). The sharp peak further proved that a low degree of randomness in a fiber grating would lead to periodic reflection intensity features in the spatial domain.

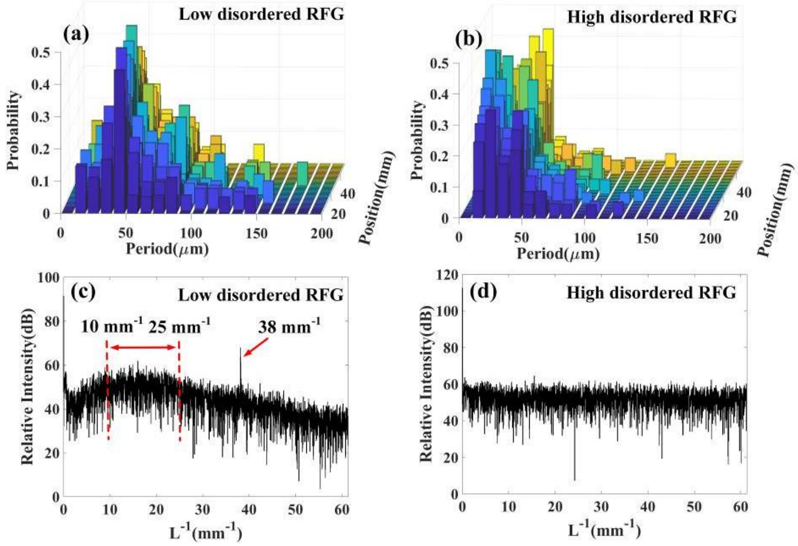

Figure 5-3 (a) Histogram of the reflection intensity fluctuation period at every 1 mm region of the low disordered RFG. (b) Histogram of the reflection intensity fluctuation period at every 1 mm region of the high disordered RFG. (c) Fourier transform of the reflection intensity of the low disordered RFG. (d) Fourier transform of the reflection intensity of the high disordered RFG.

5.2.3 Local spectral response characterization

Thanks to the high spatial resolution of the OFDR technique, the local spectral response of the RFG could be characterized. The influence of the grating length to the local spectral response property was first studied both in low and high disordered RFGs. It can be seen from Figure 5-4 (a) that when the interrogation length was chosen to be 40 µm and 80 µm, the local spectral response of the low disordered RFG only had one dominant peak, indicating that the refractive index fluctuation under the length of 80 µm was not random enough to create multiple reflection peaks in the spectral domain. When the interrogation length was increased to 200 µm, multiple reflection peaks started to appear due to the period change of the sub-gratings in the local region. The local spectral response in the high disordered RFG in Figure 5-4 (b) revealed different properties. When the interrogation length of high disordered RFG was chosen to be as small as 40 µm, multiple peaks still appeared in the local spectral response and the peak number increased as the interrogation length elongated. The local spectrum of the high disordered RFG showed a larger number of peaks than the low disordered RFG, which was caused by the relatively high degree of randomness in the high disordered RFG. As a comparison, the local spectral response of a regular weak FBG was also measured. It can be seen that for regular uniform FBG, there was only one dominant reflection peak regardless of the grating's length, illustrating that the higher degree of randomness would induce more reflection peaks in the spectral domain.

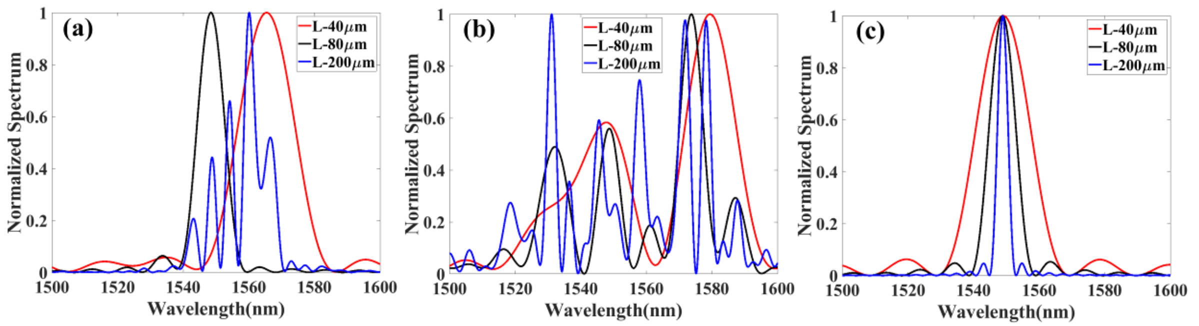

Figure 5-4 Local spectral response of (a) low disordered RFG, (b) high disordered RFG, (c) regular weak FBG at different lengths.

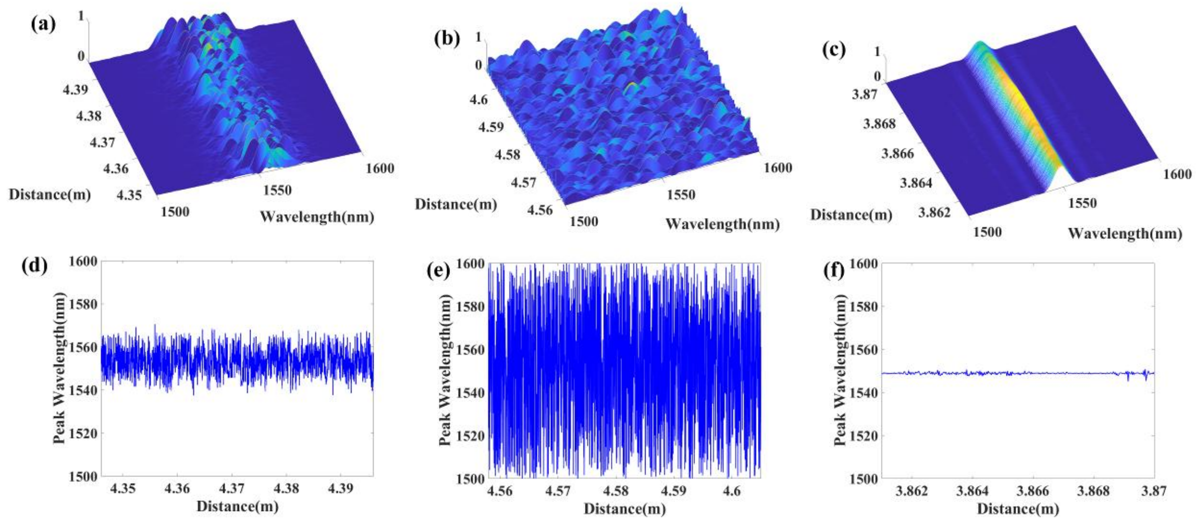

Figure 5-5 Distributed local spectral response of (a) the low disordered RFG, (b) the high disordered RFG, (c) a regular weak FBG at different positions. And the peak wavelength of the local spectral response of (d) the low disordered RFG, (e) the high disordered RFG, and (f) the regular weak FBG at different positions.

Figure 5-5 shows the distributed local spectral response of the low disordered RFG, high disordered RFG and a regular uniform FBG. The interrogation length was chosen to be 40 μm. The top three figures show their three-dimensional local spectral response at every position, and the bottom three figures are the corresponding peak wavelength value in the spatial domain. It can be seen that in the regular uniform FBG, the peak wavelength of the local spectral response was always located at 1550 nm, except for some small deviation at a particular position. The standard deviation of the distributed peak wavelength in regular uniform FBG was 0.1 nm. The reflection strength in the middle part was stronger than both sides of the measured uniform FBG, which also agreed with the reflectivity changing trend at different positions, as shown in Figure 5-2 (c). For the low disordered RFG, the peak wavelength of the spectral response at each local section randomly changed from 1540 nm to 1570 nm, with a standard deviation of 6.72 nm. In contrast, the corresponding peak wavelength of each local section in the high disordered RFG covered the total wavelength range from 1500 nm to 1600 nm, and the standard deviation was 26.65 nm, which was 4 times larger than the corresponding value in the low disordered RFG. Both the low and high disordered RFGs had a much larger standard deviation of distributed peak wavelength than regular uniform FBG. The local spectral response showed that the higher degree of randomness could provide richer reflection peaks for the RFG in the spectral domain and resulted in larger peak wavelength fluctuation in the grating's spatial domain.

5.2.4 Theoretical simulation of RFG

In the experiment, two different disordered RFGs were characterized, which gave a qualitative description about the influence of the degree of randomness to the gratings' property. In order to find the quantitative relationship between the degree of randomness and reflectivity of the RFG, the concept of entropy was introduced to describe the degree of randomness of the RFG. The period of each sub-grating can be regarded as a continuous random variable with uniform distribution. The probability density function of a random variable ranges from *a* to *b* with uniform distribution is:

$$p(x) = \begin{Bmatrix} \dfrac{1}{b-a}, a < x < b \\ 0, otherwise \end{Bmatrix} \tag{5.1}$$

Because the RFG is comprised of many sub-gratings that are independent of each other, the entropy of the whole RFG can be defined as [212]:

$$H(X_1, X_2 \cdots X_N) = N \cdot H(X) = -N \cdot \int p(x) \ln p(x) dx = N \cdot \ln \Delta P \tag{5.2}$$

where ΔP is the period variation range of all sub-gratings, N is the total number of sub-gratings, and $H(X)$ is the entropy of a sub-grating. The reflection spectrum of the RFG is simulated based on the transfer matrix method [213]. In the transfer matrix method, propagation of light characterized by the transfer matrix relates the amplitudes of the forward and backward propagating waves of each sub-grating on the right-hand side with those on the left-hand side:

$$\begin{bmatrix} a_n^+ \\ a_n^- \end{bmatrix} = M_n \begin{bmatrix} a_{n-1}^+ \\ a_{n-1}^- \end{bmatrix} \tag{5.3}$$

where a_n^+ and a_{n-1}^- are the transmission and reflection field of the n_{th} sub-grating, respectively. M_n is the transfer matrix of n_{th} sub-grating. The transfer matrix of the whole RFG can be written as the product of the transfer matrix of each sub-grating. From the coupled-wave equation of the counter-propagating waves, the transfer matrix of a single uniform sub-grating can be written as:

$$M_n = \begin{pmatrix} \cosh(SL_0) - i\dfrac{\Delta\beta}{S}\sinh(SL_0) & -i\dfrac{\kappa}{S}\sinh(SL_0) \\ i\dfrac{\kappa}{S}\sinh(SL_0) & \cosh(SL) + i\dfrac{\Delta\beta}{S}\sinh(SL_0) \end{pmatrix} \tag{5.4}$$

where L_0 is the length of each sub-grating. κ is the coupling coefficient between the counter-propagating beams in the gratings, which is determined by the refractive index modulation, $\Delta\beta = \beta - \pi / \Lambda$ is the wave-number deviation from the Bragg wavelength, Λ is the grating period, and $S = (|\kappa|^2 - \Delta\beta^2)^{1/2}$. The relationship between the entropy of the sub-grating and mean reflectivity of the RFG is simulated first, as shown in Figure 5-6. The main simulation parameters in Figure 5-6 are as follows. The refractive index modulation is 10^{-6}, and every 50 uniform index modulation periods form a sub-grating, and the total number of sub-gratings is 380. The mean reflectivity is calculated by averaging the reflectivity of the RFG in the spectral domain. The period variation range is divided by a constant P_0 ($P_0 = 1\,nm$) for normalization, thus the entropy of sub-grating is expressed as $\ln \Delta P / P_0$. The red curve is the result when the median value of the sub-grating's period is 0.5382 μm (corresponding to the central wavelength of 1550 nm) and the black curve is the result when the median value of the sub-grating's period is 0.6500 μm (corresponding to the central wavelength of 1872 nm).

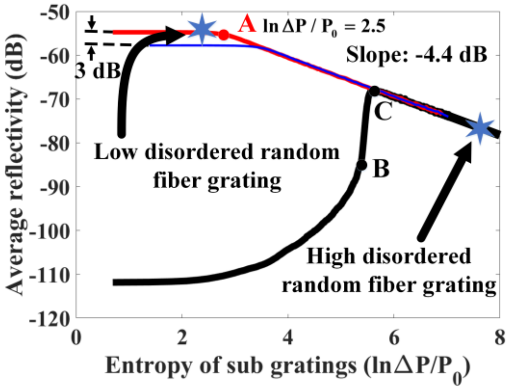

Figure 5-6 The relationship between the average reflectivity of RFG and entropy of sub-gratings (the red curve represent the median value of the sub-grating's period were 0.5328 μm, and calculated wavelength ranges from 1500 nm to 1600 nm. The blue curve represents the median value of the sub-grating's period are 0.5328 μm, and calculated wavelength ranges from 1450 nm to 1650 nm. The black curve represents the median value of the sub-grating's period are 0.6500 μm and calculated wavelength ranges from 1500 nm to 1600 nm.

The red curve shows that the mean reflectivity of the RFG remains almost constant when the sub-grating's entropy is smaller than 2.5 (before point A). This is similar to the conserved transmittance area theorem that is proved in [214], which claims that the total area under the curve of the transmittance in the reciprocal wave vector space remains constant regardless of the amount of disorder. However, when the grating's period variation range continues to increase after point A, the reflectivity in dB scale decreases linearly with the increase of the sub-grating's entropy. This is because the wavelength range in our simulation only covers from 1500 nm to 1600 nm. With increasing entropy of the sub-grating, the reflected energy is dispersed from the central wavelength to other wavelengths. If the dispersed wavelength range is smaller than the calculated wavelength range in the simulation (or wavelength range used for measurement in the experiment), the total reflectivity of the RFG remains constant.

When the sub-grating's entropy is large enough, the dispersed wavelength range would exceed our measured wavelength range, and the reflectivity of RFG at a fixed wavelength range would decrease exponentially as the sub-grating entropy increases. The two stars on the curve represent the two RFGs that were measured in the experiment by the OFDR setup. The period variation of the low disordered RFG in the experiment was 10.8 nm, corresponding to 2.38 of sub-grating's entropy ($\ln \Delta P / P_0 \approx 2.38$). The period variation of the high disordered RFG was 2.5 μm, corresponding to 7.82 of sub-grating's entropy ($\ln \Delta P / P_0 \approx 7.82$). The simulated average reflectivity of the high disordered RFG is 22 dB lower than that of the low disordered RFG, which is very close to the experiment result (~20 dB). Since the simulated random period of the sub-gratings is assumed to have a uniform distribution, the entropy of the high disordered RFG in the experiment was a little overvalued as the random period of the sub-gratings was more likely to be focused on a particular region. Considering this factor, the simulation results agreed well with our experimental results. The wavelength range is selected to be from 1500 nm to 1600 nm because the wavelength range of the tunable laser in the experiment is from 1500 nm to 1600 nm. A larger wavelength calculation range does not affect the mean reflectivity changing trend of the RFG. For example, the blue curve in Figure 5-6 represents that the calculated wavelength in simulation ranges from 1450 nm to 1650 nm. Since the wavelength range of the blue curve is two times larger than that of the red curve, the mean reflectivity in the blue curve is 3 dB smaller than that in the red curve when the entropy of sub grating is small, which means the total reflectivity of the RFG in these two cases is the same. When the entropy of the sub grating is large, the blue curve also shows that the average reflectivity of the RFG in dB scale decreased linearly as the entropy of the sub gratings increases. In order to study the reflectivity of the RFG that is out of the central wavelength range of the sub-grating, the median value of the sub-grating's period is set at 0.6500 μm, as shown of the black curve in Figure 5-6. When the sub-grating's period variation range is smaller than 0.0944 μm (before point B), the total reflectivity of RFG increases slowly as the sub-grating's entropy increases. The wavelength from 1500 nm to 1600 nm locates at the bandpass region of a uniform FBG with a grating period of 0.6500 μm, which is a result of the destructive interference of light. If small-period variation is introduced to the sub-grating, the destructive interference would be disturbed, leading to an increase of reflection intensity. When the sub-grating's period variation range is between 0.0944 μm and 0.1292 μm (between point B and point C), the total reflectivity of RFG increases dramatically as the increase of sub-grating's entropy. The dramatic increase relies on that the central wavelength of the sub-grating starts to cover the wavelength range from 1500 nm to 1600 nm when the sub-grating's period variation range is larger than 0.0944 μm. If the sub-grating's entropy continues to increase (after point C), the reflectivity of the RFG decreases exponentially as the increase of the sub-grating's entropy after the central wavelength of the sub-grating totally covers the wavelength range from 1500 nm to 1600 nm. In order to study whether the average reflectivity of the RFG is dependent on the number of sub-gratings or the total entropy of the RFG, the number of sub-gratings is changed from 300 to 400 while the total length of the RFG was fixed (10 mm). Due to the requirement of the slowly varying approximation in the transfer matrix method, the number of the periods in each sub grating should be a suitably large number. When the number of sub gratings is chosen to be 400, the period number of each sub grating is 47, which is large enough to ensure accurate simulation result [213]. The average reflectivity of the 10 mm long RFG is independent of the number of sub-gratings, which implies that the reflectivity of the RFG is determined by the entropy of each sub-grating rather than the total entropy of the RFG.

The relationship between the peak reflectivity of a regular FBG and $\ln(\kappa L)$ show different characteristics in the two conditions of $\kappa L << \pi$ and $\kappa L >> \pi$. When $\kappa L << \pi$, the peak reflectivity of an FBG in dB scale increases linearly with the increase of $\ln(\kappa L)$. In contrast, the peak reflectivity of an FBG is close to 100% if $\kappa L >> \pi$, as shown in Figure 5-7 (a). Figure 5-7 (b) shows the spectrum of an FBG at different conditions when $\kappa L = 1.6$ and $\kappa L = 20$. When random period variation of the sub-gratings is introduced into the grating, the peak reflectivity of the RFG is reduced and the criteria that $\kappa L << \pi$ or $\kappa L >> \pi$ previously used to estimate the grating properties is no longer valid. In order to find the proper criteria that can estimate the properties of the RFG, the peak reflectivity of the RFG is shown in Figure 5-7 (c–e). There is a linear relationship between the peak reflectivity of the RFG and $\ln \kappa / \kappa_0$ (κ_0 is a constant) with a slope of 8.8 dB when κ is relatively small, as shown in Figure 8c. Similarly, Figure 5-7 (d) shows that the relationship between the peak reflectivity and $\ln L / L_0$ (L_0 is a constant) is also close to linear with a slope of 4.4 dB when L is relatively small. According to the simulation results in Figure 5-7 (c,d) and Figure 5-6, we concluded that the peak reflectivity of the RFG was determined by $\kappa^2 L \Delta P$ rather than κL, as the slope of the linear part in Figure 5-7 (d) was two times the slope of the linear part in Figure 5-6 and Figure 5-7 (c). Figure 5-7 (e) shows the relationship between the peak reflectivity of the RFG and $2*\ln\kappa + \ln L - \ln \Delta P - \ln C$, where C was a dimensionless constant (C=10^{-5}). Since there were three variables κ, L and ΔP, there are three curves in Figure 5-7 (e), which is plotted by changing one of the variables among them and keeping the other two variables fixed. These three curves were overlapped with each other except when ΔP was smaller than 8 nm. The overlapping portion indicates that the peak reflectivity of the RFG was determined by $\kappa^2 L\Delta P$ when the random period variation ΔP was larger than 8 nm. When ΔP was smaller than 8 nm, the peak reflectivity property of the structure is similar to a regular FBG rather than Figure 5-7 (f) shows two typical spectral shapes of RFGs when $\kappa^2 L\Delta P >> C$ (red curve) and $\kappa^2 L\Delta P << C$ (blue curve).

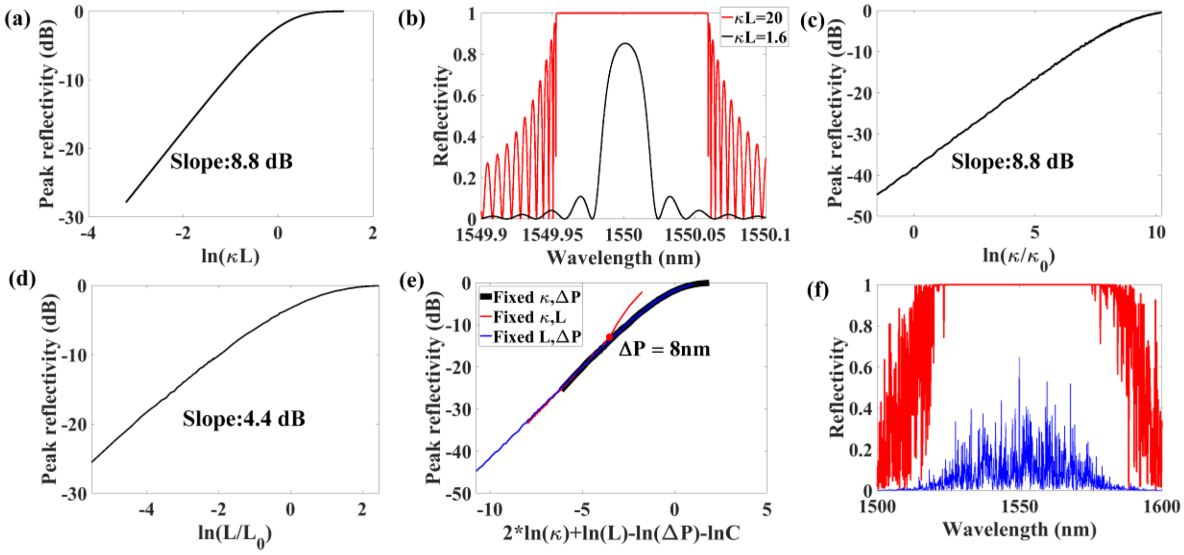

Figure 5-7 (a) Relationship between peak reflectivity of a FBG and $\ln \kappa L$. (b) Spectrum of a regular FBG when $\kappa L = 1.6$ (black curve) and $\kappa L = 20$ (red curve). (c) Relationship between peak reflectivity of a RFG and $\ln L / L_0$. (d) Relationship between peak reflectivity of a RFG and $\ln \kappa / \kappa_0$. (e) Relationship between the peak reflectivity of an RFG and $2*\ln \kappa + \ln L - \ln \Delta P - \ln C$ (black curve: fixed $\kappa, \Delta P$; red curve: fixed κ, L; blue curve: fixed $L, \Delta P$). (f) Spectrum of a RFG when $\kappa^2 L\Delta P >> C$ (red curve) and $\kappa^2 L\Delta P << C$ (blue curve).

5.3 RFG enabled low noise BRFL

5.3.1 Simulation of environmental perturbation to RFG

In optical fibers, Rayleigh scattering originates from optical property fluctuations. When the light is launched into the fiber, any fluctuation of the material such as non-uniform density leads to scattering on the scale of a subwavelength to form coherent Rayleigh scattering [167]. Compared to the Rayleigh scattering in the fiber, the RFG, fabricated by the "point-by-point" writing technique [198], has a micrometer inhomogeneity scale with higher index modulation induced by the femtosecond laser; i.e., the intrinsic refractive index fluctuations in the fiber are around 10^{-7} [215] while the indexes' change along the random grating can be up to 10^{-3} [216], as shown in Figure 5-8.

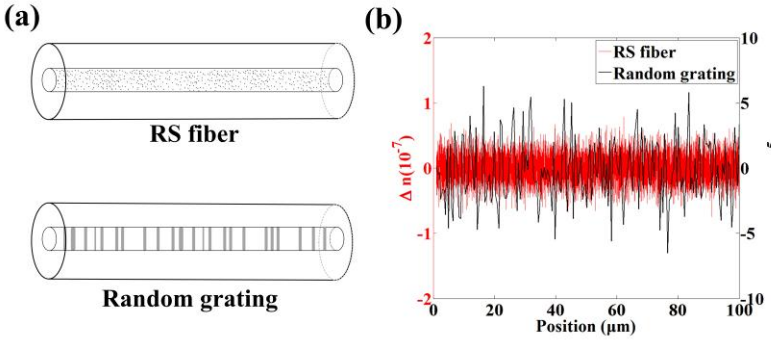

Figure 5-8 (a) Schematic of the refractive index fluctuation of RS fiber and random grating; (b) simulated refractive index fluctuation in RS fiber and random grating.

In the simulation, the scattering centers are randomly distributed along the fiber or the random grating. Because the fiber is a one-dimensional waveguide, the scattering centers in the fiber can be simplified to one-dimensional spots with a scattering length of l. Thus, the backscattered feedback can be expressed as the summation of all the scattered light from various scattering centers:

$$E_s = \sum_{j=1}^{N} \sqrt{R_j l_j} E_0 \exp(-i \frac{4\pi n f z_j}{c}) \tag{5.5}$$

where E_0 is the amplitude of the incident light, N is the total number of scattering centers, n is the refractive index of the fiber providing feedback, f is the optical frequency, z_j is the position of j_{th} scattering center, c is the light velocity in vacuum, R_j and l_j are scattering coefficient and scattering length of j_{th} scattering center respectively. Environmental perturbations such as vibration can lead to pressure fluctuation with time inside the fiber. The compressibility C of the fiber material then converts the pressure fluctuation into fiber density fluctuation, which can be calculated from the relation with sound velocity $v^2 = 1/C\rho$. The compressibility is given by:

$$C = \frac{1}{\rho}\frac{\partial \rho}{\partial p} \tag{5.6}$$

where p is the pressure inside the fiber, and ρ is the density of material. Since the change of the dielectric constant mainly depends on density fluctuation, we can express the change in the dielectric constant as:

$$\Delta\varepsilon = \frac{\partial \varepsilon}{\partial \rho}\Delta\rho = \frac{1}{\rho}\gamma_e \Delta\rho \tag{5.7}$$

where γ_e is the electrostrictive constant. Therefore, the pressure fluctuation with time caused by the environmental perturbation can affect the dielectric constant, which further leads to the change of the scattering coefficient of each scattering center and the reflected intensity. Another factor that can cause the instability of the reflected intensity is the temperature fluctuation of the environment. As the temperature increases or decreases, the scattering position and the scattering length of each scattering center will also change due to thermal expansion. The coefficient of linear thermal expansion is given by

$$\alpha_L = \frac{1}{l}\frac{dl}{dT} \tag{5.8}$$

where l is the length of RS fiber or random grating and T is the temperature of material. Based on Equations (5.5) - (5.8), we developed a relationship between pressure and temperature fluctuation with the fluctuation of reflected intensity. The main parameters used in the simulation are listed in Table 5-1.

Table 5-1. Main parameters used in simulations

Parameters		**Random grating**	**RS fiber**
Fiber length	$L\,(m)$	0.15	500
Scatters number	N	7.5×10^{4}	10^{7}
Mean value of refractive index fluctuation	$\mu_{\Delta n}$	10^{-4}	10^{-7}
Mean value of scatters length	μ_{l} (m)	10^{-6}	10^{-8}

Figure 5-9 (a) shows that temperature fluctuations have a larger effect on the reflected intensity of the RS fiber than that of random grating, indicating that the RS fiber is more environmentally susceptible compared to the random grating. The reason behind this relies on the temperature change being able to cause the position and length change of the scattering centers due to thermal expansion. Since the RS fiber has a much longer length than the random grating, the thermal expansion would have a stronger effect on the RS fiber than the random grating.

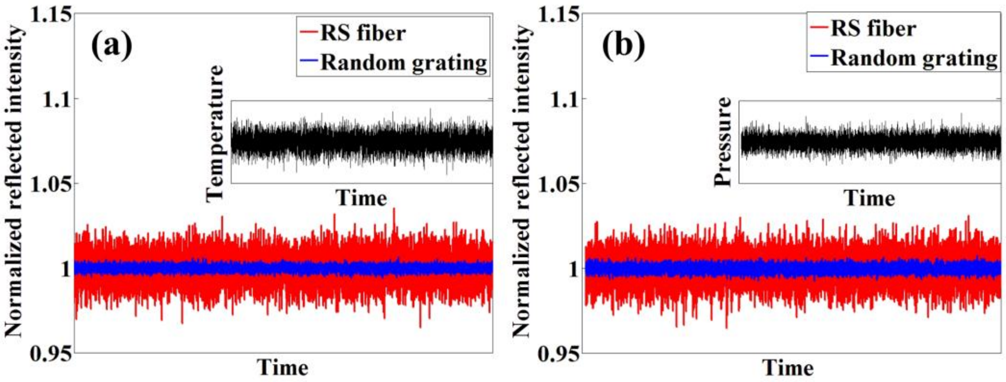

Figure 5-9 Simulation of the reflected intensity of RS (Rayleigh scattering) fiber (red) and random grating (blue) caused by (a) temperature fluctuation and (b) pressure fluctuation (black curve is the assumed pressure/temperature fluctuation).

Figure 5-9 (b) also indicates that the reflected intensity from the random grating is more stable than that from the RS fiber when the same pressure perturbation is exerted on them because the pressure fluctuation mainly changes the refractive index of the material. While the random grating has a larger refractive index contrast than the RS fiber, the relative refractive index fluctuation of the random grating is smaller than that in the RS fiber, resulting in a smaller scattering coefficient fluctuation and a more stable reflected intensity. Consequently, the compact random grating has more advantages in combating the environmental perturbation, which is usually the noise source of the random fiber laser in a low frequency range.

5.3.2 Experiment setup and results

The experimental setup is illustrated in Figure 5-10. The random fiber laser was pumped by a fiber laser with a 3.5 kHz linewidth. After being amplified by an EDFA, the pump laser was launched into PC 1 and a PBS to generate a linearly polarized pump laser. Then, the pump laser was injected into the random fiber laser cavity through a PM circulator. The Brillouin gain medium was a 5 km Panda-type PM fiber. After unidirectional passing through the circulators 1 and 2, the backscattered Stokes light from SBS was reflected by the PM RFG, which had a length of 150 mm. The random grating can provide random distributed reflection of the laser through the multi-reflection of various scattering centers created by the femtosecond laser. To compare the performance of the PM RFG to the RS fiber in BRFL, a 500 m long PM fiber was also used by replacing part A with part B in Figure 5-10. The red line in Figure 5-10 represents the PM fiber or PM component while the black line represents the SMF-based component. The reflected light from the random grating was then injected into a Fabry–Perot interferometer and the PC 2 to stabilize the random fiber laser. The bandwidth of the FPI is 30 kHz and its FSR is 20 MHz. By connecting the output of the PC 2 with the other end of the 5 km SBS gain fiber, light from the PC 2 provided the feedback for the Stokes lasing resonance in the ring cavity. To filter out the residual pump light, an optical filter was used after the random grating and the laser was emitted after the filter.

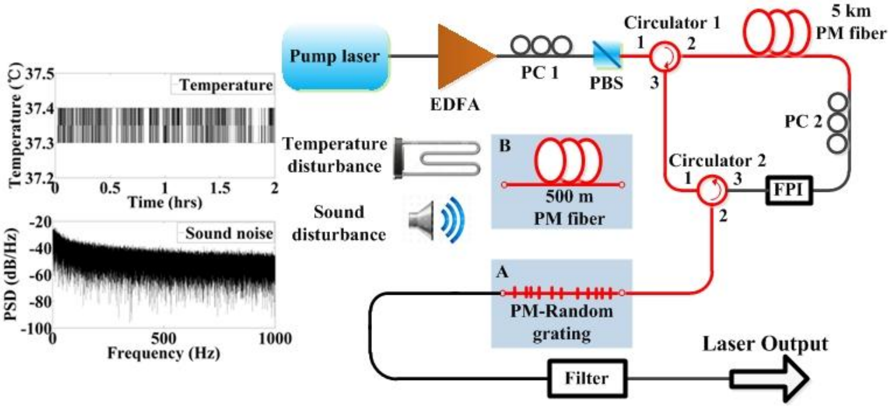

Figure 5-10 Experimental setup of BRFL based on PM random fiber grating.

The RIN power spectral density of the BRFL was characterized by recording and digitizing the temporal intensity fluctuation of the laser output through a photodetector with a 350 MHz bandwidth and an oscilloscope. The measurement time for each trace was 100 ms, and the sampling rate of the oscilloscope was 5 MHz. It can be seen from Figure 5-11 (a) that the intensity noise of the BRFL based on the RFG was much lower than that of the BRFL based on the RS fiber in the low-frequency region from 10 Hz to 1 kHz, which resulted from the less environmental perturbation on the RFG. Because of the short length of the RFG, it was intrinsically less disturbed by the environment, which also confirmed our theoretical analysis. In contrast, the Rayleigh scattering from the 500 m long PM fiber would be disturbed even if only a single point on the 500 m long fiber was affected by external perturbation. Moreover, the number of the longitudinal modes supported by the random grating was decreased significantly compared to the Rayleigh scattering fiber [110], which resulted in a less mode-hopping effect within the Brillouin gain bandwidth induced by the mode competition. Note that the suppressed mode density and mode-hopping effect relies on the specific random pattern of the random grating, which could provide a single dominant lasing peak for the BRFL. The frequency noise of the BRFL was also measured by an imbalanced symmetric 3×3 coupler Michelson interferometer with a delay fiber of 100 m long in one arm [217]. The two BRFLs had a similar frequency noise in the high-frequency domain (>1 kHz), as shown in Figure 5-11 (b). However, in the low-frequency domain (<1 kHz), the frequency noise of the BRFL with a RFG was lower than that of the BRFL based on the RS fiber, confirming that RFG was more stable and robust than the RS fiber in combating with the environmental perturbation. This external induced instability can modify significantly the phase and mode structure of the BRFL. In contrast, the PM RFG offers a stable feedback because of its short length, large refractive index contrast, and reduced density of reflecting centers. Hence, the RFG provides a more robust BRFL with lower frequency and intensity noise in the low-frequency domain.

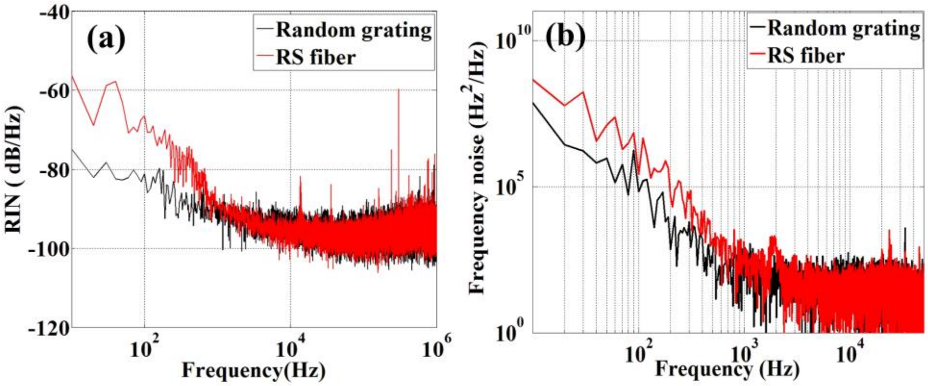

Figure 5-11 (a) RIN and (b) frequency noise of the BRFL based on random fiber grating and RS fiber.

To further verify the stable characteristics of the random grating, artificial temperature and sound disturbance were additionally placed on the random grating and RS fiber, respectively. The temperature disturbance was created by putting the random grating or the RS fiber in an oven with the temperature set to around 40 ℃. As shown in Figure 5-10, the temperature inside the oven was unstable and fluctuates with the time, thus resulting in a temperature disturbance on the fiber. The sound disturbance was generated by putting a loudspeaker with white noise besides the random grating or RS fiber. The intensity noise of the BRFL in the low-frequency range was measured when those external disturbances were added on the feedback medium. It can be seen from Figure 5-12 (a) that when the disturbance was introduced on the RS fiber, the intensity noise of the BRFL had a significant increase in the low-frequency domain. In contrast, the thermal and acoustic disturbance on the random grating had little influence on the intensity noise of the BRFL since the BRFL based on the random grating had similar intensity noise before and after the disturbance in Figure 5-12 (b), suggesting that the random grating can provide robust feedback for the BRFL.

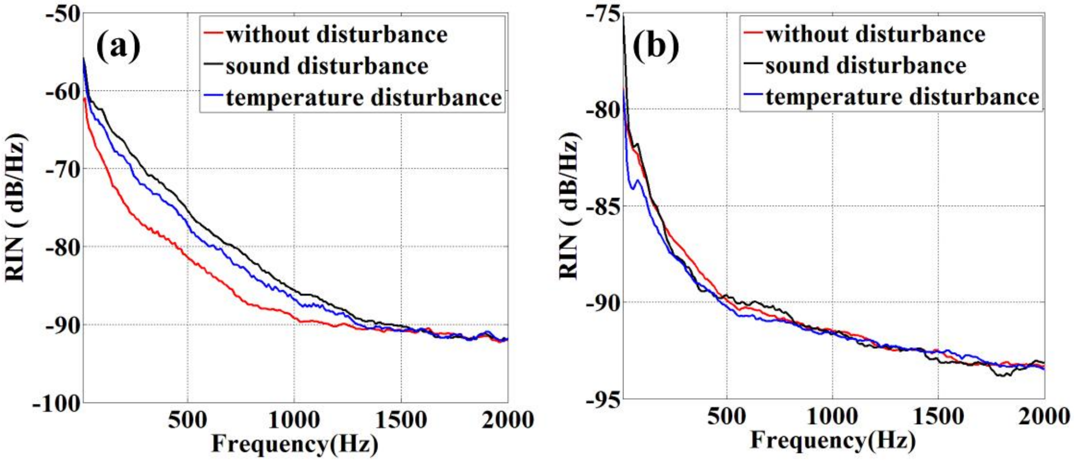

Figure 5-12 RIN of (a) the RS fiber-based BRFL and (b) the PM random fiber grating-based BRFL.

5.4 Conclusion

In this chapter, in order to design a low noise BRFL based on a PM RFG, the reflectivity and spectral properties of RFGs were characterized first by the OFDR technique and simulated based on the transfer matrix method. By comparing different characteristics of low and high disordered RFGs, influences of the degree of randomness to the grating’s backscattering strength and spectral response properties were qualitatively analyzed experimentally. Higher degrees of randomness in the RFG lead to lower light backscattering intensity with larger intensity fluctuations in the spatial domain. For low disordered RFGs, the low degree of randomness results in a specific intensity fluctuation period. For the local spectral response, a high degree of randomness leads to rich fine structures and a larger peak wavelength fluctuation range. The linewidths of the fine spectral features of the RFG shows a scaling behavior with the grating's length. The concept of entropy was introduced to describe the period variation of the RFG in order to establish the quantitative relationship between the grating's degree of randomness and its spectral properties. Simulation results show that the average reflectivity of a RFG is dependent on the sub-grating's entropy rather than the entropy of the total RFG. The average reflectivity of RFGs in dB scale decreases linearly as the increase of the sub-grating's entropy when the wavelength range for measurement is smaller than sub-grating's central wavelength fluctuation range.

Then, a noise suppressed BRFL in the low-frequency domain based on the PM fiber-based random grating was analyzed theoretically and demonstrated experimentally. The random grating had a larger spatial refractive index fluctuation and inhomogeneity scale, which provided more stable feedback than the RS fiber under the same environmental perturbation. Experimental results confirmed the temperature and vibration insensitive characteristics of the BRFL based on the random grating. In the frequency domain of less than 1 kHz, the BRFL based on the PM random grating showed a significant intensity noise and frequency noise suppression, paving the way for applications in the fields of coherent light sources, high-precision metrology, and optical sensing.

Chapter 6 Dynamic spectral properties of a dual-wavelength orthogonal polarization BRFL

6.1 Introduction

The frequency drift of a laser source can induce error in phase recovery of a phase sensitive OTDR system [218], which limits the low frequency detection ability of the sensing system, such as in the application of hydrophones. Though BRFL based on Rayleigh scattering has demonstrated good performance in generating highly coherent photons, the time dependent frequency drifts in BRFL have not been studied. Compared with RFLs based on Raman gain, Brillouin gain with narrow bandwidth intrinsically provides a narrow linewidth filter for the random lasing process. The narrow linewidth spectra in coherent BRFLs are on the order of sub kHz [55], which poses a problem to characterize such a narrow linewidth spectrum and its dynamics because of the insufficient resolution and scanning rate of traditional optical spectrum analyzers. Although DSH method has been used to characterize the narrow linewidth of BRFL [58], it cannot measure real-time laser frequency drifting and spectra dynamics in the time domain, as it measures correlation trace at the delayed time, which gives the phase noise information. The frequency information can be obtained by measuring the beat frequency between the laser under test and the reference laser oscillator, for instance, the heterodyne based method can be used to obtain the information. The spectral dynamics exhibit laser frequency stability and its intensity fluctuation characteristics, which is important to understand laser radiation process and its underlying physics. In this chapter, the heterodyne based method was implemented to measure the spectra dynamic properties of a dual-wavelength BRFL with orthogonal polarization. In the heterodyne based method, the output of the BRFL was mixed with the pump light which acted as a local oscillator. The optical spectra were reproduced by the heterodyne beat frequencies, given by the difference between the instantaneous optical frequency of BRFL and the local oscillator. The spectral dynamics of the dual-wavelength BRFL was characterized, in which polarization dependent and polarization independent spectra drift between two orthogonal polarizations were found. The intensity fluctuation of the lasing spectra and spectral correlations at different part were also analyzed considering the environmental perturbation factor. To the best of our knowledge, this is the first characterization and analysis of the spectral dynamics of BRFL.

6.2 Experimental setup of the dual-wavelength BRFL

The experimental setup of the dual-wavelength orthogonal polarization BRFL is shown in Figure 6-1. The pump light source was based on a 3.5 kHz linewidth fiber laser (Rock Module, NP Photonics) which was amplified by an EDFA. After the EDFA, the polarization of pump light was carefully adjusted by a PC to distribute power of pump light equally in *x* polarization and *y* polarization. Then, the pump light was split into two paths by a PM coupler. After the PM coupler, one path was used to generate beat signal with BRFL, the other path was injected into the Brillouin gain medium of BRFL through circulator 1. The Brillouin gain medium was a 2 km Panda-type PM fiber with fiber loss of 0.296 dB/km and a mode field diameter of 6.48 μm at wavelength of 1550 nm. The pump light in the Brillouin gain medium could stimulate backward Stokes light which travel anticlockwise between PM circulator 1 and PM circulator 2. After port 2 of PM circulator 2, the Stokes light experienced Rayleigh scattering provided by a 500 m PM fiber. The Rayleigh scattered Stokes light was then injected back to the Brillouin gain medium after port 3 of circulator 2, providing distributed feedback for the BRFL. The BRFL was emitted from the 500 m PM Rayleigh scattering fiber. To measure dynamic spectral properties of the BRFL, the pump laser and the BRFL were combined by a coupler and then detected by a PD. The beat spectra on the PD was then collected by an ESA to analyze the spectra dynamics of the BRFL. The utilization of PM fibers and components in the experiment offer us a perfect way to generate dual wavelength random fiber laser with orthogonal polarization. Because the Brillouin gain medium of the 2 km PM fiber in our experiment has a smaller effective mode field diameter of 6.48 μm than that of a single mode fiber (10.4 μm), it can provide a higher Brillouin gain coefficient for BRFL. At the same time, the two dimensional stresses from Baron-doped-silica rods in the PM fiber introduce different Brillouin gain spectrum in slow axis and fast axis, providing dual wavelength random fiber lasing with orthogonal polarization. More importantly, large birefringence induced by stress rod can help to maintain polarization of the dual wavelength BRFL during its propagation in the corresponding principal axis of PM fiber, which give us the opportunity to study their respective spectra dynamics in the time domain.

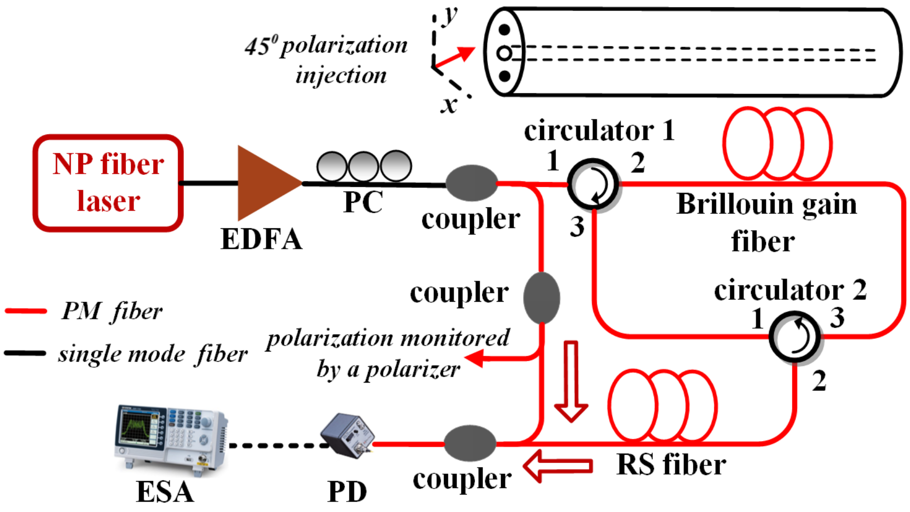

Figure 6-1 Experimental setup of the dual-wavelength orthogonal polarization BRFL (RS: Rayleigh scattering).

6.3 Spectra dynamics of BRFL

The beat spectra between the pump laser and the dual-wavelength BRFL were measured in the time domain, as shown in Figure 6-2, which is the top view of the three dimensional beat spectra measured at different time. The measuring time for each trace is 2.18 ms. It is shown that the beat spectra between the pump laser and the dual-wavelength BRFL is not stable and fluctuate with time. Those kinds of fluctuation can be divided into two categories, polarization dependent fluctuation and polarization independent fluctuation. The polarization dependent fluctuation manifests as random optical frequency jumps which lead to random changes of the frequency difference between the two wavelengths of the BRFL. In contrast, for the polarization independent spectra fluctuation, the frequencies of the dual-wavelength BRFL in orthogonal polarizations fluctuate in the same manner, where the frequency difference remains relatively stable in the time domain. It can be seen in Figure 6-2 that the polarization independent spectral fluctuations manifest as smooth random frequency shifts and account for most of the time in the time domain. There are mainly three reasons that lead to the spectral fluctuations of the BRFL. Firstly, the Brillouin gain spectrum is different at different locations of the Brillouin gain medium which is caused by the non-uniform longitudinal distributed refractive index and birefringence of the SBS gain fiber. Therefore, the gain competition at different locations of the Brillouin gain medium lead to unstable lasing frequency. Secondly, the temperature changes of the Brillouin gain fiber caused by environmental perturbation provides fluctuating gain spectrum in the Brillouin gain medium, which is the main reason for the polarization independent frequency fluctuation of BRFL. Because the temperature in both slow and fast axis experiences the same environmental perturbation, the Brillouin gain spectrum in both axes also fluctuate in the same manner accordingly. Thirdly, the Rayleigh scattering fiber which provides feedback for BRFL acts as a narrow linewidth filter that selects only one lasing mode in each direction of polarization. Any perturbation on the Rayleigh scattering fiber could lead to the change of the filter property, which then cause the random lasing frequency fluctuation in the time domain. Note that, although the pump laser from NP Photonics Rock module also has frequency drifting, it has little influence on the beat spectra between the pump laser and the dual-wavelength BRFL. This is because the ratio of the Brillouin frequency shift is governed by $\upsilon_B = \left(2n\upsilon_a / c\right)\upsilon_0$, where n is the refractive index of the fiber, υ_a is the speed of the acoustic wave, c is the light speed in vacuum, and υ_0 is the frequency of the pump laser. When the frequency of pump laser υ_0 is drifting on the order of MHz, the frequency change of the beat spectra is only on the order of several Hz, which is much smaller than the frequency changes that are measured in the experiment.

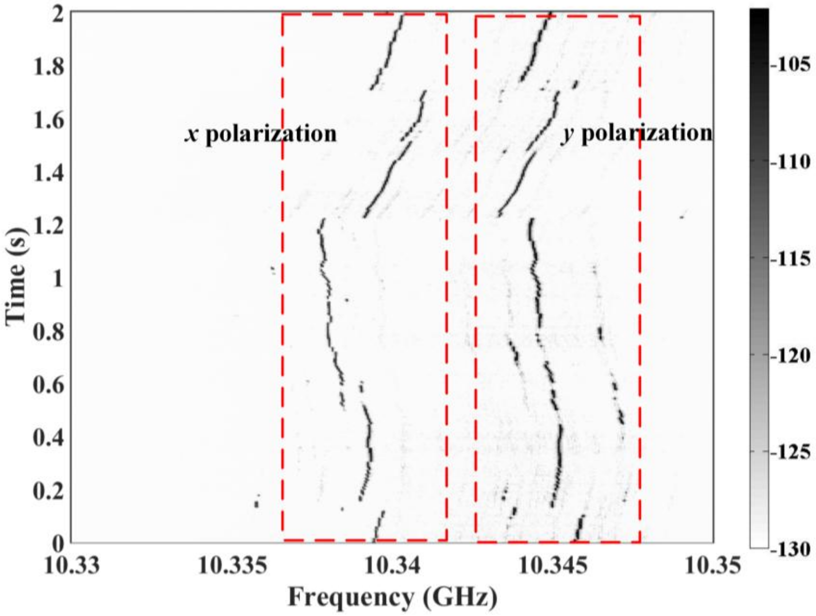

Figure 6-2 Dynamic beat spectra evolution of the dual wavelength orthogonal polarization BRFL.

The frequency variations of the BRFL at both polarizations are further analyzed statistically by calculating the relative frequency variations at both polarizations. The relative frequency variations denote $f_x - \langle f_x \rangle$ in *x* polarization, and $f_y - \langle f_y \rangle$ in *y* polarization. Figure 6-3 (a) and (b) show the probability distribution of the relative frequency variations in *x* polarization and *y* polarization respectively. It can be seen that there is a dip near the central part of the probability distribution graph at both *x* polarization and *y* polarization, which is caused by the spectral hole burning of the SBS process. The spectral hole burning is a typical phenomenon in the laser radiation with inhomogeneous broadened absorption lines of the atomic medium. In the SBS process, it was demonstrated in [219, 220] that the spectral hole burning can happen in a homogeneous broadening medium of the Brillouin line. The dip near the central spectral line is due to both the gain saturation and the coupling between the pump and random laser perturbations that counter propagate around the steady state intensity profiles. Figure 6-3 (c) shows the laser frequency difference between *x* polarization and *y* polarization, i.e. $f_y - f_x$. It is interesting to note that the laser frequency difference shows discrete features, which manifest that the random modes in the BRFL is also discrete. Because the environmental perturbations, such as the temperature change, lead to polarization independent laser frequency variation, the frequency difference $f_y - f_x$ can eliminate the influence of the environmental perturbations. Therefore, the change of the frequency difference of orthogonal polarizations reflect the random mode change of the BRFL due to the gain competition. Figure 6-3 (c) demonstrates discrete random modes in BRFL though distributed Rayleigh scattering fiber is used in building the random laser. It reflects random mode hopping of the Stokes frequency change, which is caused at different fiber locations.

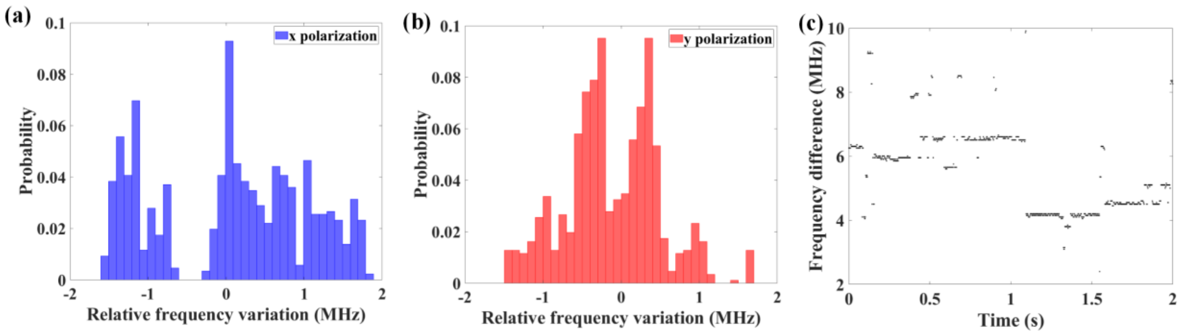

Figure 6-3 (a) Probability distribution of the relative frequency variation of the BRFL in *x* polarization; (b) Probability distribution of the relative frequency variation of the BRFL in *y* polarization; (c) Frequency difference of the BRFL in *x* polarization and *y* polarization.

The relative intensity of the lasing peak in the time domain is plotted in Figure 6-4 (a), which represent the intensity evolution in each polarization. The polarization of the pump light is carefully adjusted by the PC before it is launched to the Brillouin gain fiber, so that the pump power is equally split into two orthogonal polarizations. The intensity of the BRFL in both polarizations are not stable in the time domain due to the environmental perturbation and gain competition. By doing Fourier transform to the relative peak intensity of the beat spectra, the relative intensity noise of the lasing peak at both polarizations are calculated, as shown in Figure 6-4 (b). It should be noted that the intensity noise in Figure 6-4 (b) is different from the intensity noise measured in the previous literature [59]. In [59], the intensity noise characterizes the fast dynamics of the laser output power, while the intensity noise measured by the heterodyne technique in this experiment characterizes the intensity dynamics of the dominating lasing mode of the BRFL. Due to the random nature of environmental perturbation, the peak intensity noise in the frequency domain is flat which is similar to the white noise. The probability distribution of the relative intensity of the dominating lasing peak shows a Gaussian distribution, as shown in Figure 6-4 (c) and (d). Note that, though it was proved in [58] that the output intensity of the BRFL above the lasing threshold follows the Gaussian distribution, this is the first demonstration that the intensity of the dominating lasing peak of the BRFL also follows the Gaussian distribution. The Gaussian distribution happens for an initial partially random signal passing many random lengths [102]. When the mode structure created by the random lengths of the frozen scattering centers are matched to the lasing mode of the BRFL, the lasing mode reaches the highest gain with maximum output intensity. The deviation of the lasing mode from the localized mode created by the random scattering medium lowers the output intensity of the lasing peak. The Gaussian distribution of the relative intensity of the lasing peak manifests that the frequency fluctuation of the lasing peak is a totally random process induced by the environmental perturbation and random mode competition for limited SBS gain.

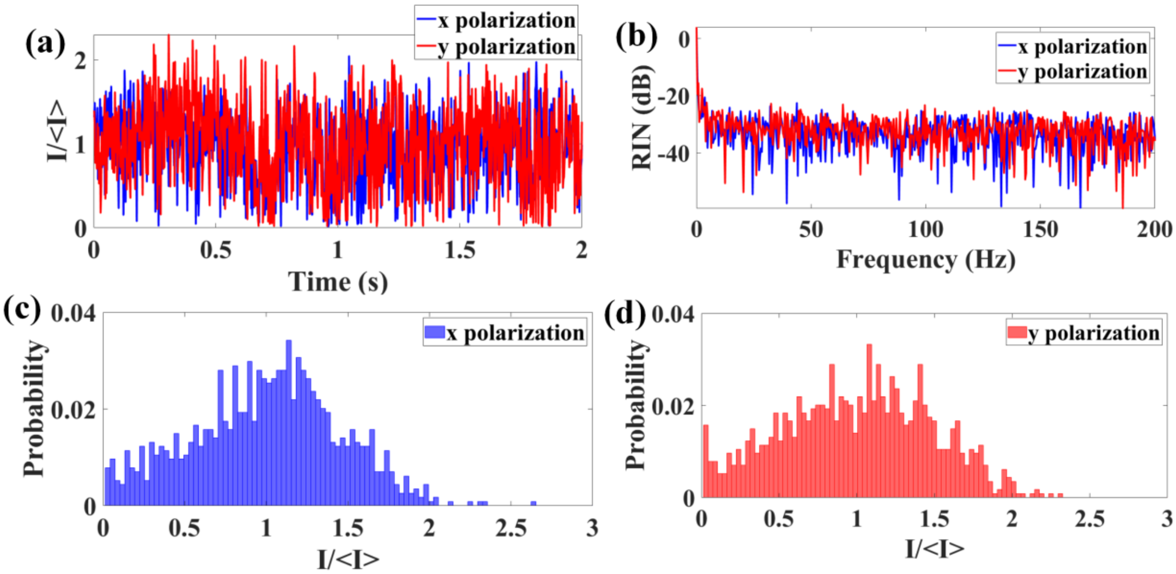

Figure 6-4 (a) Relative intensity of the dominating lasing peak of the BRFL in *x* polarization and *y* polarization; (b) Relative intensity noise of the dominating lasing peak of the BRFL in *x* polarization and *y* polarization; (c) Probability distribution of the relative intensity of the dominating lasing peak of the BRFL in *x* polarization; (d) Probability distribution of the relative intensity of the dominating lasing peak of the BRFL in *y* polarization.

The ensemble averaged beat spectra are studied which shows the average statistical temporal-spectra evolution property. In order to discriminate the beat spectra from different polarization, the power of pump light in slow axis is reduced to be slightly lower than that in fast axis by adjusting the polarization state of the pump source. Therefore, the intensity of beat spectra from polarization *y* is also lower than that from polarization *x*, as shown in Figure 6-5. In [221], the ensemble averaged spectrum of coherent random laser is a smoothed curve which is similar to spectrum of random lasers with non-resonant feedback. In contrast, in BRFLs, although the total average time of the beat spectra is on the order of seconds, the narrowband peaks still appear and survive, which is much longer than the time of flight in the 2 km Brillouin gain fiber. Compared to the spontaneous Brillouin gain spectrum, the ensemble averaged spectrum carries the intrinsic signature of the gain profile. In order to characterize spectral correlations in the dual-wavelength orthogonal polarization BRFLs, Pearson's correlation coefficients $\rho(\lambda_1,\lambda_2)=\mathrm{cov}(\boldsymbol{I}_{\lambda_1},\boldsymbol{I}_{\lambda_2})/(\sigma_{I_{\lambda_1}},\sigma_{I_{\lambda_2}})$ are calculated based on the measured beat spectra. This approach has been used to describe underlying spectral correlations between sidebands in modulation stability [222], spectral correlations in supercontinuum generation [223], and in Raman random fiber lasers [120], which are combined with real time spectral measurement based on dispersive Fourier transformation or the FP-based configuration. As the spectral resolution of FP-based configuration is not enough to measure linewidth on the order of sub kHz and the dispersive Fourier transformation method can only be used in pulse regime, the heterodyne method offers a way to study such correlations for ultra-narrow linewidth generation in continuous wave BRFLs. Figure 6-5 (b) shows the matrix of ρ values, where the diagonal line corresponds to the averaged beat spectra obtained in Figure 6-5 (a) . The peaks of the Pearson's correlation coefficient beyond the diagonal line have discrete positions in regard to the frequency difference of the dual-wavelength BRFL. These discrete positions are caused by the narrow linewidth spectral generation and strong spectral correlations between the two wavelengths of the BRFL. When the frequency of BRFL jumps from one position to another, the frequency difference changes and creates multiple peaks in the Pearson's correlation coefficient matrix. The correlations of the beat spectra between the orthogonal polarizations correspond to the polarization independent spectra variations in Figure 6-2, in which the spectra with orthogonal polarization shifts in the same manner. The estimation of the Pearson's correlation coefficient aided by the heterodyne spectral measurement method offers a simple and straightforward method of checking the existence of spectral correlations in BRFLs.

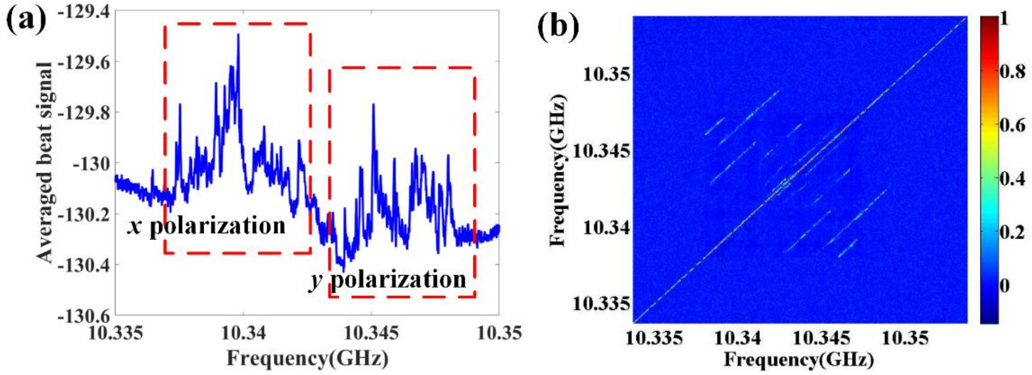

Figure 6-5 (a) Averaged beat spectra of the BRFL and (b) Pearson's correlation coefficient of the spectra of the BRFL.

6.4 Conclusion

In conclusion, the dynamic spectral properties of a dual-wavelength BRFL with orthogonal polarizations are studied. Due to the large birefringence of the PM fiber, the Brillouin gain spectrum of the PM fiber at orthogonal polarization is different. The spectrum of the BRFL fluctuates continuously in the time domain in two distinct manners, which are polarization dependent spectral variation and polarization independent spectral variation respectively. Spectral hole burning of the Brillouin gain is found by analyzing the probability distribution of the relative frequency variation of the dual-wavelength BRFL. The intensity of the dominating lasing mode exhibits Gaussian probability distribution, revealing a totally random process caused by the gain competition and environmental perturbation. The long time averaged spectra of the BRFL still remain narrow linewidth spikes, indicating the increased coherent time of BRFL. Spectral correlations of the BRFL are studied which reflect the gain competition and potentially give rise to spatially dependent spectral dynamics. Exploration of the nature of such underlying correlations can have profound implications in the future design of RFLs.

Chapter 7 Summary and future work

7.1 Summary

This thesis investigates the characteristics of BRFL and proposes a low noise BRFL based on a PM RFG. The background of RFLs, including its categories, development and applications is reviewed and discussed. Theory involved in BRFL is presented to describe its spectral properties and noise properties from the origin of the random scattering process. Below is the summary of the thesis:

(1) An acoustic wave detection method to monitor the internal working state of BRFL is proposed based on the SBS enhanced polarization decoupled FWM process. By using a continuous probe light, the phase noise and intensity noise of the intrinsic acoustic wave are characterized. The acoustic wave is generated by a linearly polarized high power pump laser in the gain medium of BRFL and detected by a second low power probe laser with orthogonal polarization. In the experiment, different linewidths of lasers are utilized as the pump source, where the phase noise and spectral width of the acoustic wave is found to be determined by the spectral convolution of pump light and its Stokes light. The influence of phase noise in the acoustic wave on the linewidth of the BRFL is studied. It is found that BRFL's linewidth could be broadened by the phase noise of the acoustic wave, although the dominating factor to the linewidth of BRFL comes from the coherent distributed feedback provided by Rayleigh scattering. The intensity dynamics of the reflected probe light are studied with different linewidths of pump light and probe light. When both the pump light and probe light have a narrow linewidth (on the order of several kHz), the intensity dynamics of the reflected probe light follow the output intensity of BRFL well with the Gaussian

output intensity probability distribution. In contrast, stochastic noise features are introduced to the intensity dynamics of the reflected probe light with the exponential probability distribution when the broad linewidth light source is used as the pump light or probe light.

(2) The statistics of the intensity of the distributed acoustic wave is measured based on the OTDR technique. By sending pulses with frequency close to resonance frequency of the dynamic grating, the distributed information of the acoustic wave in BRFL is characterized. Depending on whether sweeping the frequency of the probe light or not, the distributed detection process is divided into static measurement and dynamic measurement. In the static measurement, the distributed Brillouin gain spectrum is measured by sweeping the frequency of the probe light, in which we find that the Brillouin gain of BRFL depletes exponentially along the Brillouin gain fiber. In addition, the Brillouin gain depletes more quickly at the initial part of the Brillouin gain fiber when the photons of the probe light absorb energy from the acoustic wave. The dynamic detection is realized by sending a series of pulsed probe light with 10 kHz repetition rate, which reveals that the noise source of BRFL first appears at the initial part of the Brillouin gain fiber and the phase noise of the random laser induces the nonlinear change of the interference dark spots in the spatial-time map. Optical rouge waves are found in BRFL with different proportion at high gain position and low gain position, which is caused by the nonlinear amplification of the SBS process.

(3) The output characteristics of the BRFL are studied by controlling the property of the distributed random feedback medium. Two types of artificial random medium are investigated, which are FBG array with random spacing and RFG with random periods. By controlling the length of the FBG array, the single longitudinal mode filter function enabled by distributed feedback is proposed and demonstrated for the first time to reveal the mode selection mechanism in BRFL. Theoretical calculation based on light interference and multi-

reflection in the fiber shows the weak FBG array (-40 dB reflection) acts as the mode filter, whose performance is related to the length of the FBG array. The optimum length ranges from 50 m to 1 km for the BRFL with 1 km SBS gain fiber. Compared to the Rayleigh scattering, the strong refractive index modification in RFG enhances the backscattering strength, which improves the slope efficiency of BRFL to 29.3% and reduces the lasing threshold to 10.2 mW. Because the relative stable frozen scattering centers in RFG, the glassy behavior of BRFL is demonstrated which manifests as a photonic spin glass phase signaled by RSB.

(4) The influence of the degree of randomness to the properties of the RFG are investigated theoretically and experimentally. In the experiment, two RFGs with different degree of randomness are characterized by the OFDR technique, which shows that a high degree of randomness leads to low average reflectivity and strong reflectivity fluctuations of the RFG in the spatial domain. Theoretically, the concept of entropy is introduced to describe the degree of randomness of the RFG. A linear relationship between the sub-grating's entropy and the average reflectivity of the RFG in dB scale are demonstrated. Then, based on a PM RFG, a low noise BRFL that are insensitive to the environmental perturbation is demonstrated. A theoretical model is developed to simulate the impact of environmental perturbations on the backscattering of RFG. The proposed low noise BRFL exhibits 20 dB intensity noise suppression in the low frequency domain from 10 Hz to 1 kHz compared to the BRFL based on Rayleigh scattering, paving the way for its applications in the fields of coherent light sources, high precision metrology and optical sensing.

(5) The dynamic frequency drifts of a dual-wavelength BRFL with orthogonal polarizations are characterized experimentally. The BRFLs are generated in slow axis and

fast axis simultaneously by launching a 45^0 linearly polarized pump light to the PM Brillouin gain fiber. The frequency fluctuations of the BRFL can be divided into polarization dependent variations and polarization independent variations, depending on whether the frequency drift of the BRFL in *x* polarization and *y* polarization varies in the same manner or not. The probability distribution of the relative frequency variation demonstrates the spectral hole burning of the Brillouin gain due to the gain saturation. The relative intensity of the dominating lasing peak of the BRFL is a random variable that follows Gaussian distribution. Internal correlations of the lasing spectrum are analyzed by Pearson correlation coefficient. The characterization of the frequency drifts of the dual-wavelength BRFL has profound implications for its further applications in distributed fiber sensing systems.

7.2 Future work

BRFL exhibits various unique lasing properties in terms of its intensity statistics, mode characteristics and narrow linewidth property. The distributed detection of the acoustic wave in the Brillouin gain fiber explores the internal state of the BRFL. The acoustic wave detection work in the thesis mainly focus on the PM Brillouin gain fiber with large birefringence in a random distributed ring cavity. The properties of the acoustic wave generated by BRFL in single mode fiber have not been explored. Besides, the influence of the pump scheme on the statistical properties of BRFL is also an interesting question to explore the fundamental physics behind BRFL. Furthermore, BRFL shows potential applications in long distance distributed sensing with high precision measurements.

7.2.1 Acoustic wave detection in single mode BRFL

In Chapter 3, the property of the acoustic wave in a PM Brillouin gain fiber is investigated. The intrinsic spectral width and the distributed intensity statistics of the acoustic wave is measured, which reflect the characteristics of the PM BRFL. In BRFL based on a single mode fiber, intensity noise and frequency noise is much higher than the corresponding properties of PM BRFL due to the increased mode number density and the polarization variation of the laser. It is beneficial to detect the acoustic wave in single mode BRFL to further understand the internal working state of the single mode BRFL and its working mechanism. The detection principle of the acoustic wave depends on the local birefringence of the Brillouin gain fiber. Theoretically, the frequency difference between the probe light and the pump light is much smaller than the corresponding frequency difference that is used in the acoustic wave detection in the PM fiber, which requires a more sophisticated method to detect the property of the probe light reflected by the dynamic grating.

7.2.2 Statistical properties of BRFL by bi-directional pump scheme

As illustrated in Chapter 4, the random distributed feedback medium can have a great impact on the output characteristics of the BRFL. However, the influence of the pump scheme on the statistical property of the BRFL still remains unclear. The BRFL can be either generated by a random distributed ring cavity that is studied in the thesis, or by launching the pump source to both ends of the fiber. The light in the ring cavity travels anti-clockwise in one way while the light in the bi-directional pump scheme bounces back and forth continuously by the random frozen scattering centers of the fiber. Compared to the ring cavity based BRFL, the bi-directional pump based BRFL exhibits a larger intensity noise in the low frequency domain due to the intensity noise transfer from the pump source, which could introduce new statistical properties when the output of the BRFL is treated as a complex random system.

7.2.3 Applications of BRFL in distributed sensing

With the improved performance of the BRFL, it shows potential applications in long distance distributed sensing. For example, the dynamic grating detection technique can be used as a distributed simultaneous multi-parameter sensor. Because the spectral response of the dynamic grating and the spectrum of the Brillouin gain show independent linear response to the temperature and pressure variation, both of the parameters can be demodulated by measuring the Brillouin gain spectrum and the spectral response of the dynamic grating. By optimizing the Brillouin gain distribution based on the high order pump scheme of BRFL, a long distance multi-parameter sensor can be realized. At the same time, the narrow linewidth of the BRFL can also be applied to the high precision measurement by using the beat frequency interrogation technique [224]. In this technique, the resolution of the sensor depends on the linewidth of the beat signal so that the sensor based on BRFL are supposed to improve the detection resolution of temperature and pressure.

Publications

- 1. **Zichao Zhou**, Liang Chen, Xiaoyi Bao, "Dynamic detection of acoustic wave generated by polarization maintaining Brillouin random fiber laser" APL Photonics, 2020, 5(9):096101.
- 2. **Zichao Zhou**, Liang Chen, Xiaoyi Bao, "Mode characteristic manipulation of random feedback interferometers in Brillouin random fiber laser" Optics Letters, 2020, 45(3):678-681.
- 3. **Zichao Zhou**, Ping Lu, Liang Zhang et al, "Thermal and acoustic noise insensitive Brillouin random fiber laser based on polarization-maintaining random fiber grating" Optics Letters, 2019, 44(17):4195-4198.
- 4. **Zichao Zhou**, Chen Chen, Ping Lu et al, "Random fiber grating characterization based on OFDR and transfer matrix method" Sensors, 2020 20(21):6071.
- 5. **Zichao Zhou**, Liang Chen, Xiaoyi Bao, "High efficiency Brillouin random fiber laser with replica symmetry breaking enabled by random fiber grating" Optics Express, 2021, 29(5):6352-6541.
- 6. **Zichao Zhou**, Haiyang Wang, Yuan Wang et al, "Distributed static and dynamic detection of acoustic wave in Brillouin random fiber laser" Photonics Research, 2021, 9(5) 772-780.
- 7. Liang Zhang, Ping Lu, **Zichao Zhou** et al, "High-efficiency random fiber laser based on strong random fiber grating for MHz ultrasonic sensing" IEEE Sensors Journal, 2020, 20(11), 5885-5892.

Bibliography

1. R. Ambartsumyan, N. Basov, P. Kryukov, and V. Letokhov, "A laser with a nonresonant feedback," IEEE J. Quantum Electron **2**, 442-446 (1966).

2. V. Letokhov, "Generation of light by a scattering medium with negative resonance absorption," Sov. Phys. JETP **26**, 835-840 (1968).

3. N. M. Lawandy, R. Balachandran, A. Gomes, and E. Sauvain, "Laser action in strongly scattering media," Nature **368**, 436-438 (1994).

4. N. Lawandy, and R. Balachandran, "Random laser?," Nature **373**, 204-204 (1995).

5. D. S. Wiersma, P. Bartolini, A. Lagendijk, and R. Righini, "Localization of light in a disordered medium," Nature **390**, 671-673 (1997).

6. D. S. Wiersma, and A. Lagendijk, "Light diffusion with gain and random lasers," Physical Review E **54**, 4256 (1996).

7. H. Cao, Y. Zhao, S. Ho, E. Seelig, Q. Wang, and R. P. Chang, "Random laser action in semiconductor powder," Physical Review Letters **82**, 2278 (1999).

8. H. Cao, J. Xu, S.-H. Chang, and S. Ho, "Transition from amplified spontaneous emission to laser action in strongly scattering media," Physical Review E **61**, 1985 (2000).

9. H. Cao, Y. Ling, J. Xu, C. Cao, and P. Kumar, "Photon statistics of random lasers with resonant feedback," Physical Review Letters **86**, 4524 (2001).

10. B. Redding, M. A. Choma, and H. Cao, "Spatial coherence of random laser emission," Optics letters **36**, 3404-3406 (2011).

11. B. Redding, M. A. Choma, and H. Cao, "Speckle-free laser imaging using random laser illumination," Nature photonics **6**, 355-359 (2012).

12. N. Bachelard, J. Andreasen, S. Gigan, and P. Sebbah, "Taming random lasers through active spatial control of the pump," Physical review letters **109**, 033903 (2012).

13. H. Kalt, "Towards mode-locking," Nature Photonics **5**, 573-574 (2011).

14. M. Leonetti, C. Conti, and C. Lopez, "The mode-locking transition of random lasers," Nature Photonics **5**, 615-617 (2011).

15. M. Bravo, M. Fernandez-Vallejo, and M. Lopez-Amo, "Internal modulation of a random fiber laser," Optics letters **38**, 1542-1544 (2013).

16. Q. Baudouin, N. Mercadier, V. Guarrera, W. Guerin, and R. Kaiser, "A cold-atom random laser," Nature physics **9**, 357-360 (2013).

17. J. Liu, P. Garcia, S. Ek, N. Gregersen, T. Suhr, M. Schubert, J. Mørk, S. Stobbe, and P. Lodahl, "Random nanolasing in the Anderson localized regime," Nature nanotechnology **9**, 285-289 (2014).

18. K. C. Kao, and G. A. Hockham, "Dielectric-fibre surface waveguides for optical frequencies," in *Proceedings of the Institution of Electrical Engineers*(IET1966), pp. 1151-1158.

19. D. J. Richardson, J. Nilsson, and W. A. Clarkson, "High power fiber lasers: current status and future perspectives," JOSA B **27**, B63-B92 (2010).

20. A. Tünnermann, T. Schreiber, and J. Limpert, "Fiber lasers and amplifiers: an ultrafast performance evolution," Applied optics **49**, F71-F78 (2010).

21. J. Knight, "Photonic crystal fibers and fiber lasers," JOSA B **24**, 1661-1668 (2007).

22. X. Zhu, and N. Peyghambarian, "High-power ZBLAN glass fiber lasers: review and prospect," Advances in OptoElectronics **2010** (2010).

23. P. F. Moulton, G. A. Rines, E. V. Slobodtchikov, K. F. Wall, G. Frith, B. Samson, and A. L. Carter, "Tm-doped fiber lasers: fundamentals and power scaling," IEEE Journal of selected topics in quantum electronics **15**, 85-92 (2009).

24. W. Shi, Q. Fang, X. Zhu, R. A. Norwood, and N. Peyghambarian, "Fiber lasers and their applications," Applied optics **53**, 6554-6568 (2014).

25. C. J. de Matos, L. d. S. Menezes, A. M. Brito-Silva, M. M. Gámez, A. S. Gomes, and C. B. de Araújo, "Random fiber laser," Physical review letters **99**, 153903 (2007).

26. S. K. Turitsyn, S. A. Babin, A. E. El-Taher, P. Harper, D. V. Churkin, S. I. Kablukov, J. D. Ania-Castañón, V. Karalekas, and E. V. Podivilov, "Random distributed feedback fibre laser," Nature Photonics **4**, 231-235 (2010).

27. Z. Hu, Q. Zhang, B. Miao, Q. Fu, G. Zou, Y. Chen, Y. Luo, D. Zhang, P. Wang, and H. Ming, "Coherent random fiber laser based on nanoparticles scattering in the extremely weakly scattering regime," Physical review letters **109**, 253901 (2012).

28. Z. Hu, B. Miao, T. Wang, Q. Fu, D. Zhang, H. Ming, and Q. Zhang, "Disordered microstructure polymer optical fiber for stabilized coherent random fiber laser," Optics letters **38**, 4644-4647 (2013).

29. W. L. Zhang, M. Y. Zheng, R. Ma, C. Y. Gong, Z. J. Yang, G. D. Peng, and Y. J. Rao, "Fiber-type random laser based on a cylindrical waveguide with a disordered cladding layer," Scientific Reports **6**, 26473 (2016).

30. S. Chernikov, Y. Zhu, J. Taylor, and V. Gapontsev, "Supercontinuum self-Q-switched ytterbium fiber laser," Optics letters **22**, 298-300 (1997).

31. A. A. Fotiadi, and P. Mégret, "Self-Q-switched Er-Brillouin fiber source with extra-cavity generation of a Raman supercontinuum in a dispersion-shifted fiber," Optics letters **31**, 1621-1623 (2006).

32. D. Churkin, I. Vatnik, S. Turitsyn, and S. Babin, "Random distributed feedback Raman fiber laser operating in a 1.2 μm wavelength range," Laser Physics **21**, 1525-1529 (2011).

33. I. D. Vatnik, D. V. Churkin, S. A. Babin, and S. K. Turitsyn, "Cascaded random distributed feedback Raman fiber laser operating at 1.2 μm," Optics express **19**, 18486-18494 (2011).

34. X. Wang, D. Chen, H. Li, L. She, and Q. Wu, "Random fiber laser based on artificially controlled backscattering fibers," Applied optics **57**, 258-262 (2018).

35. O. Shapira, and B. Fischer, "Localization of light in a random-grating array in a single-mode fiber," JOSA B **22**, 2542-2552 (2005).

36. Y. Bliokh, E. I. Chaikina, N. Lizárraga, E. R. Méndez, V. Freilikher, and F. Nori, "Disorder-induced cavities, resonances, and lasing in randomly layered media," Physical Review B **86**, 054204 (2012).

37. M. Gagné, and R. Kashyap, "Demonstration of a 3 mW threshold Er-doped random fiber laser based on a unique fiber Bragg grating," Optics express **17**, 19067-19074 (2009).

38. Y. Li, P. Lu, X. Bao, and Z. Ou, "Random spaced index modulation for a narrow linewidth tunable fiber laser with low intensity noise," Optics letters **39**, 2294-2297 (2014).

39. Y. Li, P. Lu, F. Baset, Z. Ou, J. Song, A. Alshehri, V. R. Bhardwaj, and X. Bao, "Narrow linewidth low frequency noise Er-doped fiber ring laser based on femtosecond laser induced random feedback," Applied Physics Letters **105**, 101105 (2014).

40. W. Zhang, R. Ma, C. Tang, Y. Rao, X. Zeng, Z. Yang, Z. Wang, Y. Gong, and Y. Wang, "All optical mode controllable Er-doped random fiber laser with distributed Bragg gratings," Optics letters **40**, 3181-3184 (2015).

41. M. Gagné, and R. Kashyap, "Random fiber Bragg grating Raman fiber laser," Optics letters **39**, 2755-2758 (2014).

42. J. Shi, S.-u. Alam, and M. Ibsen, "Highly efficient Raman distributed feedback fibre lasers," Optics express **20**, 5082-5091 (2012).

43. Z. Guo, J. Song, Y. Liu, Z. Liu, P. Shum, and X. Dong, "Randomly spaced chirped grating-based random fiber laser," Applied Physics B **124**, 48 (2018).

44. M. Skvortsov, S. Abdullina, A. Wolf, A. Dostovalov, A. Vlasov, I. Lobach, S. Wabnitz, and S. Babin, "Random Raman fiber laser based on a twin-core fiber with FBGs inscribed by femtosecond radiation," Optics letters **44**, 295-298 (2019).

45. S. Babin, V. Karalekas, P. Harper, E. Podivilov, V. Mezentsev, J. Ania-Castañón, and S. Turitsyn, "Experimental demonstration of mode structure in ultralong Raman fiber lasers," Optics letters **32**, 1135-1137 (2007).

46. A. Sarmani, M. A. Bakar, A. Bakar, F. M. Adikan, and M. Mahdi, "Spectral variations of the output spectrum in a random distributed feedback Raman fiber laser," Optics express **19**, 14152-14159 (2011).

47. A. El-Taher, M. Alcon-Camas, S. Babin, P. Harper, J. D. Ania-Castanón, and S. K. Turitsyn, "Dual-wavelength, ultralong Raman laser with Rayleigh-scattering feedback," Optics letters **35**, 1100-1102 (2010).

48. A. Pinto, M. Bravo, M. Fernandez-Vallejo, M. Lopez-Amo, J. Kobelke, and K. Schuster, "Suspended-core fiber Sagnac combined dual-random mirror Raman fiber laser," Optics express **19**, 11906-11915 (2011).

49. A. M. R. Pinto, O. Frazão, J. L. Santos, and M. Lopez-Amo, "Multiwavelength Raman fiber lasers using Hi-Bi photonic crystal fiber loop mirrors combined with random cavities," J. Lightwave Technol. **29**, 1482-1488 (2011).

50. A. E. El-Taher, J. D. Ania-Castañón, V. Karalekas, and P. Harper, "High efficiency supercontinuum generation using ultra-long Raman fiber cavities," Optics express **17**, 17909-17915 (2009).

51. S. Babin, A. El-Taher, P. Harper, E. Podivilov, and S. Turitsyn, "Tunable random fiber laser," Physical Review A **84**, 021805 (2011).

52. X. Du, H. Zhang, X. Wang, and P. Zhou, "Tunable random distributed feedback fiber laser operating at 1 μm," Applied optics **54**, 908-911 (2015).

53. D. V. Churkin, S. Sugavanam, I. D. Vatnik, Z. Wang, E. V. Podivilov, S. A. Babin, Y. Rao, and S. K. Turitsyn, "Recent advances in fundamentals and applications of random fiber lasers," Advances in Optics and Photonics **7**, 516 (2015).

54. A. A. Fotiadi, and R. V. Kiyan, "Cooperative stimulated Brillouin and Rayleigh backscattering process in optical fiber," Optics letters **23**, 1805-1807 (1998).

55. M. Pang, S. Xie, X. Bao, D.-P. Zhou, Y. Lu, and L. Chen, "Rayleigh scattering-assisted narrow linewidth Brillouin lasing in cascaded fiber," Optics letters **37**, 3129-3131 (2012).

56. M. Pang, X. Bao, and L. Chen, "Observation of narrow linewidth spikes in the coherent Brillouin random fiber laser," Optics letters **38**, 1866-1868 (2013).

57. M. Pang, X. Bao, L. Chen, Z. Qin, Y. Lu, and P. Lu, "Frequency stabilized coherent Brillouin random fiber laser: theory and experiments," Optics express **21**, 27155-27168 (2013).

58. L. Zhang, C. Wang, Z. Li, Y. Xu, B. Saxena, S. Gao, L. Chen, and X. Bao, "High-efficiency Brillouin random fiber laser using all-polarization maintaining ring cavity," Optics express **25**, 11306-11314 (2017).

59. L. Zhang, Y. Xu, S. Gao, B. Saxena, L. Chen, and X. Bao, "Linearly polarized low-noise Brillouin random fiber laser," Optics letters **42**, 739-742 (2017).

60. L. Zhang, Y. Xu, S. Gao, B. Saxena, L. Chen, and X. Bao, "Multiwavelength Coherent Brillouin Random Fiber Laser With Ultrahigh Optical Signal-to-Noise Ratio," IEEE Journal of Selected Topics in Quantum Electronics **24**, 1-8 (2018).

61. L. Zhang, Y. Xu, P. Lu, S. Mihailov, L. Chen, and X. Bao, "Multi-Wavelength Brillouin Random Fiber Laser via Distributed Feedback From a Random Fiber Grating," J. Lightwave Technol. **36**, 2122-2128 (2018).

62. T. Zhu, X. Bao, and L. Chen, "A single longitudinal-mode tunable fiber ring laser based on stimulated Rayleigh scattering in a nonuniform optical fiber," J. Lightwave Technol. **29**, 1802-1807 (2011).

63. G. Yin, B. Saxena, and X. Bao, "Tunable Er-doped fiber ring laser with single longitudinal mode operation based on Rayleigh backscattering in single mode fiber," Optics express **19**, 25981-25989 (2011).

64. B. Saxena, X. Bao, and L. Chen, "Suppression of thermal frequency noise in erbium-doped fiber random lasers," Optics letters **39**, 1038-1041 (2014).

65. L. Wang, X. Dong, P. P. Shum, and H. Su, "Tunable erbium-doped fiber laser based on random distributed feedback," IEEE Photonics Journal **6**, 1-5 (2014).

66. L. Wang, X. Dong, P. P. Shum, C. Huang, and H. Su, "Erbium-doped fiber laser with distributed Rayleigh output mirror," Laser Physics **24**, 115101 (2014).

67. N. Lizárraga, N. Puente, E. Chaikina, T. Leskova, and E. Méndez, "Single-mode Er-doped fiber random laser with distributed Bragg grating feedback," Optics express **17**, 395-404 (2009).

68. B. Hu, W. Zhang, R. Ma, J. Guo, A. Ludwig, and Y. Rao, "Wavelength locking of Er-doped random fiber laser," Laser Physics Letters **16**, 055102 (2019).

69. I. A. Lobach, S. I. Kablukov, M. I. Skvortsov, E. V. Podivilov, M. A. Melkumov, S. A. Babin, and E. M. Dianov, "Narrowband random lasing in a Bismuth-doped active fiber," Scientific reports **6**, 30083 (2016).

70. Y. Tang, and J. Xu, "A random Q-switched fiber laser," Scientific Reports **5**, 1-5 (2015).

71. M. A. Bakar, F. M. Adikan, and M. Mahdi, "Rayleigh-based Raman fiber laser with passive erbium-doped fiber for secondary pumping effect in remote L-band erbium-doped fiber amplifier," IEEE Photonics Journal **4**, 1042-1050 (2012).

72. Z. Wang, H. Wu, M. Fan, Y. Li, Y. Gong, and Y. Rao, "Broadband flat-amplitude multiwavelength Brillouin-Raman fiber laser with spectral reshaping by Rayleigh scattering," Optics express **21**, 29358-29363 (2013).

73. H. Wu, Z. Wang, X. Jia, P. Li, M. Fan, Y. Li, and Y. Zhu, "Flat amplitude multiwavelength Brillouin–Raman random fiber laser with a half-open cavity," Applied Physics B **112**, 467-471 (2013).

74. C. Huang, X. Dong, S. Zhang, N. Zhang, and P. P. Shum, "Cascaded random fiber laser based on hybrid Brillouin-erbium fiber gains," IEEE Photonics Technology Letters **26**, 1287-1290 (2014).

75. W. L. Zhang, S. W. Li, R. Ma, Y. J. Rao, Y. Y. Zhu, Z. N. Wang, X. H. Jia, and J. Li, "Random distributed feedback fiber laser based on combination of Er-doped fiber and single-mode fiber," IEEE Journal of Selected Topics in Quantum Electronics **21**, 44-49 (2014).

76. N. Z. Abidin, M. A. Bakar, Y. M. Kamil, A. F. Abas, M. T. Alresheedi, and M. A. Mahdi, "Open Cavity Hybrid Raman-Erbium Random Fiber Laser With Common Pump," IEEE Access **7**, 85867-85874 (2019).

77. Z. Wang, H. Wu, M. Fan, Y. Rao, I. Vatnik, E. Podivilov, S. Babin, D. Churkin, H. Zhang, and P. Zhou, "Random fiber laser: simpler and brighter," Opt. Photon. News **25**, 30 (2014).

78. I. D. Vatnik, D. V. Churkin, and S. A. Babin, "Power optimization of random distributed feedback fiber lasers," Optics express **20**, 28033-28038 (2012).

79. D. V. Churkin, A. E. El-Taher, I. D. Vatnik, J. D. Ania-Castañón, P. Harper, E. V. Podivilov, S. A. Babin, and S. K. Turitsyn, "Experimental and theoretical study of longitudinal power distribution in a random DFB fiber laser," Optics express **20**, 11178-11188 (2012).

80. S. Lin, Z. Wang, H. A. Araújo, E. P. Raposo, A. S. Gomes, H. Wu, M. Fan, and Y. Rao, "Ultrafast convergent power-balance model for Raman random fiber laser with half-open cavity," Optics express **28**, 22500-22510 (2020).

81. I. Vatnik, D. Churkin, E. V. Podivilov, and S. A. Babin, "High-efficiency generation in a short random fiber laser," Laser Physics Letters **11**, 075101 (2014).

82. H. Zhang, P. Zhou, H. Xiao, and X. Xu, "Efficient Raman fiber laser based on random Rayleigh distributed feedback with record high power," Laser Physics Letters **11**, 075104 (2014).

83. S. A. Babin, E. A. Zlobina, S. I. Kablukov, and E. V. Podivilov, "High-order random Raman lasing in a PM fiber with ultimate efficiency and narrow bandwidth," Scientific reports **6**, 22625 (2016).

84. X. Du, H. Zhang, X. Wang, P. Zhou, and Z. Liu, "Short cavity-length random fiber laser with record power and ultrahigh efficiency," Optics letters **41**, 571-574 (2016).

85. Z. Wang, H. Wu, M. Fan, L. Zhang, Y. Rao, W. Zhang, and X. Jia, "High power random fiber laser with short cavity length: theoretical and experimental investigations," IEEE Journal of Selected Topics in Quantum Electronics **21**, 10-15 (2014).

86. H. Zhang, L. Huang, P. Zhou, X. Wang, J. Xu, and X. Xu, "More than 400 W random fiber laser with excellent beam quality," Optics letters **42**, 3347-3350 (2017).

87. H. Zhang, J. Ye, P. Zhou, X. Wang, J. Leng, J. Xu, J. Wu, and X. Xu, "Tapered-fiber-enabled high-power, high-spectral-purity random fiber lasing," Optics letters **43**, 4152-4155 (2018).

88. J. Ye, J. Xu, J. Song, H. Xu, H. Wu, H. Zhang, J. Leng, and P. Zhou, "Power scalability of linearly polarized random fiber laser through polarization-rotation-based Raman gain manipulation," Optics express **26**, 22894-22903 (2018).

89. H. Zhang, L. Huang, J. Song, H. Wu, P. Zhou, X. Wang, J. Wu, J. Xu, Z. Wang, and X. Xu, "Quasi-kilowatt random fiber laser," Optics letters **44**, 2613-2616 (2019).

90. Z. Wang, P. Yan, Y. Huang, J. Tian, C. Cai, D. Li, Y. Yi, Q. Xiao, and M. Gong, "An efficient 4-kW level random fiber laser based on a tandem-pumping scheme," IEEE Photonics Technology Letters **31**, 817-820 (2019).

91. S. A. Babin, E. Dontsova, and S. Kablukov, "Random fiber laser directly pumped by a high-power laser diode," Optics letters **38**, 3301-3303 (2013).

92. S. Kablukov, E. Dontsova, E. Zlobina, I. Nemov, A. Vlasov, and S. Babin, "An LD-pumped Raman fiber laser operating below 1 μm," Laser Physics Letters **10**, 085103 (2013).

93. E. A. Evmenova, A. G. Kuznetsov, I. N. Nemov, A. A. Wolf, A. V. Dostovalov, S. I. Kablukov, and S. A. Babin, "2nd-order random lasing in a multimode diode-pumped graded-index fiber," Scientific Reports **8**, 1-7 (2018).

94. H. Zhang, H. Xiao, P. Zhou, X. Wang, and X. Xu, "Random distributed feedback Raman fiber laser with short cavity and its temporal properties," IEEE Photonics Technology Letters **26**, 1605-1608 (2014).

95. S. V. Smirnov, and D. V. Churkin, "Modeling of spectral and statistical properties of a random distributed feedback fiber laser," Optics express **21**, 21236-21241 (2013).

96. O. A. Gorbunov, S. Sugavanam, and D. V. Churkin, "Intensity dynamics and statistical properties of random distributed feedback fiber laser," Optics letters **40**, 1783-1786 (2015).

97. D. R. Solli, C. Ropers, P. Koonath, and B. Jalali, "Optical rogue waves," Nature **450**, 1054-1057 (2007).

98. J. Xu, J. Wu, J. Ye, J. Song, B. Yao, H. Zhang, J. Leng, W. Zhang, P. Zhou, and Y. Rao, "Optical rogue wave in random fiber laser," Photonics Research **8**, 1-7 (2020).

99. D. V. Churkin, S. V. Smirnov, and E. V. Podivilov, "Statistical properties of partially coherent cw fiber lasers," Optics letters **35**, 3288-3290 (2010).

100. S. Randoux, N. Dalloz, and P. Suret, "Intracavity changes in the field statistics of Raman fiber lasers," Optics letters **36**, 790-792 (2011).

101. B. C. Lima, P. I. Pincheira, E. P. Raposo, L. d. S. Menezes, C. B. de Araújo, A. S. Gomes, and R. Kashyap, "Extreme-value statistics of intensities in a cw-pumped random fiber laser," Physical Review A **96**, 013834 (2017).

102. L. Ogorodnikov, and S. Vergeles, "Intensity statistics in a long random fiber Raman laser," Optics letters **43**, 651-654 (2018).

103. B. C. Lima, A. S. Gomes, P. I. Pincheira, A. L. Moura, M. Gagné, E. P. Raposo, C. B. de Araújo, and R. Kashyap, "Observation of Lévy statistics in one-dimensional erbium-based random fiber laser," JOSA B **34**, 293-299 (2017).

104. J. Li, H. Wu, Z. Wang, S. Lin, C. Lu, E. P. Raposo, A. S. Gomes, and Y. Rao, "Lévy spectral intensity statistics in a Raman random fiber laser," Optics letters **44**, 2799-2802 (2019).

105. I. R. R. Gonzalez, B. C. Lima, P. I. Pincheira, A. A. Brum, A. M. Macedo, G. L. Vasconcelos, L. d. S. Menezes, E. P. Raposo, A. S. Gomes, and R. Kashyap, "Turbulence hierarchy in a random fibre laser," Nature Communications **8**, 1-8 (2017).

106. A. S. Gomes, B. C. Lima, P. I. Pincheira, A. L. Moura, M. Gagné, E. P. Raposo, C. B. de Araújo, and R. Kashyap, "Glassy behavior in a one-dimensional continuous-wave erbium-doped random fiber laser," Physical Review A **94**, 011801 (2016).

107. A. Tehranchi, V. L. Iezzi, and R. Kashyap, "Power fluctuations and random lasing in multiwavelength Brillouin erbium-doped fiber lasers," J. Lightwave Technol. **37**, 4439-4444 (2019).

108. J. Nuño, M. Alcon-Camas, and J. D. Ania-Castañón, "RIN transfer in random distributed feedback fiber lasers," Optics express **20**, 27376-27381 (2012).

109. S. Rota-Rodrigo, G. Rizzelli, D. Leandro, J. Nuño, M. Lopez-Amo, G. Santarelli, and J. D. Ania-Castañón, "Anomalous relative intensity noise transfer in ultralong random fiber lasers," Optics express **28**, 28234-28242 (2020).

110. Y. Xu, S. Gao, P. Lu, S. Mihailov, L. Chen, and X. Bao, "Low-noise Brillouin random fiber laser with a random grating-based resonator," Optics letters **41**, 3197-3200 (2016).

111. Y. Xu, P. Lu, and X. Bao, "Compact single-end pumped Brillouin random fiber laser with enhanced distributed feedback," Optics letters **45**, 4236-4239 (2020).

112. B. Yao, Y. Rao, Z. Wang, Y. Wu, J. Zhou, H. Wu, M. Fan, X. Cao, W. Zhang, and Y. Chen, "Graphene based widely-tunable and singly-polarized pulse generation with random fiber lasers," Scientific reports **5**, 18526 (2015).

113. A. Kuznetsov, E. Podivilov, and S. Babin, "Actively Q-switched Raman fiber laser," Laser Physics Letters **12**, 035102 (2015).

114. J. Xu, J. Ye, H. Xiao, J. Leng, J. Wu, H. Zhang, and P. Zhou, "Narrow-linewidth Q-switched random distributed feedback fiber laser," Optics express **24**, 19203-19210 (2016).

115. J. Xu, J. Ye, W. Liu, J. Wu, H. Zhang, J. Leng, and P. Zhou, "Passively spatiotemporal gain-modulation-induced stable pulsing operation of a random fiber laser," Photonics Research **5**, 598-603 (2017).

116. B. Hu, H. Cui, Y. L. Zhang, R. Ma, Y. C. Xiao, P. F. Qu, and W. L. Zhang, "Mode locking of a coherent random fiber laser with selectable repetition rates," Optics express **28**, 36380-36388 (2020).

117. I. D. Vatnik, D. V. Churkin, and S. A. Babin, "Spectral width optimization in random DFB fiber laser," in *The European Conference on Lasers and Electro-Optics*(Optical Society of America2013), p. CJ_P_19.

118. I. Vatnik, E. Zlobina, S. Kablukov, and S. Babin, "Multi-peak structure of generation spectrum of random distributed feedback fiber Raman lasers," Optics express **25**, 2703-2708 (2017).

119. D. V. Churkin, I. V. Kolokolov, E. V. Podivilov, I. D. Vatnik, M. A. Nikulin, S. S. Vergeles, I. S. Terekhov, V. V. Lebedev, G. Falkovich, and S. A. Babin, "Wave kinetics of random fibre lasers," Nature communications **6**, 1-6 (2015).

120. S. Sugavanam, M. Sorokina, and D. V. Churkin, "Spectral correlations in a random distributed feedback fibre laser," Nature communications **8**, 1-8 (2017).

121. J. Ye, Y. Zhang, J. Xu, J. Song, T. Yao, H. Xiao, J. Leng, and P. Zhou, "Investigations on the extreme frequency shift of phosphosilicate random fiber laser," J. Lightwave Technol. (2020).

122. I. Vatnik, O. Gorbunov, S. Sugavanam, D. Churkin, and E. Podivilov, "Spatial location of correlations in a random distributed feedback Raman fiber laser," Optics letters **44**, 1516-1519 (2019).

123. Y. Bliokh, E. Chaikina, I. Vatnik, and D. Churkin, "Temporal variation of the spectrum of a continuously pumped random fiber laser: phenomenological model," JOSA B **36**, 408-414 (2019).

124. S. Sugavanam, N. Tarasov, X. Shu, and D. V. Churkin, "Narrow-band generation in random distributed feedback fiber laser," Optics express **21**, 16466-16472 (2013).

125. B. Saxena, Z. Ou, X. Bao, and L. Chen, "Low frequency-noise random fiber laser with bidirectional SBS and Rayleigh feedback," IEEE Photonics Technology Letters **27**, 490-493 (2014).

126. S. Gao, L. Zhang, Y. Xu, P. Lu, L. Chen, and X. Bao, "Tapered fiber based Brillouin random fiber laser and its application for linewidth measurement," Optics express **24**, 28353-28360 (2016).

127. L. Zhang, H. Jiang, X. Yang, W. Pan, and Y. Feng, "Ultra-wide wavelength tuning of a cascaded Raman random fiber laser," Optics letters **41**, 215-218 (2016).

128. Y. Zhang, J. Song, J. Ye, J. Xu, T. Yao, and P. Zhou, "Tunable random Raman fiber laser at 1.7 μm region with high spectral purity," Optics express **27**, 28800-28807 (2019).

129. J. Ye, J. Xu, J. Song, Y. Zhang, H. Zhang, H. Xiao, J. Leng, and P. Zhou, "Pump scheme optimization of an incoherently pumped high-power random fiber laser," Photonics Research **7**, 977-983 (2019).

130. A. E. El-Taher, P. Harper, S. Babin, D. Churkin, E. Podivilov, J. D. Ania-Castanon, and S. Turitsyn, "Effect of Rayleigh-scattering distributed feedback on multiwavelength Raman fiber laser generation," Optics letters **36**, 130-132 (2011).

131. S. Sugavanam, Z. Yan, V. Kamynin, A. Kurkov, L. Zhang, and D. Churkin, "Multiwavelength generation in a random distributed feedback fiber laser using an all fiber Lyot filter," Optics express **22**, 2839-2844 (2014).

132. O. Gorbunov, S. Sugavanam, I. Vatnik, and D. Churkin, "Statistical properties of radiation of multiwavelength random DFB fiber laser," Optics express **24**, 19417-19423 (2016).

133. A. Pinto, O. Frazão, J. Santos, and M. Lopez-Amo, "Multiwavelength fiber laser based on a photonic crystal fiber loop mirror with cooperative Rayleigh scattering," Applied Physics B **99**, 391-395 (2010).

134. N. M. Yusoff, K. Lau, N. Z. Abidin, Y. M. Kamil, A. Sarmani, and M. Mahdi, "Dual-wavelength random fiber laser incorporating micro-air cavity," Journal of Optics **22**, 035603 (2020).

135. J. Ye, Y. Zhang, J. Xu, J. Song, T. Yao, H. Xiao, J. Leng, and P. Zhou, "Broadband pumping enabled flat-amplitude multi-wavelength random Raman fiber laser," Optics letters **45**, 1786-1789 (2020).

136. Y. Y. Zhu, W. L. Zhang, and Y. Jiang, "Tunable multi-wavelength fiber laser based on random Rayleigh back-scattering," IEEE Photonics Technology Letters **25**, 1559-1561 (2013).

137. V. DeMiguel-Soto, M. Bravo, and M. Lopez-Amo, "Fully switchable multiwavelength fiber laser assisted by a random mirror," Optics letters **39**, 2020-2023 (2014).

138. P. Huang, X. Shu, and Z. Zhang, "Multi-wavelength random fiber laser with switchable wavelength interval," Optics express **28**, 28686-28695 (2020).

139. R. Ma, W. L. Zhang, S. S. Wang, X. Zeng, H. Wu, and Y. J. Rao, "Simultaneous generation of random lasing and supercontinuum in a completely-opened fiber structure," Laser Physics Letters **15**, 085111 (2018).

140. L. Chen, R. Song, C. Lei, W. Yang, F. He, and J. Hou, "Influences of position of ytterbium-doped fiber and ASE pump on spectral properties of random fiber laser," Optics express **27**, 9647-9654 (2019).

141. R. Ma, Y. J. Rao, W. L. Zhang, X. Zeng, X. Dong, H. Wu, Z. N. Wang, and X. P. Zeng, "Backward supercontinuum generation excited by random lasing," IEEE Journal of Selected Topics in Quantum Electronics **24**, 1-5 (2017).

142. Z. Wang, Y. Rao, H. Wu, P. Li, Y. Jiang, X. Jia, and W. Zhang, "Long-distance fiber-optic point-sensing systems based on random fiber lasers," Optics express **20**, 17695-17700 (2012).

143. M. Fernandez-Vallejo, M. Bravo, and M. Lopez-Amo, "Ultra-long laser systems for remote fiber Bragg gratings arrays interrogation," IEEE Photonics Technology Letters **25**, 1362-1364 (2013).

144. D. Leandro, V. d. Soto, R. A. Perez-Herrera, M. B. Acha, and M. López-Amo, "Random DFB fiber laser for remote (200 km) sensor monitoring using hybrid WDM/TDM," J. Lightwave Technol. **34**, 4430-4436 (2016).

145. Z. Wang, W. Sun, H. Wu, X. Qian, Q. He, Z. Wei, and Y. Rao, "Long-distance random fiber laser point sensing system incorporating active fiber," Optics express **24**, 22448-22453 (2016).

146. H. Martins, M. Marques, and O. Frazão, "Temperature-insensitive strain sensor based on four-wave mixing using Raman fiber Bragg grating laser sensor with cooperative Rayleigh scattering," Applied Physics B **104**, 957-960 (2011).

147. D. Leandro, V. deMiguel-Soto, and M. López-Amo, "High-resolution sensor system using a random distributed feedback fiber laser," J. Lightwave Technol. **34**, 4596-4602 (2016).

148. P. Liu, W. Huang, W. Zhang, and F. Li, "Ultrahigh resolution optic fiber strain sensor with a frequency-locked random distributed feedback fiber laser," Optics letters **43**, 2499-2502 (2018).

149. A. M. R. Pinto, M. Lopez-Amo, J. Kobelke, and K. Schuster, "Temperature fiber laser sensor based on a hybrid cavity and a random mirror," J. Lightwave Technol. **30**, 1168-1172 (2011).

150. Y. Xu, L. Zhang, S. Gao, P. Lu, S. Mihailov, and X. Bao, "Highly sensitive fiber random-grating-based random laser sensor for ultrasound detection," Optics letters **42**, 1353-1356 (2017).

151. L. Zhang, P. Lu, Z. Zhou, Y. Wang, S. Mihailov, L. Chen, and X. Bao, "High-Efficiency Random Fiber Laser Based on Strong Random Fiber Grating for MHz Ultrasonic Sensing," IEEE Sensors Journal **20**, 5885-5892 (2020).

152. S. Miao, W. Zhang, W. Huang, and Y. Song, "High-Resolution Static Strain Sensor Based on Random Fiber Laser and Beat Frequency Interrogation," IEEE Photonics Technology Letters **31**, 1530-1533 (2019).

153. X.-H. Jia, Y.-J. Rao, F. Peng, Z.-N. Wang, W.-L. Zhang, H.-J. Wu, and Y. Jiang, "Random-lasing-based distributed fiber-optic amplification," Optics express **21**, 6572-6577 (2013).

154. M. Tan, P. Rosa, S. Le, M. A. Iqbal, I. Phillips, and P. Harper, "Transmission performance improvement using random DFB laser based Raman amplification and bidirectional second-order pumping," Optics express **24**, 2215-2221 (2016).

155. X.-H. Jia, Y.-J. Rao, C.-X. Yuan, J. Li, X.-D. Yan, Z.-N. Wang, W.-L. Zhang, H. Wu, Y.-Y. Zhu, and F. Peng, "Hybrid distributed Raman amplification combining random fiber laser based 2nd-order and low-noise LD based 1st-order pumping," Optics express **21**, 24611-24619 (2013).

156. Y. Fu, R. Zhu, B. Han, H. Wu, Y.-J. Rao, C. Lu, and Z. Wang, "175-km Repeaterless BOTDA With Hybrid High-Order Random Fiber Laser Amplification," J. Lightwave Technol. **37**, 4680-4686 (2019).

157. Y. Xu, P. Lu, S. Mihailov, and X. Bao, "Real-time physical random bit generation at Gbps based on random fiber lasers," Optics letters **42**, 4796-4799 (2017).

158. D. Xiang, P. Lu, Y. Xu, S. Gao, L. Chen, and X. Bao, "Truly random bit generation based on a novel random Brillouin fiber laser," Optics letters **40**, 5415-5418 (2015).

159. S. Gao, L. Zhang, Y. Xu, L. Chen, and X. Bao, "High-speed random bit generation via brillouin random fiber laser with non-uniform fibers," IEEE Photonics Technology Letters **29**, 1352-1355 (2017).

160. H. Wu, B. Han, Z. Wang, G. Genty, G. Feng, and H. Liang, "Temporal ghost imaging with random fiber lasers," Optics express **28**, 9957-9964 (2020).

161. D. Xiang, P. Lu, Y. Xu, L. Chen, and X. Bao, "Random Brillouin fiber laser for tunable ultra-narrow linewidth microwave generation," Optics letters **41**, 4839-4842 (2016).

162. Y. Xu, D. Xiang, Z. Ou, P. Lu, and X. Bao, "Random Fabry–Perot resonator-based sub-kHz Brillouin fiber laser to improve spectral resolution in linewidth measurement," Optics letters **40**, 1920-1923 (2015).

163. R. Ma, J. Q. Li, J. Y. Guo, H. Wu, H. H. Zhang, B. Hu, Y. J. Rao, and W. L. Zhang, "High-power low spatial coherence random fiber laser," Optics express **27**, 8738-8744 (2019).

164. R. Ma, J. Li, J. Guo, H. Wu, H. Zhang, B. Hu, Y. Rao, and W. Zhang, "High-power multi transverse modes random fiber laser with considerably low spatial coherence," in *CLEO: Science and Innovations*(Optical Society of America2019), p. STh3L. 1.

165. J. Lv, H. Li, Y. Zhang, R. Tao, Z. Dong, C. Gu, P. Yao, Y. Zhu, W. Chen, and Q. Zhan, "Few-mode random fiber laser with a switchable oscillating spatial mode," Optics express **28**, 38973-38982 (2020).

166. R. Ma, Y. J. Rao, W. L. Zhang, and B. Hu, "Multimode random fiber laser for speckle-free imaging," IEEE Journal of Selected Topics in Quantum Electronics **25**, 1-6 (2018).

167. R. W. Boyd, *Nonlinear Optics* (2003).

168. M. Berry, and S. Klein, "Transparent mirrors: rays, waves and localization," European Journal of Physics **18**, 222 (1997).

169. T. Yoshino, "Simple theoretical approach for spectral properties of Rayleigh backscattering feedback fibre lasers," Electronics letters **47**, 1040-1042 (2011).

170. S. Foster, A. Tikhomirov, and M. Milnes, "Fundamental thermal noise in distributed feedback fiber lasers," IEEE journal of quantum electronics **43**, 378-384 (2007).

171. S. Foster, "Fundamental limits on 1/f frequency noise in rare-earth-metal-doped fiber lasers due to spontaneous emission," Physical Review A **78**, 013820 (2008).

172. S. K. Turitsyn, S. A. Babin, D. V. Churkin, I. D. Vatnik, M. Nikulin, and E. V. Podivilov, "Random distributed feedback fibre lasers," Physics Reports **542**, 133-193 (2014).

173. T. Okoshi, K. Kikuchi, and A. Nakayama, "Novel method for high resolution measurement of laser output spectrum," Electronics letters **16**, 630-631 (1980).

174. L. Richter, H. Mandelberg, M. Kruger, and P. McGrath, "Linewidth determination from self-heterodyne measurements with subcoherence delay times," IEEE Journal of Quantum Electronics **22**, 2070-2074 (1986).

175. P. Gallion, and G. Debarge, "Quantum phase noise and field correlation in single frequency semiconductor laser systems," IEEE Journal of Quantum Electronics **20**, 343-349 (1984).

176. S. K. Sheem, "Optical fiber interferometers with [3× 3] directional couplers: Analysis," Journal of Applied Physics **52**, 3865-3872 (1981).

177. C. Wang, Y. Shang, X.-H. Liu, C. Wang, H.-H. Yu, D.-S. Jiang, and G.-D. Peng, "Distributed OTDR-interferometric sensing network with identical ultra-weak fiber Bragg gratings," Optics express **23**, 29038-29046 (2015).

178. E. Turitsyna, S. Smirnov, S. Sugavanam, N. Tarasov, X. Shu, S. Babin, E. Podivilov, D. Churkin, G. Falkovich, and S. Turitsyn, "The laminar–turbulent transition in a fibre laser," Nature Photonics **7**, 783-786 (2013).

179. A. Debut, S. Randoux, and J. Zemmouri, "Experimental and theoretical study of linewidth narrowing in Brillouin fiber ring lasers," JOSA B **18**, 556-567 (2001).

180. I. A. Lobach, R. V. Drobyshev, A. A. Fotiadi, E. V. Podivilov, S. I. Kablukov, and S. A. Babin, "Open-cavity fiber laser with distributed feedback based on externally or self-induced dynamic gratings," Optics letters **42**, 4207-4210 (2017).

181. K. Y. Song, W. Zou, Z. He, and K. Hotate, "All-optical dynamic grating generation based on Brillouin scattering in polarization-maintaining fiber," Optics letters **33**, 926-928 (2008).

182. Y. Dong, L. Chen, and X. Bao, "Characterization of the Brillouin grating spectra in a polarization-maintaining fiber," Optics express **18**, 18960-18967 (2010).

183. K. Y. Song, and H. J. Yoon, "Observation of narrowband intrinsic spectra of Brillouin dynamic gratings," Optics letters **35**, 2958-2960 (2010).

184. D.-P. Zhou, Y. Dong, L. Chen, and X. Bao, "Four-wave mixing analysis of Brillouin dynamic grating in a polarization-maintaining fiber: theory and experiment," Optics express **19**, 20785-20798 (2011).

185. D.-P. Zhou, L. Chen, and X. Bao, "Polarization-decoupled four-wave mixing based on stimulated Brillouin scattering in a polarization-maintaining fiber," JOSA B **30**, 821-828 (2013).

186. H. Lee, T. Chen, J. Li, K. Y. Yang, S. Jeon, O. Painter, and K. J. Vahala, "Chemically etched ultrahigh-Q wedge-resonator on a silicon chip," Nature Photonics **6**, 369-373 (2012).

187. Z. Zhou, L. Chen, and X. Bao, "Mode characteristic manipulation of random feedback interferometers in Brillouin random fiber laser," Optics letters **45**, 678-681 (2020).

188. B. J. Soller, D. K. Gifford, M. S. Wolfe, and M. E. Froggatt, "High resolution optical frequency domain reflectometry for characterization of components and assemblies," Optics express **13**, 666-674 (2005).

189. Z. Lou, B. Yang, K. Han, X. Wang, H. Zhang, X. Xi, and Z. Liu, "Real-time in-situ distributed fiber core temperature measurement in hundred-watt fiber laser oscillator pumped by 915/976 nm LD sources," Scientific Reports **10**, 1-8 (2020).

190. K. Y. Song, "High-sensitivity optical time-domain reflectometry based on Brillouin dynamic gratings in polarization maintaining fibers," Optics express **20**, 27377-27383 (2012).

191. Y. H. Kim, and K. Y. Song, "Optical time-domain reflectometry based on a Brillouin dynamic grating in an elliptical-core two-mode fiber," Optics letters **42**, 3036-3039 (2017).

192. Z. Zhou, H. Wang, Y. Wang, L. Chen, and X. Bao, "Distributed static and dynamic detection of an acoustic wave in a Brillouin random fiber laser," Photonics Research **9**, 772-780 (2021).

193. Z. Zhou, P. Lu, L. Zhang, S. Mihailov, L. Chen, and X. Bao, "Thermal and acoustic noise insensitive Brillouin random fiber laser based on polarization-maintaining random fiber grating," Optics letters **44**, 4195-4198 (2019).

194. J. M. Dudley, F. Dias, M. Erkintalo, and G. Genty, "Instabilities, breathers and rogue waves in optics," Nature Photonics **8**, 755-764 (2014).

195. E. J. Kelleher, J. C. Travers, S. V. Popov, and J. R. Taylor, "Role of pump coherence in the evolution of continuous-wave supercontinuum generation initiated by modulation instability," JOSA B **29**, 502-512 (2012).

196. Z. Zhou, L. Chen, and X. Bao, "Dynamic detection of acoustic wave generated by polarization maintaining Brillouin random fiber laser," APL Photonics **5**, 096101 (2020).

197. J. Deng, M. Han, Z. Xu, Y. Du, and X. Shu, "Stable and low-threshold random fiber laser via Anderson localization," Optics express **27**, 12987-12997 (2019).

198. P. Lu, S. J. Mihailov, D. Coulas, H. Ding, and X. Bao, "Low-loss random fiber gratings made with an fs-IR laser for distributed fiber sensing," J. Lightwave Technol. **37**, 4697-4702 (2019).

199. L. Huang, J. Xu, J. Ye, X. Liu, H. Zhang, X. Wang, and P. Zhou, "Power scaling of linearly polarized random fiber laser," IEEE Journal of Selected Topics in Quantum Electronics **24**, 1-8 (2017).

200. S. Sugavanam, S. Fabbri, S. T. Le, I. Lobach, S. Kablukov, S. Khorev, and D. Churkin, "Real-time high-resolution heterodyne-based measurements of spectral dynamics in fibre lasers," Scientific reports **6**, 1-8 (2016).

201. I. Bar-Joseph, A. Dienes, A. Friesem, E. Lichtman, R. Waarts, and H. Yaffe, "Spontaneous mode locking of single and multi mode pumped SBS fiber lasers," Optics communications **59**, 296-298 (1986).

202. C. Montes, D. Bahloul, I. Bongrand, J. Botineau, G. Cheval, A. Mamhoud, E. Picholle, and A. Picozzi, "Self-pulsing and dynamic bistability in cw-pumped Brillouin fiber ring lasers," JOSA B **16**, 932-951 (1999).

203. R. Gabet, P. Hamel, Y. Jaouën, A.-F. Obaton, V. Lanticq, and G. Debarge, "Versatile characterization of specialty fibers using the phase-sensitive optical low-coherence reflectometry technique," J. Lightwave Technol. **27**, 3021-3033 (2009).

204. A.-F. Obaton, C. Palavicini, Y. Jaouenjaouen, E. Kerrinckx, Y. Quiquempois, and M. Lievrelievre, "Characterization of fiber Bragg gratings by phase-sensitive optical low-coherence reflectometry," IEEE transactions on instrumentation and measurement **55**, 1696-1703 (2006).

205. N. M. Israelsen, C. R. Petersen, A. Barh, D. Jain, M. Jensen, G. Hannesschläger, P. Tidemand-Lichtenberg, C. Pedersen, A. Podoleanu, and O. Bang, "Real-time high-resolution mid-infrared optical coherence tomography," Light: Science & Applications **8**, 1-13 (2019).

206. Z. Zhou, C. Chen, P. Lu, S. Mihailov, L. Chen, and X. Bao, "Random Fiber Grating Characterization Based on OFDR and Transfer Matrix Method," Sensors **20**, 6071 (2020).

207. N. Ghofraniha, I. Viola, F. Di Maria, G. Barbarella, G. Gigli, L. Leuzzi, and C. Conti, "Experimental evidence of replica symmetry breaking in random lasers," Nature communications **6**, 1-8 (2015).

208. F. Antenucci, A. Crisanti, and L. Leuzzi, "The glassy random laser: replica symmetry breaking in the intensity fluctuations of emission spectra," Scientific reports **5**, 1-11 (2015).

209. Z. Zhou, L. Chen, and X. Bao, "High efficiency Brillouin random fiber laser with replica symmetry breaking enabled by random fiber grating," Optics express **29**, 6532-6541 (2021).

210. R. Drever, J. L. Hall, F. Kowalski, J. Hough, G. Ford, A. Munley, and H. Ward, "Laser phase and frequency stabilization using an optical resonator," Applied Physics B **31**, 97-105 (1983).

211. F. Monet, S. Loranger, V. Lambin-Iezzi, A. Drouin, S. Kadoury, and R. Kashyap, "The ROGUE: a novel, noise-generated random grating," Optics express **27**, 13895-13909 (2019).

212. W. H. Zurek, *Complexity, entropy and the physics of information* (CRC Press, 2018).

213. R. Kashyap, *Fiber bragg gratings* (Academic press, 2009).

214. A. Mafi, "Anderson localization in a partially random Bragg grating and a conserved area theorem," Optics letters **40**, 3603-3606 (2015).

215. G. P. Agrawal, *Nonlinear Fiber Optics: Formerly Quantum Electronics* (Academic press, 2013).

216. S. J. Mihailov, D. Grobnic, C. Hnatovsky, R. B. Walker, P. Lu, D. Coulas, and H. Ding, "Extreme environment sensing using femtosecond laser-inscribed fiber Bragg gratings," Sensors **17**, 2909 (2017).

217. D. Xu, F. Yang, D. Chen, F. Wei, H. Cai, Z. Fang, and R. Qu, "Laser phase and frequency noise measurement by Michelson interferometer composed of a 3×3 optical fiber coupler," Optics express **23**, 22386-22393 (2015).

218. Q. Yuan, F. Wang, T. Liu, Y. Liu, Y. Zhang, Z. Zhong, and X. Zhang, "Compensating for influence of laser-frequency-drift in phase-sensitive OTDR with twice differential method," Optics express **27**, 3664-3671 (2019).

219. L. Stépien, S. Randoux, and J. Zemmouri, "Origin of spectral hole burning in Brillouin fiber amplifiers and generators," Physical Review A **65**, 053812 (2002).

220. A. A. Juarez, R. Vilaseca, Z. Zhu, and D. J. Gauthier, "Room-temperature spectral hole burning in an engineered inhomogeneously broadened resonance," Optics letters **33**, 2374-2376 (2008).

221. R. Uppu, and S. Mujumdar, "Statistical fluctuations of coherent and incoherent intensity in random lasers with nonresonant feedback," Optics letters **35**, 2831-2833 (2010).

222. D. R. Solli, G. Herink, B. Jalali, and C. Ropers, "Fluctuations and correlations in modulation instability," Nature Photonics **6**, 463-468 (2012).

223. T. Godin, B. Wetzel, T. Sylvestre, L. Larger, A. Kudlinski, A. Mussot, A. B. Salem, M. Zghal, G. Genty, and F. Dias, "Real time noise and wavelength correlations in octave-spanning supercontinuum generation," Optics express **21**, 18452-18460 (2013).

224. W. Huang, S. Feng, W. Zhang, and F. Li, "DFB fiber laser static strain sensor based on beat frequency interrogation with a reference fiber laser locked to a FBG resonator," Optics express **24**, 12321-12329 (2016).